NONLEPTONIC DECAYS OF CHARM MESONS

BY

RODNEY LENNART GREENE

S.B., Harvard University, 1985
M.S., University of Texas at Austin, 1987
M.S., University of Illinois at Urbana-Champaign, 1991

THESIS

Submitted in partial fulfillment of the requirements
for the degree of Doctor of Philosophy in Physics
in the Graduate College of the
University of Illinois at Urbana-Champaign, 1995

Urbana, Illinois

NONLEPTONIC DECAYS OF CHARM MESONS

Rodney L. Greene, Ph.D.
Department of Physics
University of Illinois at Urbana-Champaign, 1993
James E. Wiss, Advisor

Amplitude analyses of the $D^+,\ D_s^+ \to K^+K^-\pi^+$ and $D^+,\ D_s^+ \to \pi^+\pi^+\pi^-$ Dalitz plots are presented using data collected by the Fermilab high energy photoproduction experiment E687. Our data are fit to a model consisting of a sum of constant and Breit-Wigner amplitudes for the intermediate three-body nonresonant and two-body resonant decay modes. We extract decay fractions and relative phases. These results are used to infer new branching ratios for the $D^+ \to \phi\pi^+$ and $D^+ \to \overline{K}^*(892)^0K^+$ channels.

I dedicate this thesis to Joyce, my wife and best friend.

Acknowledgments

All the physicists, engineers and technicians participating on the E687 experiment have my gratitude. My close work with some of my collaborators deserves my special thanks.

I am greatly indebted to my advisor Jim Wiss and Illinois colleagues Robert Gardner and Ray Culbertson. Their knowledge, enthusiasm and expertise guided and fueled this work. I really benefitted from working with Rob, who is one of the world's authorities on Dalitz analysis.

I must point out the very welcome collaborative work I shared with two of my Milan colleagues, Sandra Malvezzi and Luigi Moroni. Their work directed and clarified this research at many crucial junctures.

My fellow collaborators and I all owe Joel Butler of Fermilab many thanks for taking on the role of spokesperson for E687.

Jerry Wray and David Lesny designed and maintained a truly outstanding computing enviroment at Illinois.

The love and support of my parents, Robert and Emma, and my sister Rochon, kept me going throughout my entire graduate program.

Of course, the biggest thanks is saved for last - Joyce. Her boundless love is what really made this stuff happen.

This research is funded in part by the U.S. Department of Energy under Grant #DE-FGO2-91ER40677 and by the Illinois Minority Graduate Incentive Program.

Table of Contents

List of Abbreviations

ADC Analog to Digital Converter.

BGM Beam Gamma Monitor – an electromagnetic shower detector designed to collect uninteracted beam photons.

CKM matrix Kobayashi, Maskawa, Cabibbo matrix - a transformation matrix contained in the Standard Model. It rotates the quark weak eigenstates into the physical mass eigenstates.

CL Confidence Level – the percentile rank of a χ^2

CL1 The confidence level that a charm daughter does not point back to the primary vertex.

CL2 The confidence level that no tracks, not in the primary or secondary are in the secondary vertex.

DCL The confidence level of a secondary or charm vertex.

ℓ/σ The separation between the primary vertex and a charm secondary vertex divided by its error.

FSI Final state interaction - mixing and rescatterring of the outgoing hadrons due to strong interaction effects.

$5-$chamber A particle trajectory that is measured in all PWC planes and passes through M2.

Golden modes The copious all charged D decays $K\pi$, $K2\pi$, and $K3\pi$.

H $\times$ V The horizontal and vertical scintillator trigger array.

Link The requirement that a particle trajectory is found in the SSD's and the PWC's and the two segments are associated.

M1, M2 The first and second analysis magnets.

MCS Multiple Coulomb Scattering

MWPC – Multiwire Proportional Chambers, also PWC or chambers.

OE, IE Outer electromagnetic detector and inner electromagnetic detector.

OM, IM Outer muon detector and inner muon detector.

Primary vertex The photon-nucleon interaction point.

RESH Recoil Electron Shower Hodoscope.

SSD Silicon Microstrip Detector

Stub A particle trajectory that is measured in the first 3 PWC planes only, P0-P2.

Track parameters A set of slopes and intercepts used to specify a particle trajectory. The parameters take the form $(x, x' = p_x/p_z, y, \Delta y' = p_y/p_z)$ or (x, x', y, y', p).

Chapter 1

Introduction

This thesis reports the analysis of a sample of charm meson decays collected during the 1990 - 1991 data-taking period of the high-energy physics experiment Fermilab E687. Our study identifies previously undiscovered hadronic decay modes of the D^+ and D_s^+ mesons to the $K^+K^-\pi^+$ final state and confirms known modes for decays to the $\pi^+\pi^+\pi^-$ final state.

Since their discovery in 1974, large samples of charm hadrons (bound states of charm and other quarks) have been produced via three methods: QED e^+e^- annihilation to a virtual photon coupling to a $c\bar{c}$ bound state; inelastic scattering of hadrons upon hadrons; and photoproduction. When the center of mass energy is set to the rest mass of a resonance (such as the $\Psi(3770)$) e^+e^- annihilation has the advantage of producing charm hadrons with little or no background. It is limited by beam luminosity ,[1] where a typical value is $\sim 10^{30} cm^{-2}s^{-1}$. On the other hand, hadroproduction has a large production cross section but copious hadronic backgrounds. Photoproduction obtains both a moderate production rate and background level. Physics studies of these charm states have focused on production and decay mechanisms. We briefly review these topics below.

E687 events are consistent with the photon-gluon fusion production mechanism, [1] where an incident real photon couples with a gluon emitted from a target nucleon via a heavy quark propagator. The resulting $c\bar{c}$ pair then hadronizes to form bound quark states.[2] The lowest order Feynman diagrams of this process are shown in Fig. 1.1 below.

Typical charm decay studies measure lifetimes and branching fractions into purely leptonic, semileptonic and nonleptonic decay modes.[3] This thesis employs

---

1 Luminosity is defined by the equation, production rate = luminosity $\times$ cross section.

2 Recall that states consisting of a single valence quark do not exist in nature. The process of hadronization "dresses" each quark in the $c\bar{c}$ pair with other quarks from the vacuum to form bound states (mesons and baryons).

3 Decays are categorized by the types of the final state particles. Decays with only leptons in

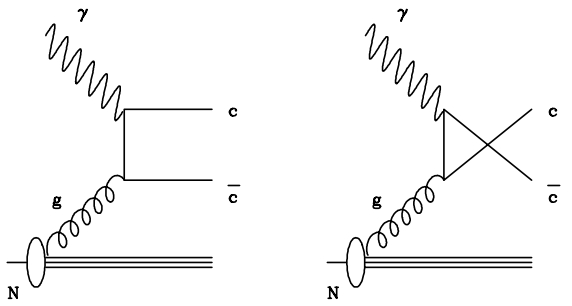

Figure 1.1 The two lowest order (in α_{QCD}) Feynman diagrams of the photon-gluon fusion charm production mechanism. The hadronization process is not shown.

a multidimensional minimization technique to study the resonant substructure of nonleptonic decay modes of the D^+ and D_s^+ charm mesons. Our "charm interferometry" technique measures quantum mechanical interference phenomena in these decays over the entire space of physical observables, thereby maximizing the information content of our results. Although this technique, *Dalitz amplitude analysis*, has been used for at least thirty years to study light meson spectroscopy, only recently have high statistics charm samples become available for Dalitz analysis. We develop the technology of nonlinear minimization to study the rich substructure of these decays.

We begin with a description of the phenomenology employed to describe nonleptonic decay amplitudes. The E687 experimental apparatus, event reconstruction software and Monte Carlo device simulation are outlined in Chapters 3 and 4. The analysis of the decays $D^+, D_s^+ \to K^+K^-\pi^+$ and $D^+, D_s^+ \to \pi^+\pi^+\pi^-$ occupies Chapters 5 and 6. To facilitate comparison with other experiments we extract branching fractions from our Dalitz fit results. Finally, Chapter 7 concludes with an overview of our analysis results.

---

the final state are called 'leptonic;' when the final state contains both leptons and hadrons it is 'semileptonic;' a decay to a purely hadronic final state is termed 'nonleptonic.'

Chapter 2

The Phenomenology of Nonleptonic Decays

2.1 Introduction

The Standard Model succesfully describes the weak interactions between pointlike objects as proceeding via the exchange of charged or neutral bosons (i.e., photons, $W^{\pm}$, Z^0) between particle currents. The amplitude for this process is $\mathcal{A}_{SM} = \frac{4G_F}{\sqrt{2}} V_{qq'} V^*_{q''q'''} J^\mu j_\mu$, where the $\{V_{qq'}\}$ are the appropriate CKM matrix elements.[1] On the other hand, weak interactions between composite particles (i.e., mesons and baryons) cannot be completely described by the Standard Model. Several models have been developed [3, 4] to explain the weak hadronic decay mechanisms of D mesons. Most of these models require experimentally measured branching ratios and deal only with decays mediated by resonant states. Some can accommodate final state interaction,[2] the level of which can be measured by looking at the relative phases between interfering decay amplitudes. The extent to which model calculations can adequately describe the data can be gauged by comparing the predicted pattern of two-body decays to experimental measurement.

A particular model developed by Bauer, Stech and Wirbel [4, 6, 7] is an attempt to apply the standard model framework to these complex interactions. It is motivated by the spectator valence quark flow diagram for 2-body weak decays of hadrons (see, for example, Figure 2.1). This diagram identifies the exchanged boson with the heavy quark (i.e., charm, bottom, top) in a hadron, while the light quark does not contribute to the interaction (except in hadronization). The BSW model postulates the amplitude $\mathcal{M}$ for the two-body decay process $D \to Mm$

1 See, for example pages 251-291 in Ref. [2].

2 Final state interaction refers to mixing and rescatterring of the outgoing hadrons due to strong interaction effects (*i.e.*, gluon exchange, quark fragmentation, etc.). The classic example is the decay process $D^0 \to K^{*0}\eta \to \overline{K}^0\phi$, where the $\overline{K}^0\phi$ state results from rearrangement of the η valence quarks. [5]

factorizes as follows (see, for example, Eq. 2.9 in Ref. [8]):

$$\mathcal{M}(D \to Mm) = \frac{4G_F}{\sqrt{2}} V_{cq} V_{ud}^* h^\mu H_\mu. \tag{2.1}$$

Here H_μ and h^μ are effective hadronic current matrix elements and they contain the dynamics of this 2-body process. G_F is the Fermi coupling constant and V_{cq}, V_{ud} are CKM matrix elements. Regrettably, particle physics does not have a complete understanding of these hadron wave functions and hence the exact form of these hadronic currents is unkown. Fortunately all

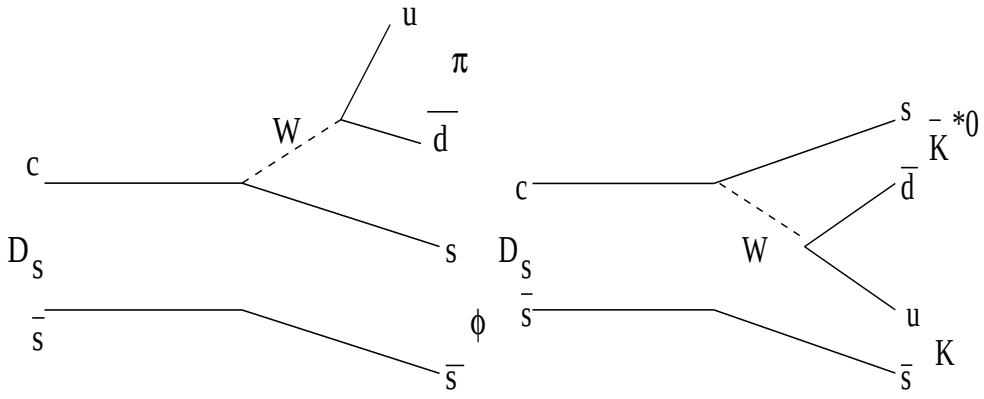

Figure 2.1 Spectator valence quark flow diagrams for the two-body decays of the D_s^+ into $\phi\pi^+$ (left) and the $\overline{K}^*(892)^0 K^+$ (right) decay channels.

is not lost because the method of *Dalitz plot analysis* provides the particle physicist with a framework to obtain phenomenological descriptions of these decays. We presently describe this method.

This thesis investigates nonleptonic decays of the D^+ and D_s^+ [3] charmed mesons of the form $D \to rc$ followed by $r \to ab$. Here, D represents a ground state 0^- charmed meson, a,b and c are 0^- psuedoscalar mesons and r is a meson with spin-parity J^P belonging to the list $0^+, 1^-, 2^+, 3^-, \ldots$. By limiting our analysis to

3 Unless otherwise stated, when referencing a particular state, we implicitly include its charge conjugate.

these particular spin-parity mesons r, we can apply the results of Zemach Table I [9] to our formalism. Also, by studying the 3-body final state $(ab)c$ we obtain insight into the 2-body process $D \to rc$.

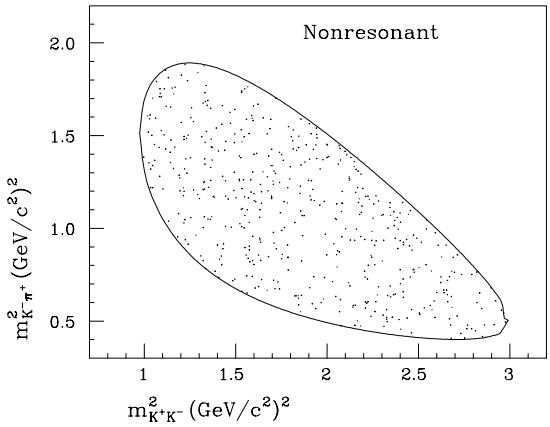

Figure 2.2 Dalitz scatterplot from a Monte Carlo simulation of $D^+ \to K^+K^-\pi^+$ using a constant decay amplitude (so-called *nonresonant decay*).

By applying symmetry arguments one can determine the minimum number of degrees of freedom necessary to completely specify the decay of a hadron into N spinless daughter particles. The decay is described fully in terms of $3N$ momentum components. Rotational invariance of the decay matrix element means it does not depend on the three Euler angles which orient the final state particles in Cartesian space. Hence we lose three additional degrees of freedom. Energy-momentum conservation provides 4 additional constraints, thus reducing the number of observables required to fully specify the N-particle final state to $3N - 3 - 4$, which for a $3-$body final state leaves only two observables.

For the three-body final state, a particularly convenient choice of observables is the squared invariant mass of any two of the possible three two-body combinations, say m^2_{ab} [4] and m^2_{ac}. This choice is motivated by the observation that

4 If p^μ_X is the energy-momentum four-vector for particle X, then $m^2_{ab} = (p^\mu_a + p^\mu_b)^2$.

the decay width $d\Gamma$ for the three-body decay $D \to abc$ depends on the quantum mechanical amplitude $\mathcal{A}$ according to:

$$d\Gamma = \frac{|\mathcal{A}|^2}{256\ \pi^3\ M^3}\ dm_{ab}^2\ dm_{ac}^2 \tag{2.2}$$

where M is the mass of the parent particle. Hence a constant amplitude will manifest itself as a uniform scatterplot in m_{ab}^2 and m_{ac}^2, as shown in Fig. 2.2. Departures from uniformity flag resonant substructure. So our preferred observables are the squared masses of the final state particles which we display on the so-called *Dalitz scatterplot.*

2.2 Amplitude Formalism

We begin this section with an informal description of the phenomenology of decay amplitudes by appealing to angular momentum conservation arguments. Section 2.2.2 outlines the Zemach [9-10] formalism, which uses angular momentum tensor operators to form decay amplitudes. We will use it in our analysis of charm meson decay in Chapters 5 and 6. In the Appendix, we describe an alternative analysis framework, the helicity formalism, which employs the rotational invariance of the helicities of the daughter particles to construct decay amplitudes. This formalism will enter our analysis as a systematic check on our method.

2.2.1 An Informal Look

Figure 2.3 shows Dalitz plots for the D^+ and D_s^+ decaying to the $K^+K^-\pi^+$ final state. The resonant structure is evident in each of these Dalitz plots and it is especially clear in the plot for the decay $D_s^+ \to K^+K^-\pi^+$ where the plot is strongly dominated by a band of events near $m_{K^+K^-}^2 \approx 1\ GeV^2$ due to the decay chain $D_s^+ \to \phi\pi^+ \to (K^+K^-)\pi^+$. The band near $m_{K^-\pi^+}^2 \approx 0.8\ GeV^2$

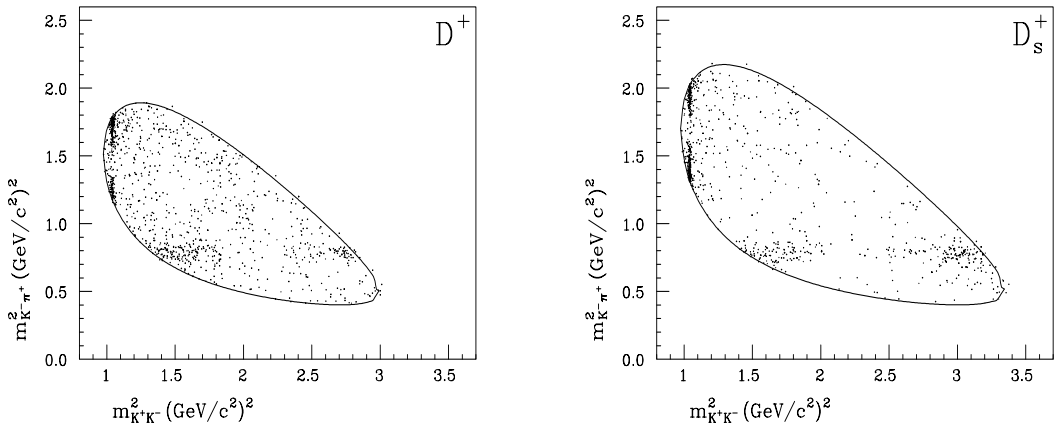

Figure 2.3. Dalitz scatterplots for the decays D^+ and D_s^+ to $K^+K^-\pi^+$.

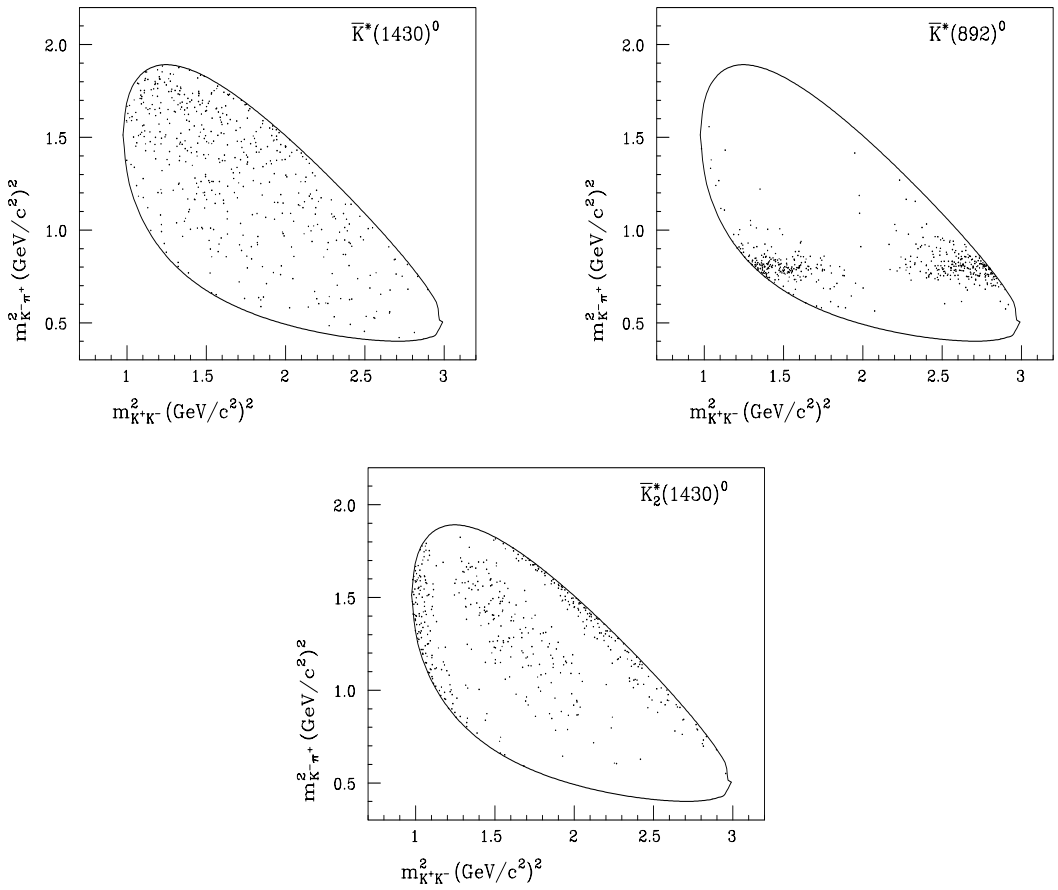

Figure 2.4 Illustration of nodal structure for Monte Carlo simulated Dalitz plots for decays of the form $D^+ \to \overline{K}^{*0} K^+$.

is due to $D_s^+ \to \overline{K}^*(892)^0 K^+ \to (K^+K^-)\pi^+$ decays. The depopulation in the center of both the ϕ and $\overline{K}^*(892)^0$ bands is due to a node in the angular wave function describing the decay of the vector meson resonance to two pseudoscalars.[5] Consider the band due to $\phi\pi^+$. Because the D_s^+ has no spin, the ϕ must be in a $|1,0>$ state in the ϕ rest frame in which we quantize angular momentum along the direction of the spinless π^+. The subsequent decay distribution of the kaons is thus $|Y_1^0(\theta,\phi)|^2$ which has a node at $\theta = 90^o$ where θ is the angle between the K^+ and the π^+ viewed in the ϕ rest frame. As one varies θ from $0 \to 180^o$ one moves from the smallest, allowable $m^2_{K^-\pi^+}$ value to the largest, and therefore the 90^o node in Y_1^0 will appear in the center of the ϕ band. Possible higher spin-J resonances will decay into two pseudoscalars according to $|Y_J^0(\theta,\phi)|^2$ which in general will have J angular nodes in θ and will appear as J nodes on the Dalitz plot. Figure 2.4 illustrates the nodal pattern in the Dalitz plots for simulated D^+ decays into several, pure spin $-$ J resonances.

In addition to the readily apparent ϕ and $\overline{K}^*(892)^0$ bands, the remaining dots may be due to decay via the three-body nonresonant channel or due to some superposition of resonant channels. An important application of Dalitz analysis is to determine the strength of a nonresonant component.

Comparison of the $\overline{K}^*(892)^0$ bands of the two $KK\pi$ Dalitz plots shown in Figure 2.3 illustrates the importance of interference effects in three $-$ body D decay. The D_s^+ Dalitz plot exhibits symmetric intensity lobes on either side of the Y_1^0 node while the D^+ Dalitz plot's lower K^+K^- mass lobe is much more intense than the upper mass lobe. This effect cannot be explained by either acceptance or resolution as will be discussed below. The asymmetry of the two lobes for the D^+ can be explained by having the $\overline{K^*}K^+$ amplitude interfere with either a constant or very slowly varying amplitude[6] of relative strength a and

5 These nodal regions are called *Zemach zeros*.

6 In Chapter 5, we will argue that the 'very slowly varying amplitude' is a broad scalar $K_0^*(1430)^0 K^+$ decay amplitude. It is responsible for the interference with the $\overline{K}^*(892)^0 K^+$ channel.

relative phase δ:

$$\mathcal{A} = \frac{\cos\ \theta_{KK}}{M_r^2 - M_{K\pi}^2 - i\Gamma M_r} + a\ (\cos\ \delta + i \sin\ \delta) \tag{2.3}$$

The K^* amplitude is described by a Breit-Wigner form along with a factor of cos θ_{KK} to represent the angle dependent amplitude described above (θ_{KK} is the angle between the two kaons in the $\overline{K^*}$ rest frame). The interference of these two amplitudes will produce a contribution to the intensity function $\mathcal{A}\mathcal{A}^*$ of the form:

$$2\ a\ Re\left\{(\cos\ \delta + i \sin\ \delta)^*\ \ \frac{\cos\ \theta_{KK}}{m_r^2 - m_{K\pi}^2 - i\Gamma m_r}\right\} =$$

$$2\ a\ \left(\frac{\left(m_r^2 - m_{K\pi}^2\right)\ \cos\ \theta_{KK}\ \cos\ \delta}{\left(m_r^2 - m_{K\pi}^2\right)^2 + \Gamma^2 m_r^2} + \frac{\Gamma m_r\ \cos\ \theta_{KK}\ sin\ \delta}{\left(m_r^2 - m_{K\pi}^2\right)^2 + \Gamma^2 m_r^2}\right) \tag{2.4}$$

As one moves in the direction of increasing $m^2_{K^+K^-}$ mass along the $\overline{K^*}$ band, cos θ_{KK} goes from +1 to -1 and both terms of Eq. (2.4) will switch sign. Along a line of constant $m^2_{K^+K^-}$ mass, the first interference term which dominates for

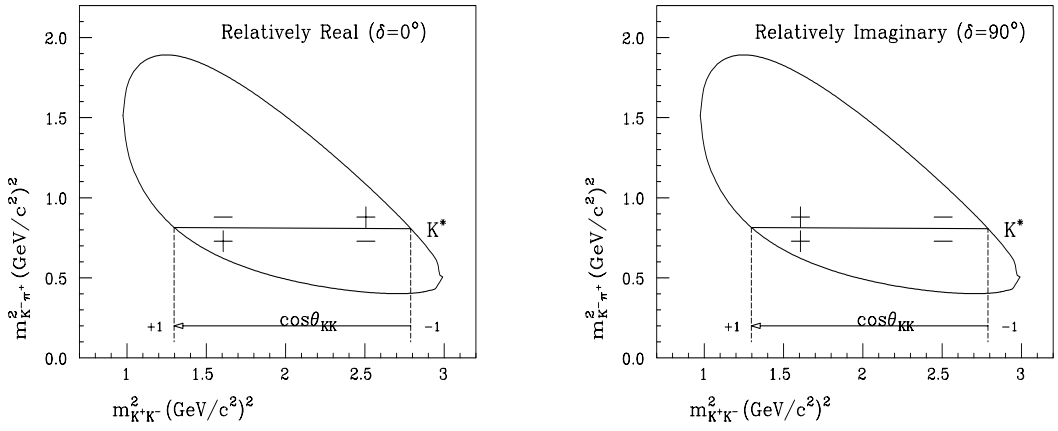

Figure 2.5 A graphical representation of the signs of the interference terms in the intensity function for real and imaginary phase differences overlayed with the D^+ Dalitz boundary and a scale giving the $cos\theta_{KK}$ axis.

relatively real amplitudes ($eg\ \delta = 0$) switches sign as one moves from $m^2(K^-\pi^+)$ masses below the $\overline{K^*}$ resonance to masses above the resonance; while the second interference term which dominates for relatively imaginary amplitudes does not change sign under this motion. The pattern for real and imaginary phase differences is illustrated in Figure 2.5. The interference present in the D^+ Dalitz plot most resembles the pattern for a relatively imaginary amplitude, and since the destructive interference of the upper lobe is nearly complete, both the constant amplitude and Breit-Wigner $\overline{K^*}$ amplitudes must have comparable local intensity.

2.2.2 The Zemach Formalism

Unlike the helicity formalism described in the Appendix, the Zemach model [9,10,11] has the pleasing feature that it naturally includes the momentum dependence of the decay amplitude in an unambiguous manner. In this section we detail the Zemach amplitude for the two-step sequential decay process $D \to rc \to (ab)c$. Before describing the details, we motivate this parameterization by applying the familiar Feynman rules, [pp. 117-151 in Ref. 2] to obtain the amplitude for decay via an intermediate vector resonance.

Figure 2.7 is an example Feynman diagram of a particular decay, $D \to \phi\pi^+ \to (K^+K^-)\pi^+$. According to the Feynman rules, the matrix element is $\mathcal{M} = F_D(q^2)\ (\pi + D)^\mu \times (Massive\ Propagator) \times F_r(q^2)(K^+ - K^-)_\mu$, where F_D and F_r are the q^2 dependent hadronic form factors which describe the non-pointlike nature of the hadrons. The terms $(\pi+D)^\mu$ and $(K^+-K^-)_\mu$ are effective hadron currents. For the case of a decay mediated by a vector meson resonance we obtain [13, 14]

$$\begin{aligned} \mathcal{M} &= (p_c + p_D)^\mu \frac{(-g_{\mu\nu} + \frac{q_\mu q_\nu}{m_{ab}^2})}{q^2 - m_r^2}(p_a - p_b)^\nu \\ &= \frac{(m_{ac}^2 - m_{bc}^2) - \frac{(m_D^2 - m_c^2)(m_a^2 - m_b^2)}{m_{ab}^2}}{m_r^2 - m_{ab}^2 - i\Gamma m_r} \end{aligned} \tag{2.5}$$

The numerator simplifies to $-4\vec{c}^{ab} \cdot \vec{a}^{ab} = -4|\vec{c}^{ab}|\ |\vec{a}^{ab}|\ \cos\theta^{ab}_{ca}$, where the 3-momentum vectors are measured in the (ab) rest frame. The periodic function $\cos\theta^{ab}_{ca}$ carves out the Zemach zeros in the resonance bands of the Dalitz plot, and results in the $\cos^2\theta$ dependence of the intensity function discussed in Eq. 2.3.

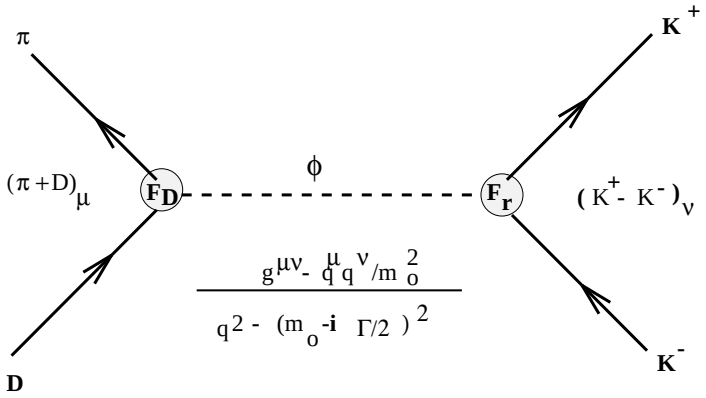

Figure 2.7 Feynman diagram for the process $D \to rc \to (ab)c$. In this example, $a = K^+$, $b = K^-$, $c = \pi^+$ and $r = \phi$. The arrows represent 4-momenta of the participating mesons. q is the 4-momentum of the exchanged meson r of spin J. In this example, the resonance particle is a spin -1 ϕ.

The spin limitation of these rules is due to the fact the Feynman theory does not address higher spin propagators. Below we describe the Zemach framework, which will form the heart of our generalized amplitude formalism.

Within the Zemach framework we model the decay chain with a complex amplitude consisting of a Breit-Wigner propagator for the intermediate resonance r multiplied by a product of form factors and effective hadronic matrix elements for each hadronic current. These current terms are constructed from the 3-momenta of the particles. Following Zemach, [9] the amplitude for the double decay is written

$$\mathcal{M}\left[D \to rc \to (ab)c\right] = \left[y\ T^J(\vec{c}) + z(\vec{c}\cdot\vec{r})T^J(\vec{c})\right] :\ T^J(\vec{a})\ \times\ BW(q) \qquad (2.6)$$

Here, y and z are the vertex form factors. T^J is a tensor of rank J in 3-space:

$$T^J_{m_1 m_2 \ldots m_J}, \quad m_i \;=\; 1,2,3$$

It is a function of the indicated 3-momentum vectors. The ':' operator denotes a tensor product (a summation over the indices m_i). With the three-momenta evaluated in the r rest frame, the term $z(\vec{c}\cdot\vec{r})T^J(\vec{c})$ vanishes. BW is the Breit-Wigner propagator and is a function of the momentum transfer q between the D and the final state psuedoscalar c. It takes the form

$$\frac{1}{m_0^2 - m_{ab}^2 - i\Gamma m_0} \tag{2.7}$$

where m_0 is the on-shell mass of the resonance r and Γ is its width. The term m_{ab}^2 is the squared invariant mass of the final state particles a and b. Applying Zemach [10] equation 5.1 we obtain

$$\begin{aligned} \mathcal{M}\,[D \to rc \to (ab)c] &= y\; T^J(\vec{c}) : T^J(\vec{a}) \;\times\; BW(q) \\ &= y\; c_J |\vec{c}|^J |\vec{a}|^J P_J(\cos\theta^r_{ac}) \;\times\; BW(q) \end{aligned} \tag{2.8}$$

Here, θ^r_{ac} is the angle between a and c in the r rest frame. P_J is the familiar Legendre polynomial. c_J is a normalization constant which by convention is set to $(-2)^J$. This result enables us to list the matrix elements for various intermediate resonances, as shown in Table 2.1.[7]

Table 2.1 Zemach Amplitudes $\mathcal{M}(abc|r)$ for $D \to rc \to (ab)c$

$J^P(r)$	Example	$\mathcal{M}(abc\|r)$	Notation
nonresonant	-	1	NR
0^+	$f_0(975)$	$y \;\times\; BW$	$S(abc\|r)$
1^-	$\phi(1020)$	$y \;\times\; -2\|\vec{C}\|\;\|\vec{A}\|\;\cos\theta^R_{AC} \;\times\; BW$	$P(abc\|r)$
2^+	$K^*(1430)$	$y \;\times\; (-2\|\vec{C}\|\;\|\vec{A}\|)^2\,\frac{1}{2}(3\cos^2\theta^R_{AC} - 1) \;\times\; BW$	$D(abc\|r)$
3^-	$K^*(1780)$	$y \;\times\; (-2\|\vec{C}\|\;\|\vec{A}\|)^3\,\frac{1}{2}(5\cos^3\theta^R_{AC} - 3\cos\theta^R_{AC}) \;\times\; BW$	$F(abc\|r)$

7 Our model for the $f_0(980)$ resonance is described in Appendix C.

Note that $P(abc|r)$ contains the $\cos\theta$ dependence we expected from section 2.2.1.[8] It gives rise to the Zemach zeros in the Dalitz plot. These matrix elements contain the traditional momentum dependent form factors and resonance decay widths developed by Blatt and Weisskopf. [15] The form factor y above is a product of the D meson form factor F_D and the form factor for the resonance, F_r. They take the forms [16] listed below:

Table 2.2 Blatt and Weiskopf Form Factors F_X

Spin J of Decaying Particle	Form Factor F_X
0	1
1	$\frac{1}{\sqrt{1+R_X^2 P^{*2}}}$
2	$\frac{1}{\sqrt{9+3R_X^2 P^{*2}+(R_X^2 P^{*2})^2}}$
> 2	1

R_X is the meson radius parameter and is taken to have the following values [16]:

Table 2.3 Blatt and Weiskopf Meson Radii R_X

Parent charm meson D	$5\ GeV^{-1}$
Intermediate resonance particle R	$1.5\ GeV^{-1}$

The resonance width $\Gamma(m_{ab}^2)$ is written

$$\Gamma \;=\; \Gamma_0 \left(\frac{|\vec{P}_{ab}|}{|\vec{P}^*|}\right)^{2J+1} \frac{M_0}{M_{ab}} \frac{F_r^2(P^{*2})}{F_r^2(P_0^{*2})} \tag{2.9}$$

where $\vec{P}^* \;\equiv$ decay 3-momentum in the (ab) rest frame and J is the spin of the resonance particle.

8 The term $\cos\theta_{KK}$ in Eq. 2.3.

The reader may be bothered by the fact the the Zemach amplitude, Eq. 2.8, appears to be not Lorentz invariant, which clearly must hold for our amplitude formalism to be useful. In Appendix D we address this issue and show that in fact the Zemach amplitude is Lorentz invariant. The non-relativistic appearance is simply an artifact of our choice to write the amplitude in the rest frame of the intermediate resonance r.

2.3 Method of Amplitude Analysis

At this point we have developed the phenomonology for the matrix elements for the nonleptonic decay of a charm meson via a single intermediate resonance. In order to make the formalism complete we must allow interference between these various decay channels. So the general amplitude for $D \to rc \to (ab)c$ is a coherent superposition of N amplitudes of the form in Table 2.1.[9] It is written

$$\mathcal{A}(D \to rc \to (ab)c) = \sum_{i=1}^{N} a_i e^{i\delta_i} \mathcal{M}(abc|r_i) \tag{2.10}$$

As a concrete example, visual inspection of the $D_s^+ \to K^+K^-\pi^+$ Dalitz plot, Fig. 2.3, leads one to guess that this decay proceeds via the landmark channels $\phi\pi^+$ and $\overline{K}^*(892)^0K^+$ as well as the three-body nonresonant mode -

$$\begin{aligned} \mathcal{A} \;=\; a_{NR}\; e^{i\delta_{NR}} \;&+\; a_\phi\; e^{i\delta_\phi} P(K^+K^-\pi^+|\phi) \\ &+\; a_{\overline{K}^*(892)^0}\; e^{i\delta_{\overline{K}^*(892)^0}} P(\pi^+K^-K^+|\overline{K}^*(892)^0) \end{aligned} \tag{2.11}$$

We interpret the terms involving the intermediate resonances ϕ and $\overline{K}^*(892)^0$ as a superposition of the spectator Feynman diagrams in Figure 2.1. The goal of the present work is to obtain the mixing parameters a_i and δ_i by fitting our hypothesized intensity function $\mathcal{A}\mathcal{A}^*$ to the observed distribution of final states on the Dalitz plot.

---

9 We discuss our convention for the amplitude for decay of the antiparticle, $\overline{D}$, in Sec. 5.2.

It is important to note that although most D decay analyses thus far essentially use a variant of Eq. (2.10), it is really only a phenomenological approximation to the strong interaction portions of the true decay amplitude. In particular, all phase shifts other than kinematic phase shift evolution for ideal Breit-Wigner resonances[10] are neglected, and the a_i amplitude strengths are treated as constants, although in principle they can certainly exhibit slow variations across the Dalitz plot. Given large enough charm sample sizes, one would surely expect that the naive form of Eq. (2.10) would fail to fit the data except in a qualitative sense.

We note one of the a_i and δ_i parameters in Eq. (2.10) is redundant. Because the intensity or Dalitz population is unchanged by an overall phase factor, one phase (usually taken to be the dominant contribution) is defined to be $\delta = 0$. Similarly, one of the a_i's is actually determined through the normalization condition required in a likelihood fit on the efficiency corrected intensity (See Section 5.2).

It has become customary to present information on the amplitude strengths a_i indirectly – by way of a "decay fraction". The decay fraction (f_i) into a given resonance is computed by taking the integral of an intensity which just includes the amplitude contribution for the given mode divided by the integral of the intensity with all amplitudes present.

$$f_i = \frac{\int dm^2_{ab}\, dm^2_{ac}\, \left(a_i\, e^{i\delta_i}\, \mathcal{M}(a\ b\ c\ |r)\right)^* \left(a_i\, e^{i\delta_i}\, \mathcal{M}(a\ b\ c\ |r)\right)}{\int dm^2_{ab}\, dm^2_{ac}\, \left(\sum_i a_i\, e^{i\delta_i}\, \mathcal{M}(a\ b\ c\ |r)\right)^* \left(\sum_i a_i\, e^{i\delta_i}\, \mathcal{M}(a\ b\ c\ |r)\right)} \qquad (2.12)$$

The decay fraction roughly represents the probability that the state decays via a given resonant channel. Of course, unlike a conventional probability, one frequently finds that $\sum_i f_i \neq 1$ owing to interference. One big advantage of quoting

10 By 'kinematic phase shift evolution for ideal Breit-Wigner resonances,' we mean the mass-squared dependent 'intrinsic' phase of the Breit-Wigner function, $\tan^{-1} \frac{Im\ BW}{Re\ BW}$. In principle, the fitted phases δ_i could also be functions of the mass-squared observables, but in our formulation they are constants to be found by our fitting procedure.

decay fractions rather than amplitude coefficients is that many phase, Breit-Wigner, and spin factor conventions cancel out in the ratio, thus allowing for easy comparison between different analyses.

2.4 Closing Remarks

Other authors [6, 16, 17, 18, 19, 20] have accomplished fully coherent amplitude analysis of charm meson decays by considering three-body $K\pi\pi$ final states of the D^+ and D^0. The E691 collaboration [21, 22] has presented semi-coherent fits to the $KK\pi$ and $\pi\pi\pi$ final states of the D^+ and the D_s. This thesis describes the first fully coherent analysis of D^+ and D_s decays to $KK\pi$ and $\pi\pi\pi$.

It is worth pointing out that the measured decay fractions can be converted into branching ratios if the absolute branching fraction for the respective final states are known. These are computed by multiplying the branching fraction by the fit fraction determined by the Dalitz plot fit, and then dividing by the appropriate branching ratio (or Clebsch Gordon coefficient) for the $(K\pi)$ or (KK) resonance where appropriate. By following this procedure, we can compare our results to the predictions of various models of nonleptonic charm decay, including that of Bauer, Stech and Wirbel. [4]

As we will see in the following chapters, our method allows one to determine the relative strengths of the diagrams in Figure 2.1. Although the fit qualitatively reproduces many features of the data, there remain statistically significant discrepancies. Hence, our analysis can only be considered a first step toward understanding nonleptonic decays of charm mesons.

Chapter 3

The E687 Apparatus

The design goal of the Fermilab Wideband Photon Beam Laboratory is to attain high charm photo-production rates while suppressing non-charm background processes. We achieve these competing goals by combining a high energy photon beam with outstanding vertexing and particle identification capabilities. The spectrometer has been descibed in detail elsewhere. [23, 24] Here we summarize the major features of the detector. Figure 3.1 shows the overall layout of the apparatus and Table 3.1 summarizes its dimensions.

3.1 Beamline

The high energy photon beam for the E687 experiment is obtained by bremsstrahlung. The process starts at the Fermilab Tevatron, which operates in cycles of about 60 seconds. It is filled with 800 GeV protons which are extracted over a 20 second 'spill.' About $3 - 4 \times 10^{12}$ protons are delivered to the E687 beamline during each spill. This proton beam is directed to a deuterium target (the *primary production target*) where it initiates a hadron shower. Sweeping magnets downstream of this target remove charged particles, leaving only photons, neutrons and K^0's. This beam of neutral particles then interacts in a 50% radiation length lead foil (the *converter*), which causes about half of the photons to convert into electron-positron pairs. The electrons are swept into a beam transport system consisting of dipole and quadrupole magnets. The positrons and neutral hadrons are absorbed in the *neutral dump*.

The electron beamline contains collimators which select electrons of mean energy 350 GeV. The energy bite is large, $\pm 7.5\%$ (hence the name Wideband) to achieve high luminosity. Finally the electrons are directed to a 27% radiation length lead foil (the *radiator*) where photons are created by bremsstrahlung. The recoiling electron is swept away by magnets and the photon beam strikes the beryllium *experimental target*.

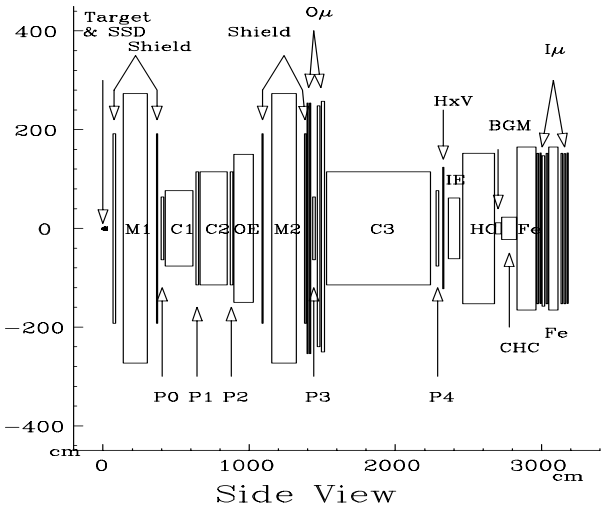

Figure 3.1 Side view of the E687 spectrometer.

Table 3.1 Spectrometer Layout

Device	z (center)	x Full Aperture	y Full Aperture
TARGET	-3.00	2.54	2.54
SSD1	4.56	2.48	3.50
SSD2	10.57	4.96	4.96
SSD3	16.59	4.96	4.96
SSD4	28.51	4.96	4.96
M1 US MIRROR	77.44	25.40	101.60
M1	220.95	76.20	127.00
M1 DS MIRROR	370.17	76.20	127.00
PWC 0	403.14	76.20	127.00
C1	519.75	101.60	152.40
PWC 1	644.58	152.40	228.60
C2	757.00	152.40	228.60
(continued)			

Table 3.1 Spectrometer Layout (continued)

PWC 2	879.18	152.40	228.60
OE	962.99	270.00	300.00
M2 US MIRROR	1091.43	76.20	127.00
M2	1238.11	76.20	127.00
M2 DS MIRROR	1383.52	76.20	127.00
OMX	1399.24	304.80	508.00
OMY	1416.94	304.80	508.00
PWC 3	1444.13	76.20	127.00
OMH	1474.56	304.80	487.68
OMV	1505.06	304.80	508.00
C3	1884.42	190.50	228.60
PWC 4	2285.88	152.40	228.60
H x V	2328.19	274.30	365.80
IE	2399.67	137.16	228.60
HC	2569.78	203.20	304.80
BGM	2445.00	25.40	22.86
CHC	2778.00	45.72	45.72
IM SHIELD 1	2895.66	231.14	330.20
IM1X	2973.48	203.20	304.80
IM1Y	62993.21	203.20	304.80
IM1V	3012.52	213.36	304.80
IM1H	3036.07	203.20	304.80
IM SHIELD 2	3079.66	231.14	330.20
(continued)			

Table 3.1 Spectrometer Layout (continued)

IM2X	3138.95	203.20	304.80
IM2Y	3158.09	203.20	304.80
IM2H	3178.25	203.20	304.80

3.2 Experimental Target and Microstrip Detector

The experimental target is a slab of beryllium 2.54 cm square and approximately 4cm long. This configuration obtains a radiation length:hadronic interaction length ratio of 11.5% : 10%. Given that this ratio > 1, the experiment can run at high photon flux (about $3 \times 10^6 \gamma$/sec) without saturating the spectrometer with $\gamma N \rightarrow e^+e^-$ non-charm events.

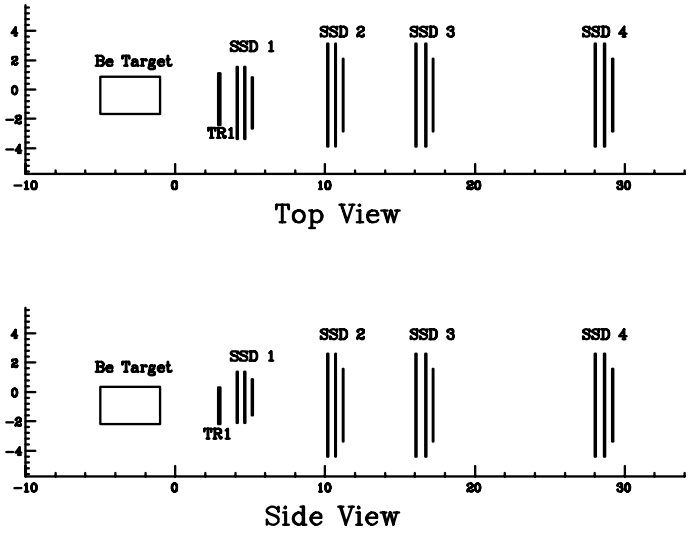

Figure 3.2 Top and side views of the E687 silicon microstrip planes.

The microstrip detector is located about 5 cm downstream of the experimental target. By measuring the trajectories of charged particles with very high precision, one can exploit the lifetime of charm paticles (typically 1 cm decay length for D mesons) to identify charm signals. Refering to Figure 3.2, the microstrip system consists of 12 planes arranged into 4 stations of 3 planes each. In each station , one plane measures in the y-direction and two planes are tilted in

opposite directions from the y-axis by 45° . Each plane is divided into an inner high-resolution region and an outer lower-resolution region. The strips in the planes of the most upstream station have 25μ pitches in the inner region and 50μ pitches in the outer region. The remaining stations have 50μ and 100μ pitches, respectively.

3.3 MWPC's and Magnets

Momentum measurement of charged particles is achieved by a system of two dipole magnets integrated with 20 planes of multi-wire-proportional wire-chambers (MWPC's). The first magnet, M1, bends charged particles in the y-direction with a kick ($0.3 \int B d\ell$) of 0.4 GeV/c. The second magnet, M2, bends particles so that their trajectories return to their undeflected positions toward the downstream end of the apparatus. It has a kick of -0.835 GeV/c.

Table 3.2 PWC Specifications

		# instrumented wires			
Station	Pitch	X	U	V	Y
P0	2mm	376	640	640	640
P1	3mm	512	832	832	768
P2	3mm	512	832	832	768
P3	2mm	376	640	640	640
P4	3mm	512	832	832	768

Located downstream of M1 and M2 as well as upstream of M2 are 20 planes of MWPC's arranged in 5 stations. Each station contains 4 planes (also called *views*). One view measures in the y-direction, another in x, and two others (u and v) are tilted in opposite directions from the y view by 11°. Each view is a set of readout wires separated from the other views by a cathode plane which is also made of wires. Charged particles passing through these chambers ionize an argon-ethane gas mixture while a high voltage between the readout and cathode

planes amplifies and collects the ions. These signals are further amplified and recorded by Time-to-Digital-Converters (TDC's).

The specifications of these chambers are summarized in Table 3.2.

3.4 Čerenkov Particle Identification

When charged particles traverse a dielectric with a velocity exceeding the phase velocity of light in the material they emit *Čerenkov* radiation. For a volume containing a dielectric of index of refraction $n = 1 + \delta$ ($\delta << 1$), the momentum threshold for Čerenkov radiation due to a particle of mass m obeys the (approximate) relation $p_{threshold} = \frac{m}{\sqrt{2\delta}}$. So by carefully choosing n one can engineer the momentum threshold for Čerenkov radiation for a selected particle. E687 has three threshold Čerenkov counters which discriminate between electrons, pions, kaons and protons.

The features of the Čerenkov detectors are summarized in Table 3.3. Each counter is segmented into cells, each cell consisting of mirrors (planar and focusing) and a phototube for conversion of the Čerenkov photons into electrons.

Table 3.3 Characteristics of the Čerenkov Detectors

Counter	Gas	cells	Photoelectron yield (ave)	Thresholds (GeV) π	K	p
C1	57% He/43% N_2	90	3.1	8.4	23.3	44.3
C2	N_2O	110	9.4	4.5	16.2	30.9
C3	He	100	9.0	17.0	61.0	116.2

The response of each counter can be described by the average number of photoelectrons detected in a particular cell by a $\beta = 1$ particle when all the Čerenkov light is enclosed by the cell.

3.5 Muon Identification

Muons are essentially heavy electrons ($m_\mu = 0.105 GeV/c^2$) which interact via the weak and electromagnetic interactions. Since muons have absorption lengths which are much longer than typical hadronic interaction lengths, in order to detect muons it is necessary to filter out the hadrons with large amounts of dense material (i.e., steel shielding). By interleaving layers of shielding with layers of scintillator (or proportional tubes) one can detect the unabsorbed charged muons.

The E687 spectrometer contains a section for identifying low angle muons (the *inner muon detector*) produced at less than 40 mradians, and a section for wide angle muons extending out to 125 mradians (the *outer muon detector*). The inner muon counter is shielded by the inner electromagnetic calorimeter, the hadronic calorimeter, cement blocks and steel. It contains three planes of scintillator for triggering and four planes of proportional tubes (in x and y) for localising the muon trajectory. M2 provides the shielding for the outer detector. It has two layers of scintillator and separate x/y views of proportional tubes. The muon system is not used for this analysis.

3.6 Calorimetry

Electromagnetic showers are initiated by the electromagnetic interactions of electrons, positrons and photons. They are dominated by bremsstrahlung of e^-/e^+ followed by conversion of the photons via $\gamma N \rightarrow e^+e^-$. Calorimeters work by absorbing the incident energy of a particle and converting it into recordable signals. EM showers have the characteristics that they are completely described by Quantum Electrodynamics and all of their energy is deposited as ionization energy loss of electrons. So by installing alternating layers of steel and scintillator one can effect EM showers and detect the subsequent ionization energy loss. On the other hand, hadronic showers are much more complicated, involve the entire spectrum of hadrons, and are not well understood. Basically, hadron showers are detected in a fashion similar to EM shower detectors with much more absorber material (i.e., steel) being used.

The E687 spectrometer has two electromagnetic shower detectors. The inner electromagnetic calorimeter (*IE*) is located immediately upstream of the hadron calorimeter and provides coverage for electrons and photons produced up to about 26 mrad. The outer electromagnetic calorimeter (*OE*) is located just upstream of M2 and samples electromagnetic interactions up to about 150 mrad. Each counter consists of alternating layers of lead and scintillator. The electromagnetic shower detectors are not used for the analysis in this thesis.

The hadron calorimeter (*HC*) is immediately downstream of the IE and covers the region from 5 mrad to approximately 30 mrad. It uses steel as the absorber and argon-ethane proportional tubes as the ionization energy loss sampler. The measured resolution is $\sigma_{\mathrm{E}}/\mathrm{E} \simeq 1.33/\sqrt{\mathrm{E}}$. It is primarily used as a part of the trigger, which is described in the next section.

3.7 Event Trigger

Most of the components of the E687 spectrometer described so far are essential for off-line analysis of the data. As stated in the introduction of this chapter, an essential function of the on-line hardware and software is to identify charm events and suppress the background. It can be shown that for high energy photoproduction, the rate for hadronic interactions is about 1/500 of the rate for pair production. The purpose of the trigger is to efficiently identify these hadronic interactions and initiate writing the state of the detector (i.e., ADC values, scalar counts, etc) to magnetic tape for subsequent off-line analysis. Generally, e^+/e^- pairs are produced with little transverse momentum so they populate a region approximately the size of the beam. Conversely, hadronically produced particles typically have wide angle trajectories and also deposit non-negligible energy in the hadron calorimeter. So the trigger hadware is arranged to detect wide angle charged hadronic particles.

The trigger is organized in two levels : a fast first level (*master gate* or *MG*) and a slower second level trigger. The master gate is responsible for gating the data acquisition devices so that wire chambers may be read out, latches set,

analog to digital converters are gated, etc. The MG also inhibits subsequent triggers while the second level trigger is evaluated. It applies more stringent requirements on the event. If it is satisfied, the state of the spectrometer is stored on magnetic tape, otherwise the readout of the event is stopped, the data aquisition is reset and becomes available for the next MG.

3.7.1 First Level Trigger

The first level is derived from several scintillators. A schematic diagram of the trigger counters in the region of the experimental target is shown in Figure 3.3. *TR1* lies between the target and the microstrips. It ensures there are charged particles coming from the target. *TR2* lies downstream of the microstrips and requires that the particles that fired TR1 also go through the microstrips.

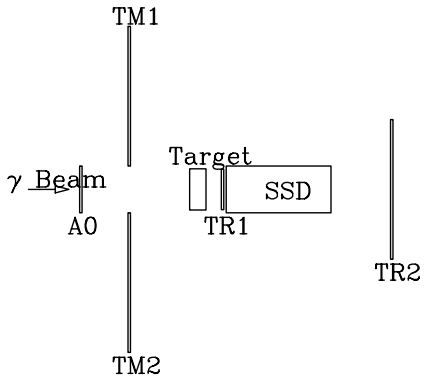

Figure 3.3 Schematic Diagram of the trigger scintillation counters in the region of the experimental target.

This arrangement of the $TR1$ and $TR2$ counters also facilitates noise reduction in the $TR2$ signal. By requiring a time coincidence (i.e., $TR1 \cdot TR2$) we veto hits in $TR2$ due to Compton scattering of soft photons. On the other hand, the Compton scattered electrons would not have sufficient energy to make it thought the microstrips to fire $TR2$.

We ran with several combinations of veto requirements. The large TM counters, located upstream of the target, are intended to veto events with a muon coming from interactions in the primary production target. There are also two

small counters, A0 and A1, in the photon beam to reject events with hadrons in the beam. The TR counters and the vetoes are combined into a signal called T given by the following logical expression -

$$T = \overline{A0} \cdot TR1 \cdot TR2 \cdot \overline{(TM1 + TM2)}$$

To require wide angle tracks in the event we use a scintillator hodoscope called H×V. This array of a layer of horizontal paddles crossed with a layer of vertical paddles lies immediately downstream of M2, just after the last PWC station. A vertical gap (of about 8cm) allows pairs from conversion of beam photons to pass. A logic module computes if the pattern of hits is consistent with at least one particle ($H \times V_1$) or more than one ($H \times V_2$). Another single layer of scintillator mounted on the upstream end of of the outer electromagnetic calorimeter is called OH. The full requirement of the MG is then

$$T \cdot (H \times V_2 \ + \ H \times V_1 \cdot OH)$$

although some data was restricted to the $H \times V_2$ component.

3.7.2 Second Level Trigger

When the second level trigger is evaluated, the modules reading out the PWC system have produced a pulse proportional to the number of hits in each plane. The outputs from all planes are combined and a minimum requirement is made in a logic module. Most of the data required evidence for at least three tracks outside of the pair region. Some data was taken with looser multiplicity requirements.

The most important element in the second level trigger is the HC energy requirement which provides additional rejection against e^+e^- pair events. The charge output of the HC is summed to provide an estimate of the hadronic energy and a minimum deposition is required. The requirement corresponded to roughly 35 GeV in the 1988 run and 40-50 GeV in the 1990 and 1991 runs.

When a MG fires, it holds off further MG's for approximately 100ns while the second level trigger is decided. If the second level trigger is satisfied, further MG's are are again held off until the detector is read out. The combination of these processes gives a typical deadtime of about 25%.

3.8 Coordinate Systems

There are two main coordinate systems employed in analysis. Both have the positive z axis oriented along the beam direction, positive x pointing to the west, and positive y vertically upward. The first system, called the *M2 system*, has the origin at the bend center of M2. The second system, called *granite block coordinates*, has its origin at the upstream edge of the granite block that supports the microstrips; the offset between the two is $\approx$ 1240cm. M2 coordinates are used for analysis of MWPC data and lepton identification while the granite block coordinates are used for analysis of SSD based information such as vertexing.

3.9 Run History

E687 took data during three separate periods which are called the '88, '90, and '91 runs, referring to the year they took place. The '88 run took $\approx$ 60 million hadronic triggers while the '90 and '91 runs each took about 250 million hadronic triggers.

During part of the 1990 run, there were timing problems in the muon proportional tube readout which caused the muon identification to be inefficient. There were also periods where the muon system was moved out of the detector to accommodate tests of the downstream experiment. These periods of no muon identification comprised about 40% of the 1990 luminosity and are removed for analyses involving muons.

Chapter 4

Event Reconstruction, Monte Carlo and Data Skims

This chapter describes how the low level information stored during the E687 data taking is assembled into high level information which is subsequently run through our physics analysis software. We devote special attention to vertex reconstruction and Čerenkov particle identification. Next the Monte Carlo event generation and detector simulation software are detailed, with emphasis on the parameterization of the hadronic energy sum trigger. We close this chapter by describing the process of data skimming, where we reduce the approximately 500 million trigger accepted events into smaller and more managable (and physics-rich!) datasets.

4.1 Event Reconstruction

Event reconstruction is the process of using the raw data collected by the spectrometer (hits in the wire chambers and microstrips, photomultiplier tube ADC counts in the trigger arrays, Čerenkov counters, hadronic calorimeter, etc.) to construct the event topology (track three momentum vectors, particle identification information and total event energy). The key steps in this process are obtaining the microstrip and PWC track parameters, linking PWC and microstrip tracks, momentum measurement, Čerenkov particle identification and constructing the vertex topology of the event.

4.1.1 Microstrip Track Reconstruction

Recall (Sec. 3.2) the microstrip detector consists of twelve planes arranged into four stations of three planes each. Reconstruction of the microstrip tracks begins by finding projections of particle trajectories in the three views. A track must have hits in at least three of the four planes in each view. A linear least squares fit is then performed to solve for the particle trajectory in Cartesian three-dimensional space. The parameters of the fit are the slope and intercept of the

track in the granite block coordinate system. Each track is required to pass a loose χ^2 cut. In this fit hits are shared between tracks and are subsequently arbitrated according to their χ^2 values. Hits not yet associated with a reconstructed track are used to search for wide-angle or highly multiple Coulomb scattered tracks. These tracks are required to have at least six hits.

The transverse resolution of tracks which consist entirely of hits in the high resolution region of the microstrips (extrapolated to the center of the experimental target) is determined to be:

$$\begin{aligned} \sigma_x &= 11\mu m\sqrt{1+\left(\frac{17.5GeV}{p}\right)^2} \\ \sigma_y &= 7.7\mu m\sqrt{1+\left(\frac{25GeV}{p}\right)^2} \end{aligned} \qquad (4.1).$$

The second term in the square root is due to multiple Coulomb scattering in the experimental target, the TR1 counter and the microstrip system.

4.1.2 PWC Track Reconstruction

The reconstruction of tracks in the PWC system is iterative. In the first iteration, simplifications about the magnetic field (i.e., sudden bend approximation) are used to estimate the track parameters in three-dimensional space. This step also performs hit arbitration for shared hits. In later iterations, the effects due to magnetic fringe fields, $\vec{B}$ components in the y and z directions and the position dependence of the $\vec{B}$ field are treated as higher order corrections. We limit the following description to the initial fit.

Like the microstrip tracks, the PWC tracking begins with finding projections in the four views (X, Y U and V) using the PWC hit information. All tracks are required to have hits in the first chamber, $P0$, and cannot have more than four missing hits among the chambers. Furthermore, tracks cannot have more than two missing hits within any single chamber. Projections are combined into

three-dimensional trajectories using a linear least squares fit to the hits in the PWC planes. This fit solves for the x and y intercepts and slopes of the tracks at the center of $M2$. These fit parameters define the three-dimensional Cartesian trajectory of the track witin the PWC system. In addition, the change in slope in the Y view (bend angle) in M2 is calculated for five-chamber tracks. A χ^2 cut is applied to filter out poor fits.

4.1.3 Linking Microstrip and PWC Tracks

The linking process corresponds microstrip track segments to PWC track segments, thereby making it possible to momentum analyze microstrip tracks which pass through M1. It also makes it possible to obtain high quality momentum, slope, and intercept information near the experimental target. Linking is accomplished by comparing the extrapolated positions of SSD and PWC tracks at the center of M1.

4.1.4 Momentum Analysis of Tracks

The momentum of charged tracks is determined by their bend (as measured by the MWPC's and SSD's) in the magnetic fields of M1 and/or M2. The algorithm applies magnetic field corrections. The momentum resolution obtained with the algorithm is,

$$\frac{\sigma_p}{p} = 3.4\% \left(\frac{p}{100\ GeV}\right)\sqrt{1+\left(\frac{17\ GeV}{p}\right)^2}$$

for stubs, and for five-chamber tracks it is

$$\frac{\sigma_p}{p} = 1.4\% \left(\frac{p}{100\ GeV}\right)\sqrt{1+\left(\frac{23\ GeV}{p}\right)^2}$$

4.1.5 Čerenkov Particle Identification

Recalling Table 3.3, charged particles have different threshold momenta for Čerenkov radiation. So for each track traversing a Čerenkov counter, the particle identification software calculates the anticipated light yield in the counters based on a particular particle hypothesis. This predicted yield is also a function of the momentum returned from the momentum analysis. Below we describe the particle identification algorithm.

The analysis begins by setting up an on/off code for every cell in each detector. This is determined by the presence or absence of a phototube pulse height above an ADC cutoff. This cutoff was chosen to exclude the pedestal and corresponds to a few picocoulombs of charge deposited in the ADC. The algorithm then considers every track in each counter individually. First the principal cell that a particular track passed through is determined. Using the momentum of the track, the detector threshold, and a particle hypothesis, the amount of light expected in the principal and adjacent cells is calculated. A track is called *on* by the algorithm when one or more cells is on and some light was expected, and *off* when a reasonable amount of light was expected and the cells are off. If neither condition exists, the track is given a *confused* status.

Once the Čerenkov responses are determined for a track (*on*, *off*, or *confused*), they are compared to the track momentum and the detector thresholds given in Table 3.3. To the extent the three counters agree, the "on"/"off" pattern for each track is combined with the momentum information to place the track into a definite or ambiguous identification category. The Čerenkov response is summarized by a status word whose bits are set to "1" if the track is consistent with a particle hypothesis or "0" if they are inconsistent. Bit 0 represents the consistency with the electron hypothesis, bit 1 the pion hypothesis, bits 2 and 3 the kaon and proton hypotheses, respectively. A status of 2 represents the track is pion definite whereas status 7 represents the track is electron-pion-kaon ambiguous. For example, consider the identification of a five-chamber track whose

momentum is measured as 32 GeV/c. It radiates Čerenkov light in only $C1$ and $C2$. Comparison with Table 3.3 shows this pattern is consistent with the $K^{\pm}$ hypothesis. The Čerenkov status word $ISTATP$ is set to the value 4. The meanings of the $ISTATP$ values are listed in Tab. 4.1 below.

Table 4.1 Čerenkov Identifications

$ISTATP$	Meaning
0	inconsistent information
1	$e^{\pm}$
2	$\pi^{\pm}$
3	$e^{\pm}, \pi^{\pm}$ ambiguous
4	$K^{\pm}$
5	$e^{\pm}, K^{\pm}$ ambiguous
6	$\pi^{\pm}, K^{\pm}$ ambiguous
7	$e^{\pm}, \pi^{\pm}, K^{\pm}$ ambiguous
8	$p^{\pm}$
9	$e^{\pm}, p^{\pm}$ ambiguous
10	$\pi^{\pm}, p^{\pm}$ ambiguous
11	$e^{\pm}, \pi^{\pm}, p^{\pm}$ ambiguous
12	$K^{\pm}, p^{\pm}$ ambiguous
13	$e^{\pm}, K^{\pm}, p^{\pm}$ ambiguous
14	$\pi^{\pm}, K^{\pm}, p^{\pm}$ ambiguous
15	$e^{\pm}, \pi^{\pm}, K^{\pm}, p^{\pm}$ ambiguous

These $ISTATP$ values are the expected identification codes for well isolated (*i.e.* unconfused) tracks in the absence of noise and inefficiencies.

Typical cuts employed in the analysis of reconstructed events are listed in Table 4.2.

Table 4.2 Typical Čerenkov Cuts Applied to Data

Name	Useful for Identifying	Description
NOT HEAVY	$\pi^{\pm}$	NOT e definite, NOT K definite NOT p definite, NOT K/p ambiguous; $ISTATP \neq 1, 4, 8, 12$
Kaon definite	$K^{\pm}$	$ISTATP = 4$
K, KP	$K^{\pm}$	$ISTATP = 4\ OR\ 12$
$KP7$	$K^{\pm}$	$ISTATP = 12$ AND $\|\vec{P}\| < 61.8\ GeV$ **OR** $ISTATP = 7$ AND $\|\vec{P}\| > 61.8\ GeV$

The performance of the Čerenkov system has been studied using topologically identified $\phi \rightarrow K^+K^-$ decays. The invariant mass of this resonance can be reconstructed as a clean peak without relying on the Čerenkov particle identification. The Čerenkov system's ability to identify kaons can be evaluated by seeing how often it obtains the correct identification for the daughter kaons. Specifically, we start with an unbiased sample of fully reconstructed events and reconstruct pairs of oppositely charged tracks as K^+K^-. We require the pair verticize with a confidence level of greater than 1%. In addition, we require one of the tracks be Čerenkov identified as kaon definite ($ISTATP = 4$). In our study we place various identification requirements on the remaining member of the di-kaon pair. We bin the invariant mass to obtain Fig. 4.1 shown below. We use the sidebands indicated on this histogram as an estimate of the distribution of background events under the signal peak. By counting the events in the central signal region

and subtracting the count of events in the sidebands we obtain an estimate of the true di-kaon events in the signal region. The kaon identification efficiency of various kaon selections is listed in Table 4.3. For, example, the efficiency of the $KP7$ cut is defined as

$$\epsilon_{KP7} = \frac{yield\ of\ sideband\ subtracted\ events\ passing\ KP7\ cut}{yield\ of\ sideband\ subtracted\ events\ with\ no\ ISTATP\ cut}$$

where, recall that both the numerator and denominator have the cut that at least one member of the di-kaon pair is kaon definite. This kaon "efficiency" reflects both the Čerenkov system performance as well as the momentum spectrum for observed $\phi \to K^+K^-$ daughters.

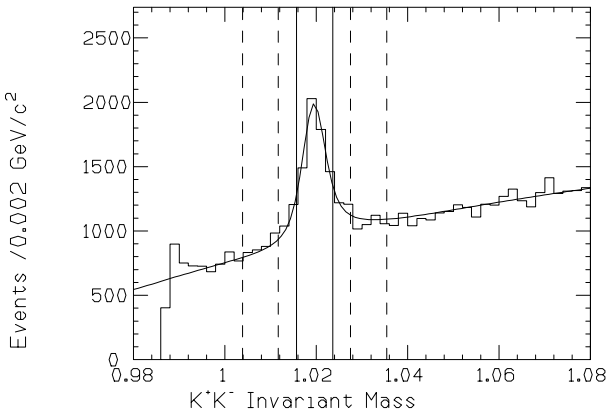

Figure 4.1 Invariant mass of the topologically reconstructed K^+K^- sample for determining kaon Čerenkov identification efficiency. Solid vertical lines indicate the signal region, dashed vertical lines delimit the sidebands.

Table 4.3a Kaon Detection Efficiency for 3-Chamber Tracks

$K^{\pm}$ ČerenkovCut	1990 Run	1991 Run
$KP7$	0.371 ± 0.088	0.433 ± 0.088
K, KP	0.747 ± 0.139	0.712 ± 0.126
Kaon Definite	0.374 ± 0.079	0.279 ± 0.064

Table 4.3b Kaon Detection Efficiency for 5-Chamber Tracks

$K^{\pm}$ ČerenkovCut	1990 Run	1991 Run
$KP7$	0.453 ± 0.044	0.457 ± 0.034
K, KP	0.689 ± 0.060	0.665 ± 0.045
Kaon Definite	0.238 ± 0.027	0.210 ± 0.019

Recent studies [25] conclude the inefficiencies are reasonably reproduced by the Monte Carlo detector simulation - *eg post hoc* Čerenkov corrections are not necessary.

4.1.6 Vertex Reconstruction

E687 exploits the three-dimensional separation between the charm production point (primary vertex) and the charm decay point (secondary vertex) to separate charm signals from noncharm background. Two algorithms are in use: the *candidate driven algorithm* and the *stand alone algorithm.* We presently describe these two methods.

4.1.6.1 Candidate Driven Vertex Reconstruction Algorithm

Consider the decay process $D_s^+ \to K^+K^-\pi^+$. The decay daughters' momentum vectors are reconstructed by the microstrip and PWC system. The vertexing software requires that the daughter PWC tracks be linked to microstrip tracks. Candidate daughter tracks are intercepted to form the decay vertex in three-dimensional space. The algorithm calculates a χ^2 by summing over the tracks in the vertex fit according to

$$\chi^2 = \sum_{i=1}^{N} \left(\frac{x_v - (x_i + x_i' z_v)}{\sigma_{x,i}} \right)^2 + \left(\frac{y_v - (y_i + y_i' z_v)}{\sigma_{y,i}} \right)^2 \qquad (4.4)$$

and returns the confidence level (DCL) of this fit to the decay vertex. The track parameters (x_i, x_i', y_i, y_i') are obtained from the microstrip or PWC track

reconstruction routines, whereas the vertex fit parameters are (x_v, y_v, z_v). The errors are due to extrapolating the track to the fitted vertex. The Cartesian sum of the momentum vectors emanating from the decay vertex becomes the candidate parent track's momentum vector. We construct the associated track parameters for this so-called 'seed' track (x_s, x'_s, y_s, y'_s) This step differentiates the candidate driven vertex reconstruction algorithm from the stand-alone algorithm to be described in the next section. The seed track is assumed to go through both the primary and secondary vertices. It is intercepted with leftover tracks not in the secondary vertex in order to form the primary vertex. These leftover tracks are intercepted with the parent track and assigned to the primary vertex as long as the confidence level of the resulting vertex (PCL) exceeds 1%. The candidate vertex algorithm calculates the signed three-dimensional separation between the vertices (ℓ) as well as its error (σ_ℓ). One of the most important cuts in E687 data is the statistical significance of detachment between the primary and secondary vertices, ℓ/σ, which is essentially a lifetime cut.

Another important feature of the algorithm is the ability to form isolation cuts to suppress backgrounds. The confidence level that a charm daughter track is in the primary vertex ($CL1$, also called 'point back isolation confidence level') is often required to be below 0.15. CL1 effectively suppresses non-charmed backgrounds. It usually depends critically on the multiplicity of the final state being considered, since more final state tracks facilitate formation of a good vertex. It is calculated by looping over the tracks in the secondary vertex. For each secondary track we re-verticize the primary vertex using the original primary and a given secondary track. The value of CL1 is the highest confidence level resulting from this process.[1] The confidence level that other tracks (excluding the secondary and primary tracks) is near the secondary ($CL2$, also called 'secondary

1 The background process $D^{*0} \to D^0\pi^+ \to (K^+K^-)\pi^+$ is effectively removed by the point back isolation confidence level cut. It can be mistaken for the process $D^0 \to K^-\pi^+$ because the low momentum pion points back to the primary vertex. By requiring the charm daughters miss the primary vertex, one can reject this contamination.

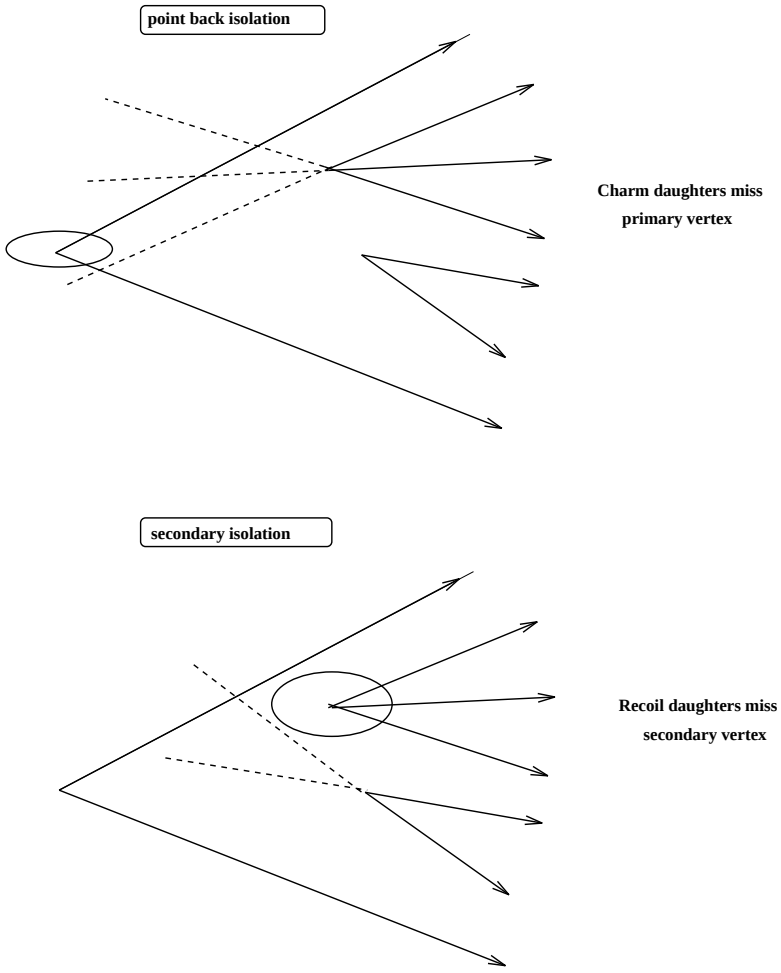

Figure 4.2 Schematic representation of isolation cuts CL1 (top) and CL2 (bottom).

vertex isolation confidence level') is usually required to be less than 0.0001. CL2 suppresses backgrounds from higher multiplicity charm final states which "feed down" into the state being considered. For example, the secondary vertex isolation confidence level cut removes contamination of candidate $D^+ \to K^-\pi^+\pi^+$ events with $D^0 \to K^-\pi^+\pi^+\pi^-$ decays. The operation of these isolation cuts is schematically illustrated in Fig. 4.2. The evolution of the signal in a sample

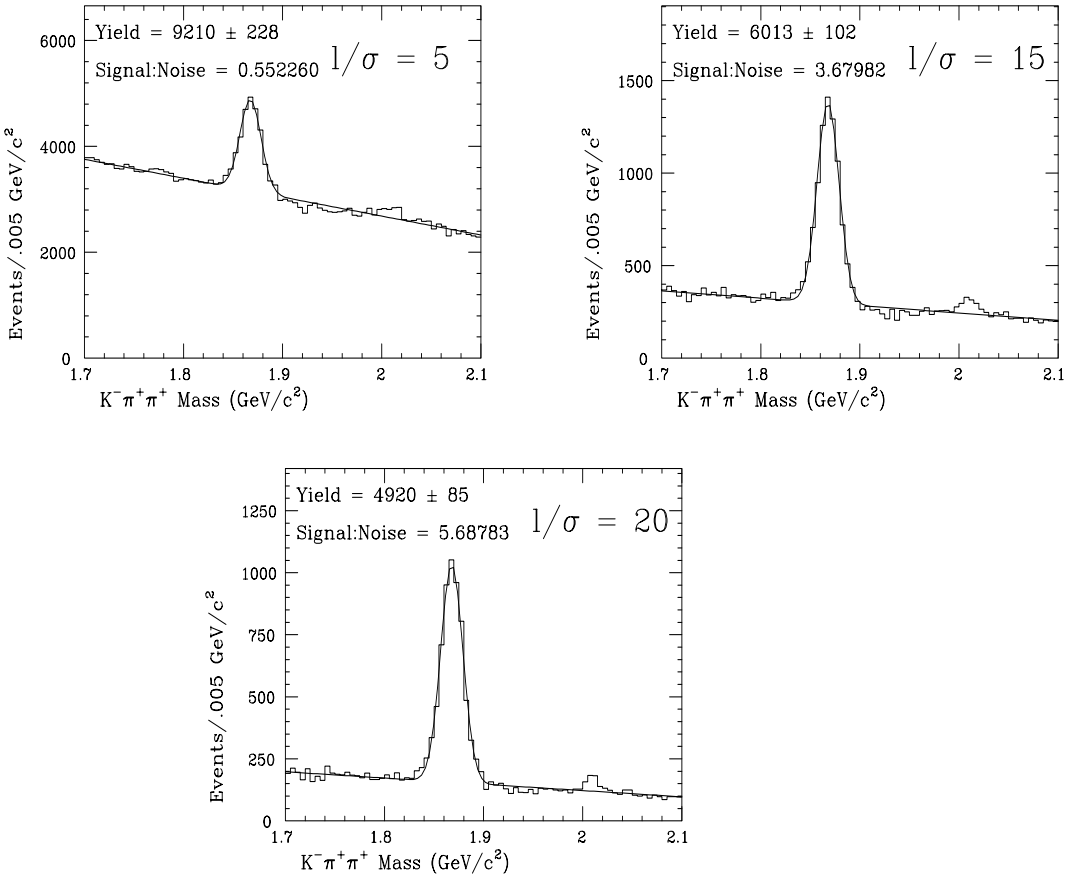

Figure 4.3 Invariant mass histograms for $D^+ \rightarrow K^-\pi^+\pi^+$ candidates with $DCL > 0.01$ and the indicated vertex separation cuts. Harder significance of detachment cuts isolate the charm signal and reject non-charm background. The bump at $2.01 GeV/c^2$ is due to $D^{*+} \rightarrow D^0\pi^+ \rightarrow (K^-\pi^+)\pi^+$ decays.

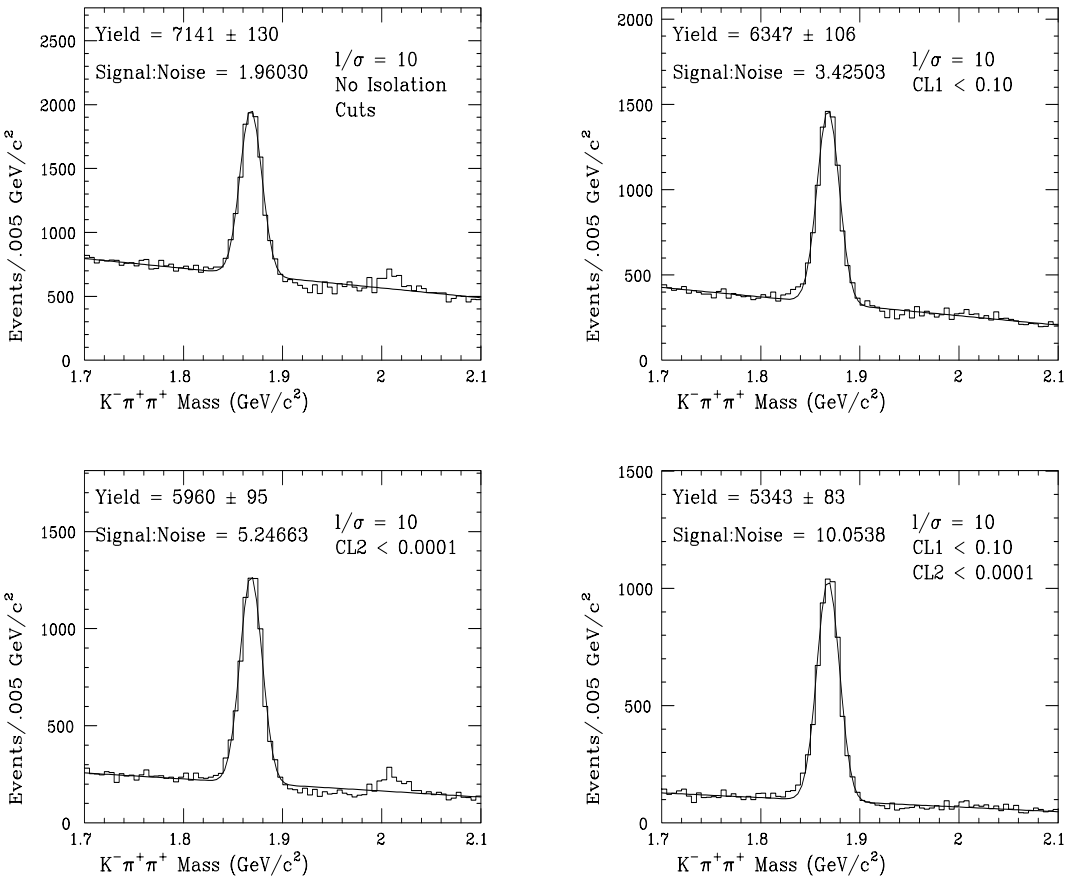

Figure 4.4 Invariant mass histograms for $D^+ \to K^-\pi^+\pi^+$ candidates with $DCL > 0.01$, $\ell/\sigma > 10$ and the indicated isolation cuts. Note the D^{*0} peak (from $D^{*+} \to D^0\pi^+ \to (K^-\pi^+)\pi^+$ decay) at 2.01 GeV/c^2 on the $CL2 < 0.0001$ sample disappears once the $CL1 < 0.10$ cut is applied. This phenomenon illustrates the "pointback isolation" behavior of the $CL1$ cut.

of $D^+ \to K^-\pi^+\pi^+$ decays as harder and harder cuts on ℓ/σ, CL1 and CL2 are applied is demonstrated in Figs. 4.3 and 4.4.

4.1.6.2 Stand-Alone Vertex Reconstruction Algorithm

This alternative vertexing algorithm searches for vertices without reference to a particular charm candidate track. It iteratively intersects tracks to obtain the entire vertex topology of the event. Linkage of the tracks is not a requirement - it only uses the microstrip information. It requires the secondary track be downstream of the primary.

4.2 Monte Carlo

A typical high energy physics measurement involves counting the number of detected particles of a particular type. This process is made considerably more challenging by the presence of inefficiencies in equipment and techniques, causing the number of detected particles to not equal the number of particles created in a reaction. Among the causes of these detection inefficiencies are: the limited geometrical acceptance of the spectrometer; deficiencies in the reconstruction and analysis software; tracking errors due to multiple Coulomb scattering; hadronic absorption; electronic noise in the spectrometer hardware. In order to assess the effects these processes have on our analysis, it is necessary to model the spectrometer's performance. Monte Carlo software accomplishes this task in two steps: particle energy-momentum four-vectors are generated according to known (and postulated) physical processes (i.e., the photon-gluon fusion mechanism); these particles (and their decay daughters) are propagated through a simulation of the E687 hardware. A brief description of these steps follows below.

The E687 Monte Carlo program employs the LUND/Pythia [26] software package to generate charm particles according to the photon-gluon fusion mechanism described in Chap. 1. One member of the $c\bar{c}$ pair is selected to hadronize into a user specified charm hadron (say a D^+ or a D_s^+) while the remaining

quark is allowed to hadronize according to the known branching ratios [28]. The hadronization model employed by LUND/Pythia is illustrated in Fig. 4.5 below.

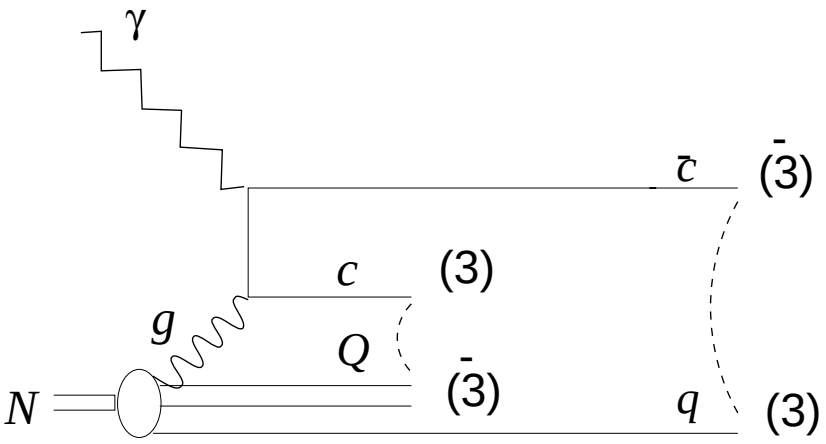

Figure 4.5 Illustration of the LUND/Pythia string framentation model. Our Monte Carlo particle generator uses this model to hadronize the photoproduced charm $-$ $\overline{\text{charm}}$ pair. In order to conserve color, the nucleon resolves itself into a color quark (q) and anticolor diquark (Q). The charm quark must dress in the same string as the diquark, leaving the anticharm to dress in a string with the quark. [27]

The generated charm particles are propagated through the spectrometer simulation software and allowed to decay according to a user specified matrix element, usually phase space (i.e., nonresonant). An important application of the amplitude analysis described in Chapters 5 and 6 is to decay the charm hadrons according to the physical matrix elements. The device simulation and particle generation routines mimic e^+e^- showers, hadronic absorption, eletronic inefficiencies in the MWPC system and multiple Coulomb scattering. The simulation also models the time dependent changes in spectrometer performance. An example of this effect was evidenced in Table 4.3, where it is apparent there is a difference in the 1990 performance of the Čerenkov system and its performance in 1991. A standard raw data tape is produced which is subsequently run through

the standard event reconstruction and analysis software.

An important component of the device simulation is the hadronic energy sum trigger which, as described in Sect. 3.7 is an essential component of the second level trigger and hence is crucial for determining the overall counting efficiency. Because the detector simulation software does not model hadronic energy response using hadronic shower simulations, we parameterize the response of the hadronic energy sum trigger from the data in terms of the total "charged" momentum striking the calorimeter face outside of a central hole (the CHC region). The tracks which enter this momentum sum (also called our effective energy sum), $\sum^{quality\ tracks} |\vec{P}_{track}|$, must satisfy the following requirements:

a) Five-chamber linked tracks: the 5-chamber cut selects tracks which travel through P4 and hence have a high probability of traversing the hadron calorimeter. The linking requirement permits us to require the track is related to a high quality hadron production vertex.

b) Not photon beam related $\gamma \rightarrow e^+e^-$ photon conversion electron. Because these e^+e^- pairs are created with low transverse momentum, they travel at very shallow angles with respect to the beam. So this cut merely removes low angle tracks.

c) The reconstructed track must be consistent with coming from a hadronic vertex reconstructed by the stand-alone vertex algorithm. This cut requires

$$\frac{|X_{vertex} - X_{track}|}{\sigma_{X_{track}}} \leq 3$$

X_{track} = X coordinate of the track projection in the plane defined by the Z coordinate where the vertex is reconstructed (with position $\vec{r}_{vertex}$). $\sigma_{X_{track}}$ is the error in the track projection. Association with a vertex reconstructed by the microstrip vertexer rejects spurious PWC tracks as well as tracks due to decay daughters from long-lived vees (i.e., $K^0_s \rightarrow \pi^+\pi^-$).

d) The track cannot have embedded pairs. An embedded e^+e^- pair is produced upstream of the experimental target (in the radiator) and travels through it. Hence they become 'embedded' in a legitimate multihadronic event and can confuse the microstrip vertexing algorithm.

e) The track must come from a well determined production vertex which is obtained from the intersection of three or more tracks. Recall (Sec. 4.1.6) that the primary vertex is obtained by intersecting tracks as long as they are consistent with coming from the same vertex.

We chose these cuts because only a very small, prescaled portion of our data is suitable for measuring hadronic energy busline response.[2] Furthermore, this heavily prescaled unbiased sample is very seriously contaminated by e^+e^- pairs. We require topological cuts be satisfied in order to

(*i*) eliminate Bethe-Heitler events;

(*ii*) avoid including the momentum from e^+e^- daughters in the momentum sum (since they presumably leave very little energy in the calorimeter).

Finally there is the issue of how to deal with neutral hadrons ($K_L^{0'}s$ and neutrons) in the simulated energy sum. We don't detect these hadrons in the measured response, but we could in principle include them in the simulated sum for Monte Carlo events. We simulate under the assumption that $K_L^{0'}s$ and neutrons are rarely produced in unbiased photoproduced hadronic events but are more prevalent in charm events. For this reason we include them in the simulated energy sum.

The resulting plot is shown in Fig. 4.6. In this plot the status of the hadronic trigger (1 or 0) is histogrammed in bins of the track energy sum described above.

2 Recall HC busline response is part of our second level trigger.

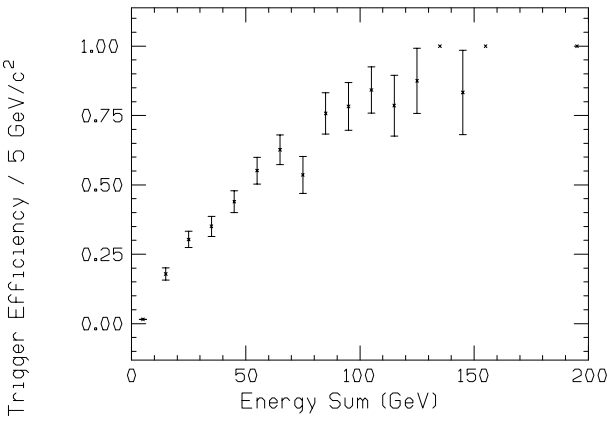

Figure 4.6 Hadronic energy trigger efficiency parameterization.

In the Monte Carlo simulation, the energy of tracks which pass through the hadronic calorimeter is summed and the state of the hadronic energy trigger is determined by Monte Carlo rejection with respect to the curve in Fig. 4.6.

By comparing the number of generated and reconstructed events in a Monte Carlo sample, it is possible to assess the time-averaged effects of the inefficiencies in event triggering and reconstruction.

4.3 Data Skims

The entire 1990-1991 raw E687 data sample consists of approximately 4000 8mm magnetic data storage tapes. Each tape is run through the event reconstruction software described in Section 4.1. E687 used a 'farm' of IBM RISC and Silicon Graphics workstations to accomplish this task. Because high quality charm events are rare in E687 data, it would be very inefficient to run all 4000 reconstructed tapes through the high level analysis software. For this reason, the reconstructed data is first run through skimming routines to select events (and store on tape) which are likely to contain charm and therefore reduce the number of data tapes to analyze.

4.3.1 All-Charged Skim

The *EZDEE skim* begins by looping over all combinations of charged tracks with charges and Čerenkov particle identification consistent with coming from known (up to multiplicity 6) decays of the D_0, D^+ and D_s^+. Those in combinations over a large invariant mass range (typically Mass $> 1.6 GeV/c^2$) are then run through the candidate driven vertex finder. Charm candidates satisfying minimal detachment and vertex quality cuts are then written to tape. This skim is essentially 100% efficient at selecting reconstructable charm hadrons which decay into an all-charged final state through the candidate driven vertex technique.

4.3.2 Global Vertex Skim

The *Global Vertex skim* is somewhat less efficient but puts no reliance on a specific exclusive final state topology. It is independent of particle identification. It intersects pairs of tracks to form pair vertices, and demands that at least two pair vertices are separated by 4σ. It also requires the confidence level of these two vertices exceeds 0.01.

Chapter 5

The $D^+, D_s^+ \to K^+K^-\pi^+$ Dalitz Plots

In this chapter we analyze the decay $D^+, D_s^+ \to K^+K^-\pi^+$ (and charge conjugate). We will show that the K^+K^- spectrum is dominated by the intermediate ϕ resonance and $K^-\pi^+$ spectrum is dominated by the $\overline{K}^*(892)^0$ resonance. Dramatic differences will be found between the D^+ and the D_s^+ involving the mixtures of participating intermediate decay channels and their relative strengths.

The chapter begins with a description of the cuts employed to bring out the signal. Background sources are discussed in detail. We continue this chapter by applying the phenomenology of Chap. 2 to the analysis of the amplitude for the decays $D^+, D_s^+ \to K^+K^-\pi^+$. Our checks for systematic effects are described. The quality of the fit is discussed - we will find that although we believe our fit is technically correct, the descrepancies between the fit and the data indicate that weaknesses of our model. Finally, we use our results on the D^+ amplitude to extract branching fractions.

5.1 The $D^+, D_s^+ \to K^+K^-\pi^+$ Signal

Starting with the EZDEE skim tapes (Sec. 4.3.1), we search for three-body final states where two tracks (the kaon candidates) are Čerenkov identified as kaon or kaon/proton consistent ($ISTATP = 4$ *or* 12) and the remaining track (the pion candidate) passes the .NOT. HEAVY cut ($ISTATP \neq 1, 4, 8, 12$). These tracks are combined to form the secondary vertex which is required to have a confidence level (DCL) greater than 1%. The secondary must be separated from the primary by at least eight standard deviations ($\ell/\sigma > 8$). We also require the secondary be well isolated from the primary by requiring the candidate $K^+K^-\pi^+$ tracks form a vertex with the tracks in the primary with a confidence level less than 20% (CL1). Isolation is improved by rejecting combinations where leftover tracks (i.e., tracks not in the secondary and primary) form a vertex with the secondary vertex with a confidence level (CL2) greater than 0.1%. Because the

raw data was collected with different second-level trigger requirements, we remove events where the hadronic trigger is not satisfied.

The above cuts (the *baseline cuts*) effectively remove non-charm background (background due to track reconstruction errors, errors in pattern recognition in the microstrips, etc.). We studied two sources of charm background: $D^+ \rightarrow K^-\pi^+\pi^+$ and $D^{*+} \rightarrow D^0\pi^+ \rightarrow (K^+K^-)\pi^+$. Removing these backgrounds is discussed in detail below in Sections 5.1.1 and 5.1.2. After filtering out these background signals we obtain the sample characterized in Table 5.1, the so-called *full dataset*. This sample is used for the analysis described in this chapter. The mass histogram is shown in Figure 5.1 below. The figure also shows the so-called *airgap* sample, which we collected in order to study background systematics. These $K^+K^-\pi^+$ candidates are required to verticize in the space downstream of the experimental target and upstream of the next detector component, the $TR1$ veto counter (see Fig. 3.3). To accomplish this cut we define the normalized displacement of the decay vertex from the target and the $TR1$ counter, $Z^{norm}_{secondary}$ and Z^{norm}_{TR1} :

$$Z^{norm}_{secondary} = \frac{Z_{secondary\ vertex} - Z_{targ}}{\sigma(Z_{secondary\ vertex})} \tag{5.1}$$

$$Z^{norm}_{TR1} = \frac{Z_{secondary\ vertex} - Z_{TR1}}{\sigma(Z_{secondary\ vertex})} \tag{5.2}$$

For the airgap sample we require $Z^{norm}_{secondary} > 3$ and $Z^{norm}_{TR1} < -3$ This cut sharply reduces charm background due to hadronic re-interactions in the beryllium target. The statistics of the airgap sample are listed in Table 5.2 below. Superimposed on the histogram is a Gaussian + linear polynomial fit, $\mathcal{G} + \mathcal{P}$. The signal region is defined as $\pm 2\sigma$ about the reconstructed charm meson mass.[1] In order to estimate the background distribution we also define sideband regions and assume the distribution of events in the sidebands is the same as the distribution of background events in the signal region. In Section 5.2.1 we describe in detail

1 Here, σ represents the fitted width of the mass histogram (the three-body mass resolution).

how we use the sidebands to characterize the background events.

Table 5.1 Full Dataset Sample Statistics

Parameter	D^+	D_s^+
Fitted Yield	922 ± 38	725 ± 36
Mass (GeV/c^2)	$1.869 \pm .0004$	$1.968 \pm .0005$
Width σ (GeV/c^2)	$.0079 \pm .00034$	$.0091 \pm .00047$
Signal Fraction $\mathcal{F}_0$	$.745 \pm .0305$	$.710 \pm .0339$
Overall Efficiency (%)	$3.81 \pm .0180$	$1.75 \pm .013$

Table 5.2 Airgap Sample Statistics

Parameter	D^+	D_s
Fitted Yield	351 ± 20	250 ± 18
Mass (GeV/c^2)	$1.8695 \pm .0004$	$1.9671 \pm .0007$
Width σ (GeV/c^2)	$.0070 \pm .0004$	$.0096 \pm .0006$
Signal Fraction $\mathcal{F}_0$	$.919 \pm .005$	$.899 \pm .008$

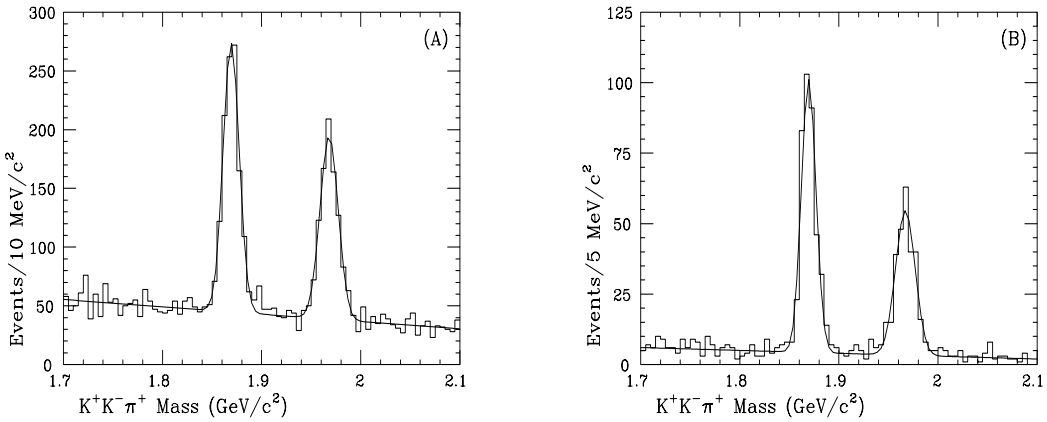

Figure 5.1 Invariant mass of histogram of $K^+K^-\pi^+$ candidates used for this analysis: A) the full data sample; B) the airgap sample.

The signal fraction $\mathcal{F}_0$ is $\int_{\substack{signal\\region}} \mathcal{G} dm_{KK\pi} / n_{\substack{signal\\region}}$, where $n_{\substack{signal\\region}}$ is the number of events counted in the signal region (see the following table). Table 5.3 summarizes our choice of sideband and signal regions. The sidebands are of equal width (4σ) and are separated from the signal region limits by 2σ for the D^+ low sideband, 1σ for the D^+ high sideband, 1σ for the D_s^+ low sideband and 2σ for the D_s^+ high sideband.

Table 5.3 Signal and Sideband Regions, Full Dataset

Region	Mass cut (GeV/c^2)	Events
D^+ low sideband	$1.805 < m(KK\pi) < 1.837$	317
D^+ signal region	$1.853 < m(KK\pi) < 1.885$	1173
D^+ high sideband	$1.893 < m(KK\pi) < 1.925$	312
D_s^+ low sideband	$1.905 < m(KK\pi) < 1.941$	307
D_s^+ signal region	$1.950 < m(KK\pi) < 1.986$	958
D_s^+ high sideband	$2.004 < m(KK\pi) < 2.040$	218

Likewise, we list the signal and sideband limits for the airgap sample in Table 5.4 below.

Table 5.4 Signal and Sideband Regions, Airgap Sample

Region	Mass cut (GeV/c^2)	Events
D^+ low sideband	$1.8135 < M(KK\pi) < 1.8415$	30
D^+ signal region	$1.8555 < M(KK\pi) < 1.8835$	370
D^+ high region	$1.8905 < M(KK\pi) < 1.9185$	32
D_s low sideband	$1.8999 < M(KK\pi) < 1.9383$	40
D_s signal region	$1.9479 < M(KK\pi) < 1.9863$	273
D_s high region	$2.0055 < M(KK\pi) < 2.0439$	14

The Dalitz scatterplots for signal region events are shown below in Fig. 5.2.

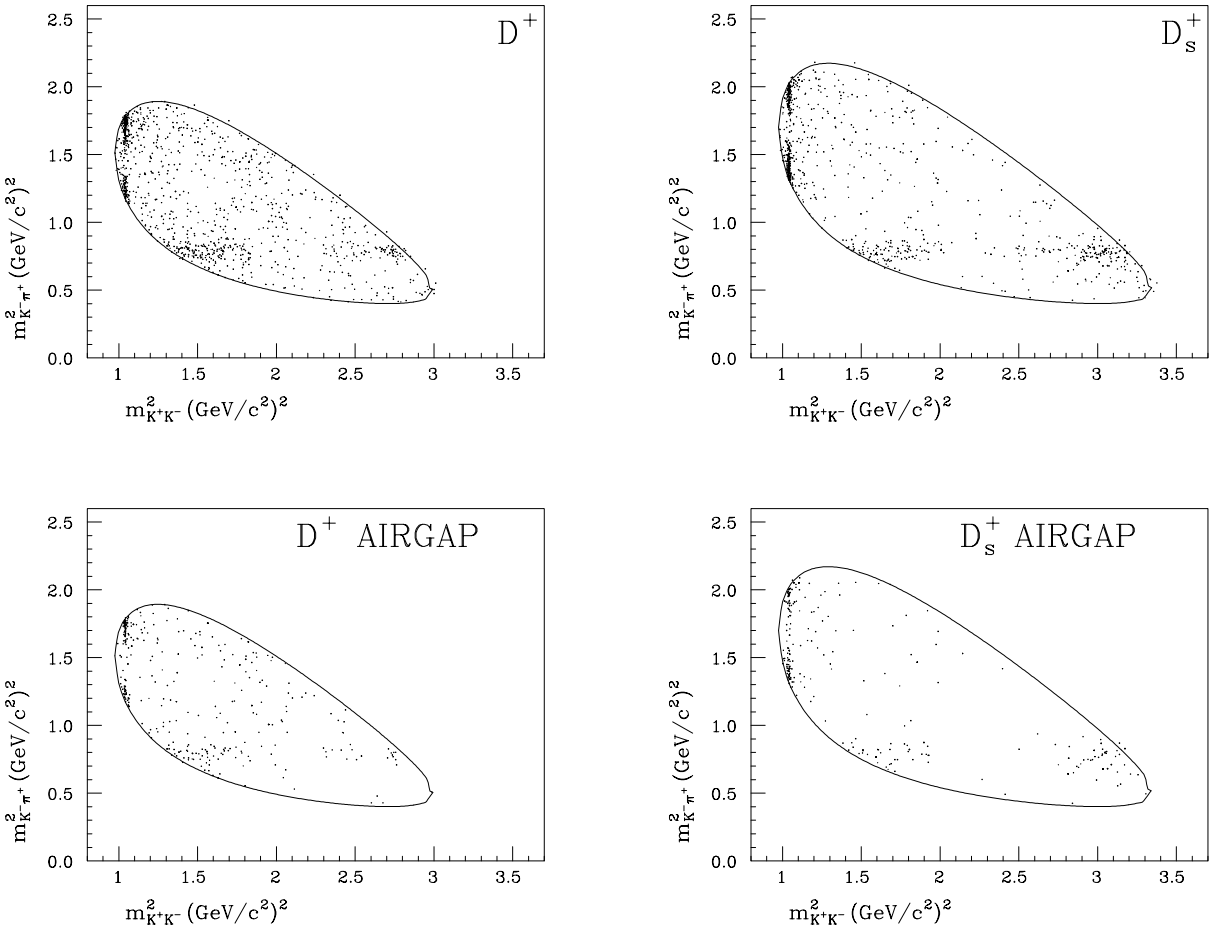

Figure 5.2 Dalitz scatterplots for $K^+K^-\pi^+$ samples. Top row is the full dataset sample , bottom row the airgap samples. The full dataset is used used to obtain our nominal analysis results. The airgap sample is used to assess systematic effects due to charm background (Sec. 5.4.2) and to help identify participating resonances in the D_s^+ decay (Sec. 5.3.2).

5.1.1 $D^+ \to K^-\pi^+\pi^+$ Contamination

An important source of background in the signal is the copious yield of $K^-\pi^+\pi^+$ from the Cabbibo favored decay of the D^+ meson. These final states are Čerenkov misidentified as $K^-\pi^+K^+$. We study this effect by reconstruct-

ing each $\underline{K}^+K^-\pi^+$ candidate as $\underline{\pi}^+K^-\pi^+$ and plotting the result in Figure 5.3. This plot is for $KK\pi$ candidates over the full histogrammed range from $1.7GeV/c^2 < m(K^+K^-\pi^+) < 2.1GeV/c^2$. This so-called *reflection* appears as an extended shoulder above the D_s peak in Figure 5.3b. Comparison of figures 5.3a and 5.1 shows that the contamination is of order the D_s^+ yield in the final sample. To remove this contamination we simply require the $K^-\pi^+\pi^+$ mass be outside the 2σ region in Figure 5.3a[2] . We will return to this cut in Sect. 5.2.5.

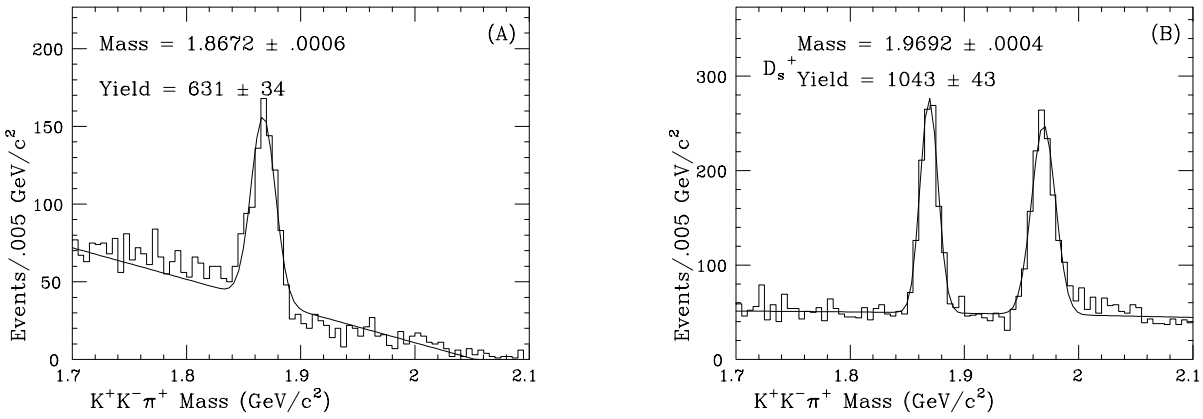

Figure 5.3 Invariant mass of histograms which demonstrate contamination by Cabbibo favored $D^+ \to K^-\pi^+\pi^+$ decays: A) obtained by calculating the 3-body mass with the $K^-\pi^+\pi^+$ hypothesis; B) $K^+K^-\pi^+$ with all cuts except the anti-reflection cut imposed. Note the long tail above the D_s^+ mass peak due to Čerenkov misidentified $D^+ \to K^-\pi^+\pi^+$ decays.

5.1.2 $\underline{D^{*+} \to D^0\pi^+ \to (K^+K^-)\pi^+}$ Contamination

The final state of this background process is identical to our analysis sample, so it appears on the Dalitz plot at $m^2_{KK} = m^2(D^0) = 3.48(GeV/c^2)^2$. This background shows up in the upper sideband of the D_s Dalitz plot in Figure 5.4, where we plot the upper sideband scatterplot of the data. We confirm our claim this contamination is due to $D^0 \to K^+K^-$ by plotting the Dalitz plot

2 We choose the D^+ reflection region to be $1.846 < m(K^-\pi^+\pi^+) < 1.888$.

(Figure 5.4b) for a $c\bar{c}$ phase space Monte Carlo sample that has passed our analysis cuts. We see an acumulation of points in the same region. Note there is very little contamination in the signal region. By cutting candidates with $m^2_{KK} > 3.4(GeV/c^2)^2$ we remove this background.

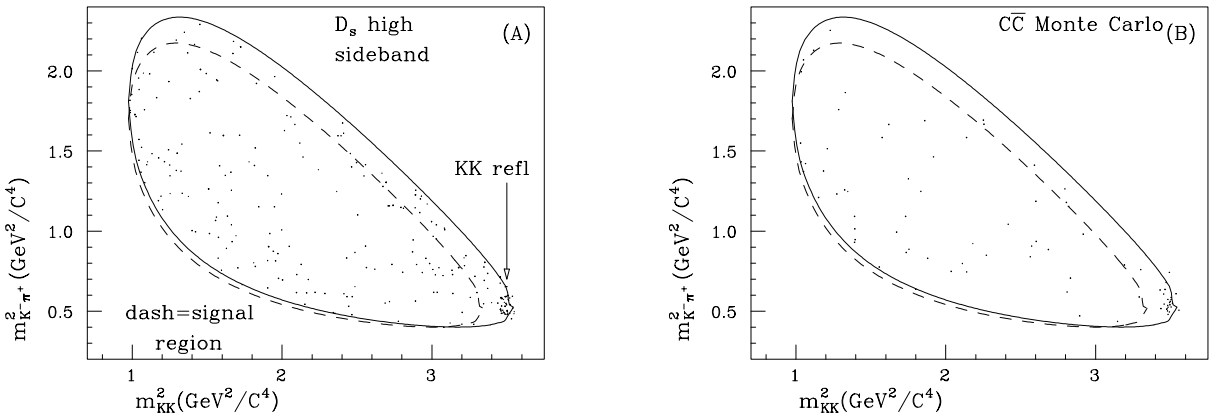

Figure 5.4 Dalitz scatterplots demonstrating contamination from $D^{*+} \to D^0\pi^+ \to (K^+K^-)\pi^+$ decay. In both figures, the solid line represents the Dalitz boundary for the central value of the high mass sideband and the dashed line is the boundary for the center of the signal region: A) Dalitz plot for events in the upper-sideband of the D_s^+ sample; B) Dalitz plot for events generated from a phase-space $c\bar{c}$ Monte Carlo.

5.2 The $D^+, D_s^+ \to K^+K^-\pi^+$ Analysis Formalism

Because the amplitude for the D^+ decay is simpler (i.e., we include fewer intermediate decay channels in the final D^+ fit), we will use it to illustrate the analysis formalism. In Sections 5.3.1 and 5.3.2 we motivate our selection of amplitudes which participate in the amplitude fits.

Recalling Equation 2.11, we write the amplitude for our $D^+ \to K^+K^-\pi^+$ signal as a coherent superposition of $\overline{K}^*(892)^0K^+$, $\phi\pi^+$ and $\overline{K}_0^*(1430)K^+$ ampli-

tudes as follows:

$$\begin{aligned}\mathcal{A}(D^+ \to K^+K^-\pi^+)_s &= a_{\overline{K}^*(892)^0}\ e^{i\delta_{\overline{K}^*(892)^0}} P(\pi^+K^-K^+|\overline{K}^*(892)^0) \\ &+ a_\phi\ e^{i\delta_\phi} P(K^+K^-\pi^+|\phi) \\ &+ a_{\overline{K}^*_0(1430)}\ e^{i\delta_{\overline{K}^*_0(1430)}} S(\pi^+K^-K^+|\overline{K}^*_0(1430))\end{aligned} \tag{5.3}$$

Here we have used the notations P and S introduced in Table 2.1, to represent $p-wave$ and $s-wave$ intermediate resonances. Because CP violation in the D sector is thought to be small [29] we obtain the amplitude for the D^- by replacing all particles with their associated antiparticles in Eq. 5.3.

$$\begin{aligned}\mathcal{A}(D^- \to K^-K^+\pi^-)_s &= a_{K^*(892)^0}\ e^{i\delta_{K^*(892)^0}} P(\pi^-K^+K^-|K^*(892)^0) \\ &+ a_\phi\ e^{i\delta_\phi} P(K^-K^+\pi^-|\phi) \\ &+ a_{K^*_0(1430)}\ e^{i\delta_{K^*_0(1430)}} S(\pi^-K^+K^-|K^*_0(1430))\end{aligned} \tag{5.4}$$

Note that we have not inverted the relative strong phase shifts δ_ϕ and $\delta_{K^*(1430)}$.[3]

The fit amplitudes a_i and phases δ_i are the parameters which we determine in the procedure. We use the $\overline{K}^*(892)^0$ as the reference channel and set $a_{\overline{K}^*(892)^0} = 1$ and $\delta_{\overline{K}^*(892)^0} = 0$.[4] The terms $\mathcal{M}_i(abc|r_i)$ are functions of the Dalitz plot variables $m^2_{K^+K^-}$ and $m^2_{K^-\pi^+}$. They are listed in Table 2.1. The notation is significant because it defines the phase convention. One obtains the signal probability density function pdf_s by multiplying $\mathcal{A}_s$ by its complex conjugate, being careful to maintain normalization:

$$pdf_s = \epsilon(m^2_{KK}, m^2_{K^-\pi^+}) \times \frac{\mathcal{A}_s\mathcal{A}_s^*}{\mathcal{N}_s} \tag{5.5}$$

The efficiency correction function, $\epsilon(m^2_{KK}, m^2_{K\pi})$, is discussed below in Section 4.2.2. The normalization constant $\mathcal{N}_s$ is merely the integral of $\epsilon \times \mathcal{A}_s\mathcal{A}_s^*$ across

3 See chapter 9 of Ref. [30].

4 Recall the comments near the end of Sec. 2.3.

the Dalitz plot:

$$\mathcal{N}_s = \int\limits_{Dalitz\ Plot} \epsilon \mathcal{A}_s \mathcal{A}_s^* dm^2_{KK} dm^2_{K^-\pi^+} \tag{5.6}$$

We use a maximum likelihood method to solve for the fit parameters a_i and δ_i. The likelihood is the product of *pdf*'s for the entire sample:

$$\mathcal{L}_{sr}(\vec{x};\vec{\alpha}) = \prod_{\text{events i}} pdf_i.$$

In this notation the signal region likelihood is a function of the measured observables $\vec{x}$ and the fit parameters $\vec{\alpha}$. For the present analysis $\vec{x} = \left(m^2_{KK}, m^2_{K^-\pi^+}\right)$ and $\vec{\alpha} = \left(\vec{a}, \vec{\delta}\right)$. Our method is to minimize the function $w_{sr} = -2\ln\mathcal{L}_{sr}$ in order to obtain the fit parameters $\vec{\alpha}$. Note that it is a continuous function (as opposed to a binned function) of the mass-squared variables and hence provides us with maximum information regarding interference between channels.

At this point we run into our first complication - "how do we deal with the background?" The last equation contains a total probability density function which includes both signal and background. The unfortunate truth of experimental physics is that in spite of our best efforts, the analysis sample is contaminated by background events. So in general, a signal region event may be an actual $KK\pi$ final state from D^+ meson decay or it may be from background. Hence we modify our probability density function by writing it as a superposition of signal and background *pdf*'s as follows:

$$pdf = \epsilon\mathcal{F}\frac{\mathcal{A}_s\mathcal{A}_s^*}{\mathcal{N}_s} + (1-\mathcal{F})\frac{I_{bg}}{\mathcal{N}_{bg}} \tag{5.7}$$

In writing equation 5.7 we have used the observation that identifying an event as 'signal' or 'background' are mutually exclusive occurences. Therefore, we must separately normalize these contributions to the *pdf*. It is also important to note that the efficiency correction ϵ only modulates the signal part of the *pdf*. Since

we make polynomial parameterization of I_{bg} directly from the the data (see Sec. 5.2.1), there is no need to include an efficiency correction in the second term $(1-\mathcal{F})\frac{I_{bg}}{\mathcal{N}_{bg}}$. The normalization integrals $\mathcal{N}_s$ and $\mathcal{N}_{bg}$ are explicitly written[5]

$$\mathcal{N}_s = \int\limits_{DP} \epsilon \; \mathcal{A}_s \mathcal{A}_s^* d\mathcal{DP} \tag{5.8}$$

$$\mathcal{N}_{bg} = \int\limits_{DP} I_{bg} d\mathcal{DP} \tag{5.9}$$

Parameterizing the background involves fitting the sideband events to a model function I_{bg}. The procedure is outlined in the next section.

At this point we have described the function w'_{sr} which is minimized to obtain the optimal fit amplitudes and phases.[6] It contains the signal and background *pdf*'s and takes the form

$$\begin{aligned} w'_{sr} &= -2 \ln \mathcal{L}_{sr} \\ &= -2 \sum_{sr \; \substack{events \\ i}} \ln \left[\epsilon_i \; \mathcal{F} \frac{\mathcal{A}_{s,i} \mathcal{A}^*_{s,i}}{\mathcal{N}_s} + (1-\mathcal{F}) \frac{I_{bg}}{\mathcal{N}_{bg}} \right] \end{aligned} \tag{5.10}$$

In order to allow for the inflation of statistical error bars due to background fluctuations, we allow the fitter to adjust the background on an event-by-event basis. This is done by allowing the fitter to adjust the parameters in the background model, within errors, by adding χ^2 type terms to the function w'_{sr}. Upon adding

5 The notation $d\mathcal{DP}$ represents the differential volume on the Dalitz plot, in this case $dm^2_{KK} dm^2_{K^-\pi^+}$.

6 We use $-2\ln\mathcal{L}$ to make the connection with the usual χ^2 of a multivariant Gaussian *pdf*. $\mathcal{G}(\vec{x}) \propto exp(-\frac{1}{2}\chi^2)$, hence $-2\ln\mathcal{G}(\vec{x}) = \chi^2 + \text{constant}$.

these terms we obtain the actual function w_{sr} we are minimizing.

$$\begin{aligned} w_{sr} &= -2\ln\mathcal{L}_{sr} + \chi^2\ terms \\ &= -2\sum_{sr\ \substack{events\\ i}} \ln\left[\epsilon_i\ \mathcal{F}\frac{\mathcal{A}_{s,i}\mathcal{A}^*_{s,i}}{\mathcal{N}_s} + (1-\mathcal{F})\frac{I_{bg}}{\mathcal{N}_{bg}}\right] \\ &+ \sum_{\lambda,\kappa}(\beta_\lambda - \beta^{(sb)}_\lambda)E^{-1}_{\lambda\kappa}(\beta_\kappa - \beta^{(sb)}_\kappa) + \left[\frac{\mathcal{F}-\mathcal{F}_0}{\sigma_{\mathcal{F}_0}}\right]^2 \end{aligned} \tag{5.11}$$

The sum over the index i is with respect to all the events in the signal region. This function w_{sr} is used for our standard fit, the *background parameterization method*. The parameters $\vec{\beta}^{sb}$ and their error matrix $E_{\lambda\kappa}$ are from the sideband fit. They determine the background lineshape whereas the parameter $\mathcal{F}$ the background normalization. The fitter minimizes w_{sr} to obtain the optimal values for $a_j, \delta_j, \mathcal{F},$ and β_j.

In the early stages of our work we used an alternative method (which we eventually abandoned) called the *likelihood subtraction method* It has the advantage of addressing the background in a model-free manner. In this method we form a log-likelihood sum over the signal region events and subtract a log-likelihood sum over the sideband events while adding a χ^2 term to allow the fitter to determine the background normalization. Specifically, we write

$$\begin{aligned} w_{alt} &= -2\ln\mathcal{L}_{sr} + 2\mathcal{Q}\ln\mathcal{L}_{sb} + \chi^2\ terms \\ &= -2\sum_{sr\ \substack{events\\ i}} \ln\left[\epsilon\times\frac{\mathcal{A}_{s,i}\mathcal{A}^*_{s,i}}{\mathcal{N}_s}\right] \\ &+ 2\mathcal{Q}\sum_{sb\ \substack{events\\ j}} \ln\left[\epsilon\times\frac{\mathcal{A}_{s,j}\mathcal{A}^*_{s,j}}{\mathcal{N}_s}\right] + \left[\frac{\mathcal{F}-\mathcal{F}_0}{\sigma_{\mathcal{F}_0}}\right]^2 \end{aligned} \tag{5.12}$$

With this method, the fitter minimizes w_{alt} to obtain the amplitudes $a_i, \delta_i,$ and $\mathcal{F}$. Note that the same probability density function that describes the signal events, pdf_s of equation 5.5, is here used to also represent the background events. The

$\mathcal{Q}$ factor is the strength of the background. It is a function of $\mathcal{F}$ as follows:

$$\mathcal{Q} = \frac{1 - \mathcal{F}}{1 - \mathcal{F}_0}$$

The problem with this method is it is very sensitive to nodes (or approximate nodes) in the intensity function $\mathcal{A}\mathcal{A}^*$ where the logarithm is undefined. These regions are weighed very heavily in the fit and cause it to fail. [31]

5.2.1 Background Parameterization

The background in our final sample is due to both charm and non-charm sources. Our purpose in the present section is to find a suitable model for the background that remains after the analysis cuts described in Section 5.1. We fit the sideband data to the product of cubic polynomials in x ($= m^2_{K^+K^-}$) and y ($= m^2_{K^-\pi^+}$) as follows:

$$\begin{aligned} I_{bg} = 1 &+ \beta_1 x + \beta_2 y + \beta_3 x^2 + \beta_4 y^2 + \beta_5 2xy \\ &+ \beta_6 x^3 + \beta_7 y^3 + \beta_8 3x^2 y + \beta_9 3xy^2 \end{aligned} \tag{5.13}$$

Starting with this unnormalized background intensity function I_{bg} we form the normalized pdf_{bg} with the usual prescription:

$$pdf_{bg} = \frac{I_{bg}}{\mathcal{N}_{bg}} \tag{5.14}$$

where

$$\mathcal{N}_{bg} = \int\limits_{\substack{sideband \\ limits}} I_{bg} d\mathcal{D}\mathcal{P} \tag{5.15}$$

We perform a joint fit to both the low and high sideband data for the coefficients β_i by again forming a continuous likelihood function. So in the normalization

above, Eq. 5.15, the region of the integration is determined by the Dalitz boundary calculated according to the central mass of the respective sideband. The sideband likelihood function becomes

$$\mathcal{L}_{sb} = \prod_{\substack{sideband \\ events\ j}} pdf_{bg,j}$$

Again, our method is to minimize $-2\ln\mathcal{L}_{sb}$. The results of this procedure are listed in Table 5.5 and displayed in Figs. 5.5 and 5.6.

It is interesting that in our actual Dalitz fit for the amplitude, where we minimize w_{sr} in Eq. 5.11, we use the same same intensity function I_{bg}. So in the actual amplitude fit the background normalization integral 5.15 is calculated over the Dalitz boundary calculated with respect to the central $KK\pi$ mass of the signal region.

Table 5.5 Sideband Fit Results

Parameter	D^+	D_s^+
β_1	$-0.211 \pm .0806$	0.525 ± 1.1872
β_2	$-0.884 \pm .0471$	$5.409 \pm .8727$
β_3	$0.012 \pm .0619$	$1.824 \pm .8349$
β_4	$0.246 \pm .0331$	$-3.451 \pm .5806$
β_5	$0.042 \pm .0278$	$-2.648 \pm .4606$
β_6	$0.070 \pm .0237$	$-0.376 \pm .2181$
β_7	$-0.019 \pm .0077$	$0.575 \pm .1105$
β_8	$0.017 \pm .0064$	$0.519 \pm .0799$
β_9	$-0.038 \pm .0104$	$0.057 \pm .1016$

In the figure we plot the Dalitz scatterplots of the sidebands and the mass-squared projections $m^2_{K^+K^-}, m^2_{K^-\pi^+}, m^2_{K^+\pi^+}$ in data (points) and as predicted by the fit

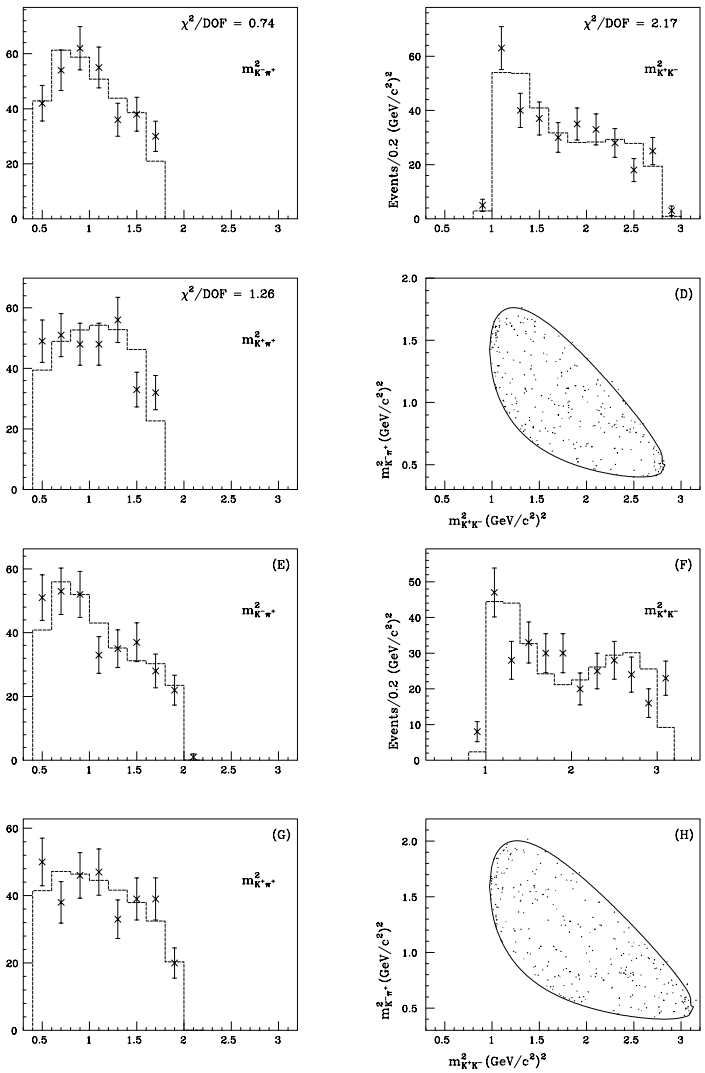

Figure 5.5 D^+ sideband Dalitz plot fit. A) - D) are the low sideband representations; E) - H) the high sideband. In the histograms, the points with error bars are the data, the histogram the prediction of the polynomial model. In the Dalitz scatterplots, the Dalitz boundary is drawn with respect to the center of the respective sideband.

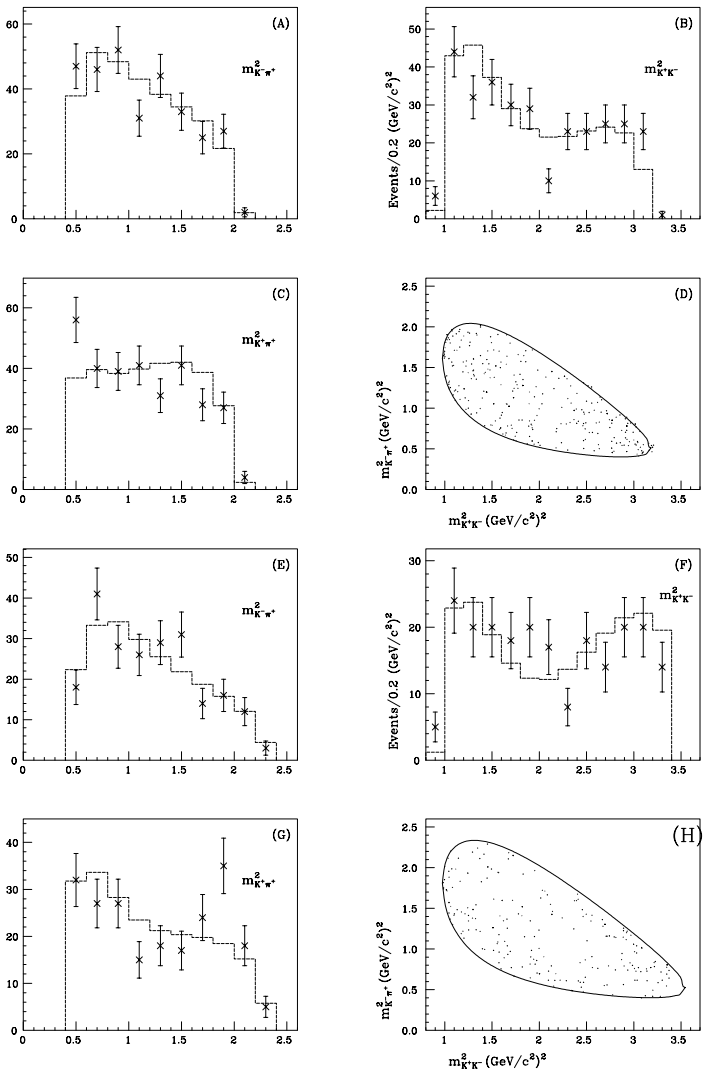

Figure 5.6 D_s^+ sideband Dalitz plot fit. A) - D) are the low sideband representations; E) - H) the high sideband. In the histograms, the points with error bars are the data, the histogram the prediction of the polynomial model. In the Dalitz scatterplots, the Dalitz boundary is drawn with respect to the center of the respective sideband.

results (solid histogram). Roughly speaking, the distribution of events in the sidebands is uniform.

As one indication of the quality of the fit we calculate the *likelihood confidence level* for the function which we minimize, $-2\ln\mathcal{L}_{sb}$, according to the method developed by the ARGUS Collaboration [16] and described in Section 5.5. In Table 5.6 we report the likelihood confidence levels for the various sidebands.

Table 5.6 Sideband Fit Quality Assesment

Region	$-2\log\mathcal{L}_{sb}^{fit}$	$\langle -2\log\mathcal{L}_{sb}^{fit}\rangle$	$\mathcal{L}CLVL(\%)$
D^+ LSB	162.7	167.2 ± 12.56	63.9
D^+ HSB	348.3	344.1 ± 15.14	39.0
D_s^+ LSB	363.9	378.4 ± 13.63	85.6
D_s^+ HSB	403.2	377.0 ± 15.32	4.4

5.2.2 Efficiency Correction Function

Equation 5.7 contains the function $\epsilon(m^2_{KK}, m^2_{K^-\pi^+})$ which corrects for the imperfect geometrical acceptance and reconstruction efficiency. In general one models the acceptance by first generating a high statistics Monte Carlo sample of particle four-vectors, propagating them through a simulation of the spectrometer and running this output tape through the analysis software. The efficiency is the ratio of reconstructed events to generated events. Departures from unity are indications of imperfections in our equipment and/or methods.

Before we describe our procedure for parameterizing this function, it is important that we address the question 'how many Monte Carlo events should be generated in order that finite Monte Carlo statistics is a negligible source of errors?' To answer this question, it is useful to consider partitioning the Dalitz scatterplot into rectangular regions. We will show that in a given two-dimensional Dalitz bin the error on the efficiency corrected yield is proportional to $\sqrt{1+\frac{N_{data}}{N_{MC}^{acc}}}$.

As a result, once $N_{MC}^{acc} >> N_{data}$ for each bin, uncertainty due to finite Monte Carlo statistics becomes negligible.

We presently employ Poisson and binomial statistics to demonstrate how one obtains a minimum variance estimate of the efficiency corrected yield $Y_{corr} = \frac{N_{data}}{\epsilon_{MC}}$. The fractional error on the efficiency corrected yield is

$$\frac{\sigma(Y_{corr})}{Y_{corr}} = \frac{\sigma_{data}^2}{N_{data}^2} + \frac{\sigma_{\epsilon_{MC}}^2}{\epsilon_{MC}^2} \tag{5.16}$$

N_{data} obeys counting (*i.e.* Poisson) statistics, so

$$\frac{\sigma_{data}^2}{N_{data}^2} = \frac{1}{N_{data}}.$$

The Monte Carlo efficiency function ϵ_{MC} follows binomial statistics. Therefore,

$$\sigma_{\epsilon_{MC}}^2 = \frac{\epsilon}{N_{MC}} \times (1 - \epsilon)$$

which obtains for $\frac{\sigma_{\epsilon_{MC}}^2}{\epsilon_{MC}^2}$

$$\frac{\sigma_{\epsilon_{MC}}^2}{\epsilon_{MC}^2} = \frac{(1-\epsilon)}{\epsilon N_{MC}}$$

If we assume $\epsilon << 1$ and define the product $N_{gen} \times \epsilon_{MC}$ as the number of accepted Monte Carlo events, N_{MC}^{acc} we obtain

$$\sigma^2(Y_{corr}) = \frac{1}{N_{data}} + \frac{1}{N_{MC}^{acc}}$$

Solving for the statistical error in the corrected yield obtains

$$\begin{aligned} \sigma(Y_{corr}) &= \sqrt{\frac{1}{N_{data}} + \frac{1}{N_{MC}^{acc}}} \\ &= \sqrt{\frac{1}{N_{data}}}\sqrt{1 + \frac{N_{data}}{N_{MC}^{acc}}} \\ &= \sigma_{\infty}\sqrt{1 + \frac{N_{data}}{N_{MC}^{acc}}} \end{aligned} \tag{5.17}$$

So, as we approach an infinite number of accepted Monte Carlo events, $\frac{N_{data}}{N_{MC}^{acc}} \to 0$,

and hence we arrive at the best fractional uncertainty in the corrected yield.

In fact, there is a slight subtlety in describing the importance of Eq. 5.17. Our goal of generating enough Monte Carlo events to obtain $N_{MC}^{acc} >> N_{data}$ must be weighed against our need to get a good result within a reasonable amount of simulation CPU time. For a given amount of simulation CPU time, the best strategy is therefore to arrange $N_{MC}^{acc} >> N_{data}$ in each bin by generating the Monte Carlo data with an intensity distribution very close to that in the data. To the extent that I_{data} is different from I_{MC}, one is wasting CPU time by running the Monte Carlo longer in order to populate bins where $N_{MC}^{acc} < N_{data}$ while generating extra events in bins where $N_{MC}^{acc} >> N_{data}$ already, which does not reduce errors in those bins. The basic point of Eq. 5.17 is not that the error gets better as N_{MC}^{acc} increases, but that diminishing returns set in once $N_{MC}^{acc} >> N_{data}$. Eq. 5.17 tells you when to stop!!![7]

The special problem to be addressed for the $KK\pi$ data is that most of the data occurs in the narrow ϕ and $\overline{K}^*(892)^0$ bands. In order to insure $\frac{n_{data}}{n_{MC}} \rightarrow 0$ everywhere on the Monte Carlo sample, we must generate it with an amplitude which approximates the true amplitude in the data. Our efficiency modeling procedure is illustrated in Fig. 5.7 and is described below.

First we get a crude decay amplitude by fitting the final analysis sample with the pdf_s in equation 5.5 and the efficiency function ϵ fixed to unity. This step obtains the fit parameters $\vec{\alpha}_{uncorrected}$. We then use the resulting $pdf_{uncorrected}$ to reject events generated by a phase space Monte Carlo. By rejecting on $pdf_{uncorrected}$ one creates a sample whose Dalitz distribution approximates that of the data. Now propagate these four-vectors through the spectrometer simulation ($ROGUE$) and run this sample through our data reconstruction and filtering software. The resulting Monte Carlo generated D_s^+ Dalitz plot is shown in Fig. 5.8.

---

7 To the extent that the simulated intensity matches the data intensity one can simply use Eq. 5.17 to inflate the error bars due to finite Monte Carlo statistics, where N_{data} and N_{MC}^{acc} refer to the total number of events in the plot rather than the number in a given bin.

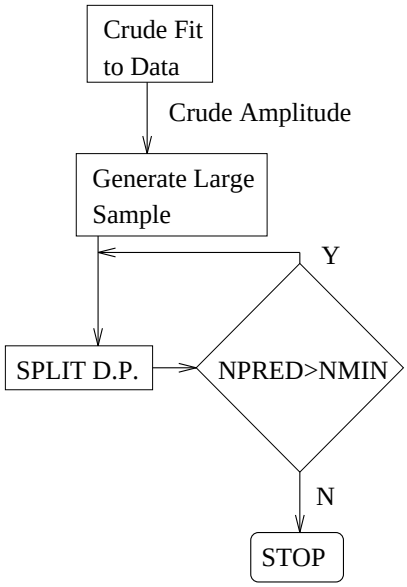

Figure 5.7 Flowchart for the parameterization of the efficiency function ϵ.

The next issue is how to choose the bins. We use the adaptive binning strategy (described in the next section). It allows us to place the binning over the smallest bin sizes commeasurate with our statistics by binning until the number of events in a bin falls below a minimum. Within each bin i calculate the efficiency according to

$$\epsilon_i = \frac{n^i_{reconstructed\ events}}{n^i_{predicted}} \tag{5.18}$$

As always, the predicted number of events in the bin ,$n_{predict}$, is

$$n^i_{predicted} = N_{MC,\ total} \int\limits_{\substack{bin\ i \\ limits}} pdf_{uncorrected} d\mathcal{DP}$$

Here, $N_{MC,\ total}$ is the total number of Monte Carlo signal region events which pass our cuts. The efficiency factors obtained from this adaptive binning scheme are displayed in Figure 5.9. From this figure we calculate the following RMS spread in efficiency across the Dalitz plots:

Table 5.7 RMS Variation of Relative Efficiencies

Parent Particle	RMS Variation
D^+	12.76%
D_s^+	25.59%

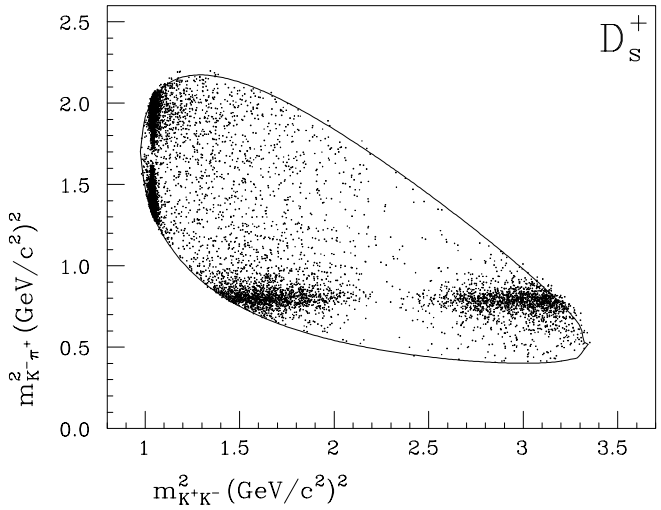

Figure 5.8 Monte Carlo generated Dalitz scatterplot used for the parameterization of the efficiency function ϵ (D_s^+ fit). The D^+ Monte Carlo sample is similar.

5.2.3 The Adaptive Binning Algorithm

The algorithm[8] begins by considering a single bin containing all events and having $(x, y) = (m^2_{K^+K^-}, m^2_{K^-\pi^+})$ corner coordinates defined by kinematic boundary limits. This is the starting point for bin splitting, and we consider splitting into two new bins. A bin can be split so long as the predicted number of events for the bin exceeds a certain value, in this case 25[9] . Ultimately each bin used in the χ^2 is required to contain at least 10 events. We maintain the lower

8 This section borrows material from Ref. [34].

9 For the high statistics Monte Carlo we use for the efficiency samples, this value is increased to 50.

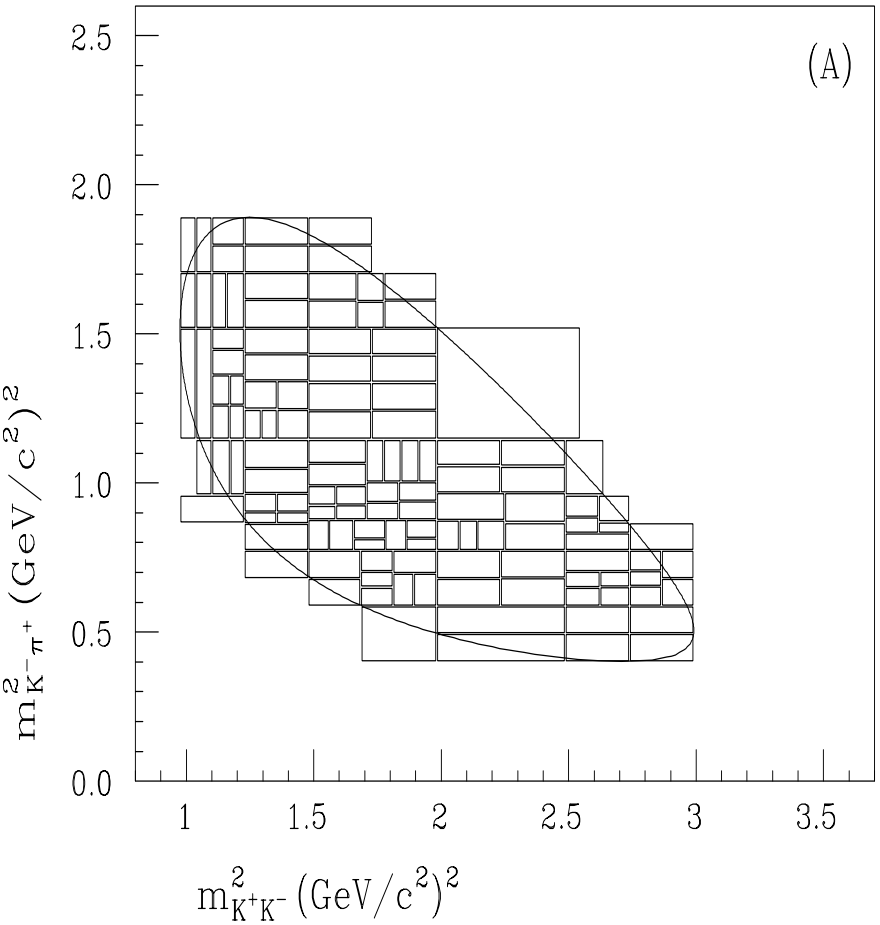

Figure 5.9a Bins resulting from running the adaptive binning algorithm on the high statistics $D^+ \to K^+K^-\pi^+$ Monte Carlo sample. Within each bin i we calculate the efficiency according to $\epsilon_i = \frac{n^i_{reconstructed\ events}}{n^i_{predicted}}$. We emphasis the binning by suppressing the resulting bin-by-bin efficiency factors from the figure.

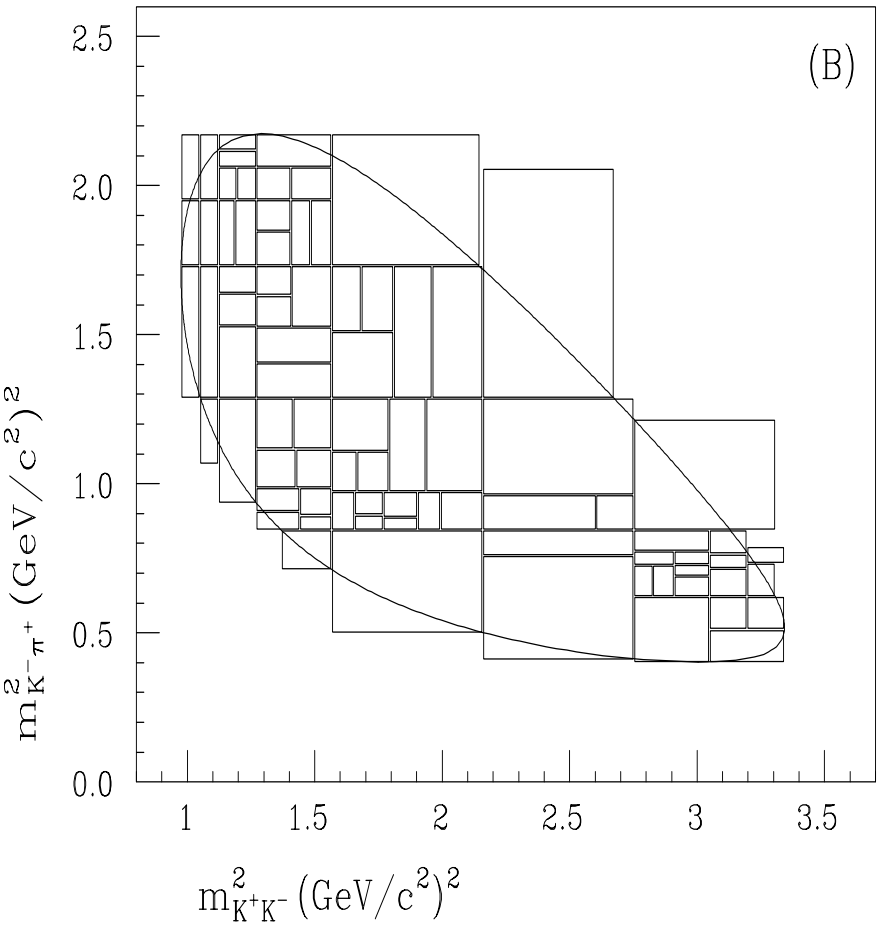

Figure 5.9b Bins resulting from running the adaptive binning algorithm on the high statistics $D_s^+ \to K^+K^-\pi^+$ Monte Carlo sample (Fig. 5.8). Note there are more bins in Fig. 5.9a. This difference in binning is a consequence of the dominance of the ϕ and $K^*(892)^0$ bands on the D_s^+ Dalitz plot. This Dalitz plot requires large bins to get sufficient statistics in regions outside these bands. There is a much larger fraction of D^+ events outside of the two landmark bands and hence one can use more bins in the 'out of band' region. As in Fig. 5.9a, we emphasis the binning by suppressing the resulting bin-by-bin efficiency factors from the figure.

limit so that the χ^2 for the bin,

$$\chi^2 = \frac{(N_{pred} - N_{obs})^2}{N_{pred}} \tag{5.19}$$

is computed reliably, *i.e.* the statistics falls within the distribution described by the Gaussian function. Although this statistic, the so-called *two-dimensional* χ^2, does not come into play in the efficiency correction parameterization, it will be used later (Sec. 5.5) to characterize the quality of our Dalitz amplitude fit results.

To decide how to split the bin, we look at the average derivative in x, y across the bin. We split the bin in the direction of most rapid change, at the location of the centroid (i.e. the average value of the coordinate weighted by the intensity). It is desirable to avoid bin comparisons using bins with very large height-width aspect ratio. To keep the aspect ratio from becoming too large, we split the longitudinal coordinate if the bin is longer than wide by a factor of 1.5, and visa versa. This value was arrived at simply by trial and experience. Sometimes bins are created having an aspect ratio larger than 1.5 since the decision is made on a proposed bin and not on the two created. Bins which have some portion of their area outside the kinematic boundary are split differently depending on the size of the data sample. For large statistics samples, bins which have more than 10% of their area outside the kinematic boundary are simply split in two. In this case we want to split the bin so as to create two bins, one which is highly overlapping with the kinematically allowed phase space, and the other which is mostly outside limits. Thus if two corners are outside of the boundary, we split in the direction parallel to the line joining them. Otherwise, the rules above are followed.

For smaller statistics samples, we make two "passes": in the first we split in the usual way and ignore bins which are outside limits. On the second pass we split the outer bins by successively shaving 1% off the edge determined as above (by considering corners or direction of rapid change, etc.). This was found

to work better for sparsely populated areas of the Dalitz plot which otherwise, using this algorithm, would be missed in the bin comparison.

5.2.4 Resolution Effects

So far we have addressed distortion of the signal probability density function due to background contamination and detection efficiency. A final agent of corruption is the experimental uncertainty of our measurements. For example, an event having a true value of m^2_{KK} will yield a measured value m'^2_{KK}. The probability density function for this process is the resolution function $r(m^2_{KK}, m^2_{K\pi})$. So the total true density function (signal + background) is pdf_{true} whereas the measured density is

$$pdf_{meas}(m^2_{KK'}, m^2_{K\pi'}) = \int_{\mathcal{DP}} r(m^2_{KK}, m^2_{K\pi}; m^2_{KK'}, m^2_{K\pi'}) \times pdf_{true}(m^2_{KK}, m^2_{K\pi}) dm^2_{KK} dm^2_{K\pi} \tag{5.20}$$

Note that measurement resolution is fundamentally different from detection efficiency because now the "true" variables m^2_{KK} and $m^2_{K\pi}$ have been integrated out and replaced with the measured variables m'^2_{KK} and $m'^2_{K\pi}$. Resolution can give rise to a measured value at a location where the true density is zero. On the other hand, the efficiency function $\epsilon(m^2_{KK}, m^2_{K\pi})$ is the density for observing an event at $(m^2_{KK}, m^2_{K\pi})$. It modulates the underlying actual density to obtain a distorted observed density.

It is traditional to take $r(m^2_{KK}, m^2_{K\pi})$ to be a Gaussian function

$$r(m^2_{KK}, m^2_{K\pi}) = \frac{1}{\sigma\sqrt{2\pi}} \exp\left[\frac{(m'^2_{KK} - m^2_{KK})^2}{2\sigma^2}\right]$$

The Monte Carlo resolution widths σ for m^2_{KK} and $m^2_{K\pi}$ in the ϕ and $\overline{K}^*(892)^0$ regions, respectively, are listed in the following table and shown in Figure 5.10.

Table 5.8 Monte Carlo Resolution

	D^+	D_s
σ_{KK} (MeV)	$1.47 \pm .009$	$1.53 \pm .0118$
$\sigma_{K^-\pi^+}$ (MeV)	$3.83 \pm .0255$	$4.45 \pm .0703$

These numbers are to be compared to the $\overline{K}^*(892)^0$ and ϕ resonance widths: 50.5 and 4.43 MeV, respectively. [28] Hence it is appropriate to focus only on the KK measurement uncertainty.

Recall that to obtain $\epsilon(m^2_{KK}, m^2_{K\pi})$ we fit a Monte Carlo sample that includes the detector simulation. Hence it reflects the experimental resolution because the kinematic variables (i.e., $m^2_{KK}, m^2_{K\pi}$) suffer from measurement resolution. Therefore, we do not have to explicitly fold resolution into our calculations. We test this simplification by generating a sample according to a preliminary amplitude, running it through the spectrometer simulation and finally fitting this sample with our Dalitz analysis software. As shown in the table, the fit results agree with the generation level parameters within errors, thereby proving we can safely neglect explicit resolution according to equation 5.20.

Table 5.9 Resolution Test Results

	D^+		D_s^+	
Parameter	Generation	Fitted	Generation	Fitted
f_{K^*}	0.278 ± 0.022	0.276 ± 0.023	0.380 ± 0.023	0.374 ± 0.020
f_ϕ	0.368 ± 0.021	0.366 ± 0.021	0.564 ± 0.026	0.586 ± 0.021
f_{NR}	0.392 ± 0.026	0.390 ± 0.023	0.111 ± 0.025	0.095 ± 0.016
δ_{K^*} (fixed)	0.0^o	0.0^o	0.0^o	0.0^o
δ_ϕ	162.5 ± 9.3^o	174.232 ± 8.2^o	147.4 ± 13.0^o	143.2 ± 10.0^o
δ_{NR}	95.7 ± 6.1^o	94.7 ± 5.8^o	173.9 ± 13.0^o	175.5 ± 9.3^o

An interesting consequence of resolution smearing is the reconstruction of

events outside the nominal Dalitz boundary, which is drawn (in Fig. 5.2) with respect to the world average [28] D^+ or D_s^+ meson mass. We include these events in the minimization of w_{sr} in Eq. 5.11 as well. This presents no technical problems because the likelihood function is in fact analytic outside this boundary. By averaging in these events which smear past the boundary, one obtains a truer estimate of unresolved intensity.

5.2.5 **The Anti-Reflection Cut**

The cut on the $D^+ \to K^-\pi^+\pi^+$ reflection is essentially a filter on the 3-momentum of the kaon with the same electric charge as the pion (i.e., $D_s^+ \to \underline{K^+}K^-\pi^+$ and $D^+ \to \underline{\pi^+}K^-\pi^+$). [14,35] One obtains this result by writing $m^2_{abc} = (p_a^\mu + p_b^\mu + p_c^\mu)^2$ and taking the limit of $|\vec{p}_i| \gg m_i$ and $\theta_{ij} \simeq 0$. Expanding and simplifying gives equation 5.21 below:

$$m^2_{K^+K^-\pi^+} = m^2_{\pi^+K^-\pi^+} + \frac{m^2_{K^+} - m^2_{\pi^+}}{x} \tag{5.21}$$

x is the (laboratory) 3-momentum fraction of the same sign kaon. In this section we describe a study of the correlation between this cut and the Dalitz plot mass-squared variables.

Upon performing a Lorentz transformation along the z-axis to the rest frame of the D_s^+ (denoted by "*") obtains

$$\begin{aligned} E^{lab}_{K^+} &= \gamma^*[E^*_{K^+} + \beta^* P^*_{Z,K^+}] \\ &= \frac{E^{lab}_{D_s}}{M_{D_s}}[E^*_{K^+} + P^*_{K^+}U^*] \end{aligned}$$

Here, $\beta^* \simeq 1$ and $U^* \equiv \cos\theta^*(D_s^+, K^+)$. With $P^{lab}_{D_s} \simeq E^{lab}_{D_s}$ we have

$$x^{lab} = \frac{1}{M_{D_s}}[E^*_{K^+} + P^*_{K^+}U^*]$$

Since $E^*_{K^+}$ and $P^*_{K^+}$ are functions of the Dalitz plot variables, for a given $(M^2_{K^-K^+}, M^2_{K^+\pi^-})$ the only independent variable in this equation is U^*. According to the equation 1, the reflection cut ($1.850 < m_{\pi^+K^-\pi^+} < 1.887$) defines

a rejection region, $x_1 < x < x_2$ on the $(U^*, x^{lab}_{K^+})$ plane. An example plot of the $(U^*, x^{lab}_{K^+})$ plane for a particular $(M^2_{K^-K^+}, M^2_{K^+\pi^-})$ is illustrated in Figure 5.11. Regions A_1 and A_3 are the acceptance regions, while region A_2 is the rejection region. Using the trapezoidal areas defined on the figure, we obtain the efficiency of the reflection cut is

$$\epsilon^{refl\ cut}(M^2_{K^-K^+}, M^2_{K^+\pi^-}) = \frac{A_1 + A_3}{A_1 + A_2 + A_3}.$$

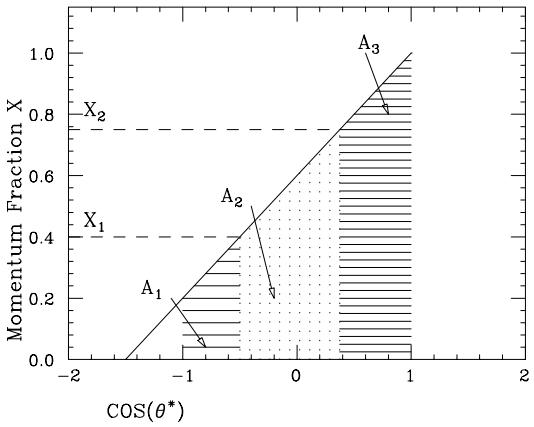

Figure 5.11 Illustration of momentum rejection region in the $(U^*, x^{lab}_{K^+})$ plane. This figure illustrates the mapping between U^* and $x^{lab}_{K^+}$. In our analytic model of the reflection cut (Fig. 5.12) we use the mapping to translate the cut on $x^{lab}_{K^+}$ to a cut on U^*.

We show a 2-dimensional histogram (*Lego-plot*) of this function in Figure 5.12. The overall efficiency of the reflection cut obtained from this plot is 0.828, which is consistent with the efficiency obtained from Monte Carlo, 0.81 ± 0.0196. More importantly, the Lego plot shows that the reflection cut produces only a very gentle modulation in the acceptance across the Dalitz plot. So we find that the reflection cut depends on both the decay's position in the Dalitz plot as well as the D^+ rest frame orientation of the same sign kaon with respect to the D^+_s lab direction. Because the orientation is random, the anti-reflection cut efficiency

has only a relatively mild ($\approx 20\%$) variation across the Dalitz plot and is most strongly tied to $m^2(K^-\pi^+)$. It is therefore quite simple to correct for using our Monte Carlo derived efficiency function $\epsilon(m^2_{KK}, m^2_{K\pi})$, as described in section 5.2.2.

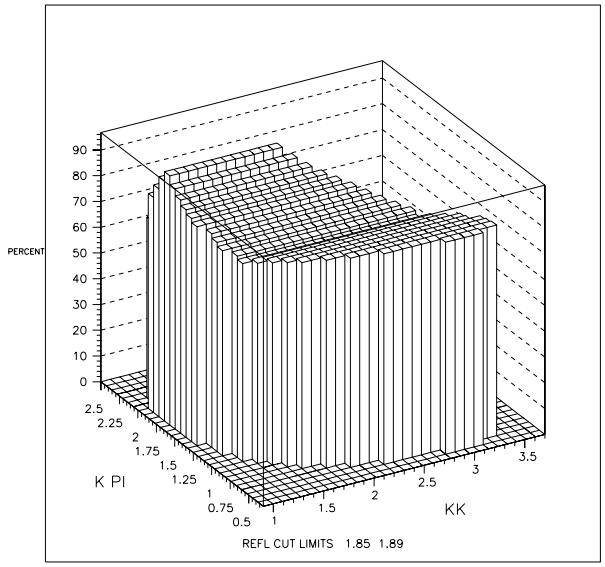

Figure 5.12 Lego plot of reflection cut acceptance.

We close this section by emphasizing that our treatment of the reflection cut implied by Fig. 5.11 is primarily discussed in order to reassure the reader that the anti-reflection cut is easy to model and has a relatively mild effect on the efficiency across the Dalitz plot. We add that the efficiency of the anti-reflection cut is automatically included in the the efficiency tables illustrated in Figure 5.9.

5.3 Fit Results

Recall that our method for fitting the decay amplitudes, Eq. 2.10, is to minimize equation 5.11 with the Minuit [32] software package to obtain the fit amplitudes $\{a_i\}$, fit phases $\{\delta_i\}$, signal fraction $\mathcal{F}$ and background shape parameters $\{\beta_i\}$.[10] Using equation 2.12 we calculate the decay fractions. In this

10 The signal fraction $\mathcal{F}$ and background shape parameters $\{\beta_i\}$ are obtained from separate fits to the $KK\pi$ mass histogram and sideband Dalitz plots, respectively. In the Dalitz

section we motivate our choice of participating decay channels for the D^+ and D_s^+, respectively. In our searches, we employ three tools for identifying which decay channels participate in the amplitude sum Eq. 2.10:

a. Visual comparison of the Dalitz scatterplot of the data[11] to scatterplots obtained from Monte Carlo simulations imcluding only pure resonant (or nonresonant) decay channels. We employ Monte Carlo rejection on the *pdf* of Eq. 5.7 where $\mathcal{A}_s$ includes only one decay channel and $\mathcal{F}$ is fixed to unity.[12] These simulated scatterplots are displayed in Fig. 5.13.

b. Careful study of the mass-squared projections of the data to identify interference phenomena.

c. Our main tool for establishing the statistical significance of an amplitude is the change $\Delta\chi^2$ in the χ^2 calculated from the fitted amplitude in the adaptively chosen two-dimensional bins. That is to say, given two fit hypotheses 1 and 2 and their respective χ^2's, if $\chi_2^2 < \chi_1^2$ the Hypothesis 2 is preferred to Hypothesis 1 at the level of $\sqrt{\chi_2^2 - \chi_1^2} = \sqrt{\Delta\chi^2}$ standard deviations. By hypothesis we mean a particular sum of intermediate decay amplitudes.

Our searches obtain good fits using purely resonant intermediate decay modes without the need for a nonresonant component. We will present evidence for previously undiscovered decay modes [28]. The D^+ fit is covered first and is followed by the D_s^+ results.

5.3.1 Results of the D^+ Fit

As illustrated in the $D^+ \to K^+K^-\pi^+$ Dalitz plot, Fig. 5.14, the most prominent channels in this decay are $\overline{K}^*(892)^0K^+$, $\phi\pi^+$ and at least one additional

---

amplitude fit they are allowed to vary within errors by the mechanism of the added χ^2 terms in Eq. 5.11.

11 We found both the full dataset and airgap Dalitz plots useful in deciding on the appropriate channel mixture.

12 To remove the pdf_bg terms from the simulation.

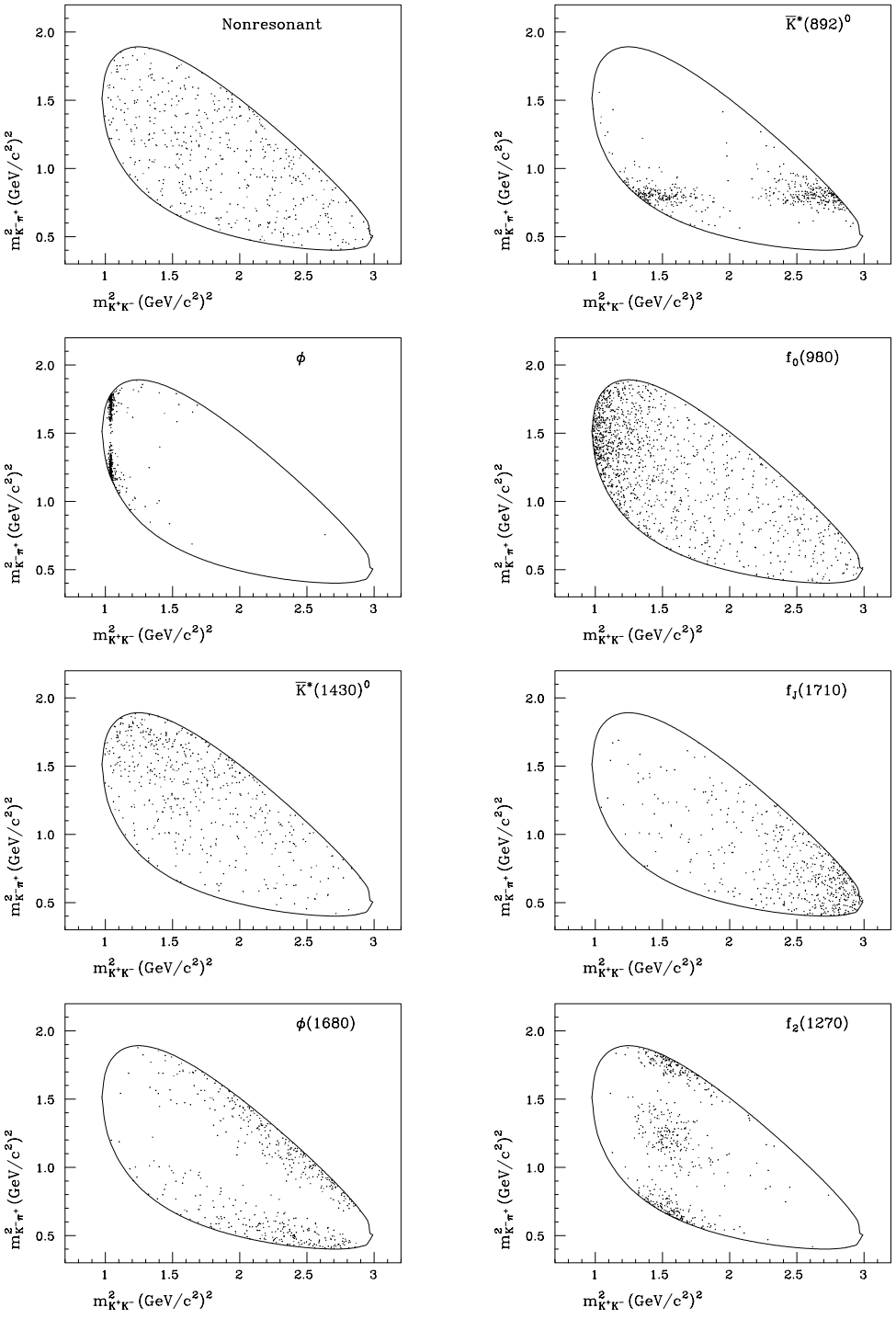

Figure 5.13a D^+ simulated pure resonances.

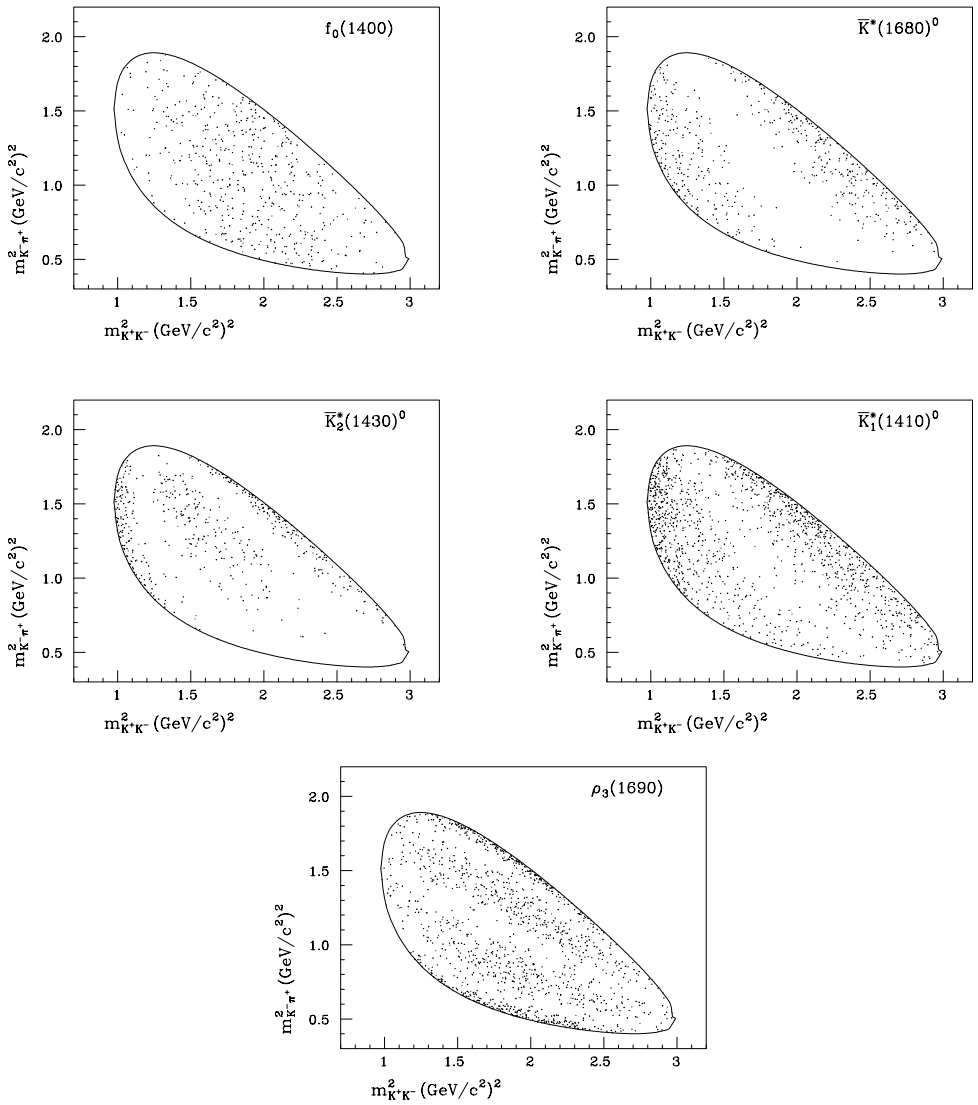

Figure 5.13b D^+ simulated pure resonances.

slowly varying (in the mass-squared variables) resonant or nonresonant contribution. The asymmetry evidenced by the ϕ lobes labeled L_1 and L_2 on the the $M^2_{K^-\pi^+}$ projection, suggests the presence of a high mass $K^-\pi^+$ resonance.[13] Furthermore, the arguments of Sec. 2.2.1 indicate that the asymmetry in the $\overline{K}^*(892)^0$ lobes (L_3 and L_4) may be caused by inteference between the $\overline{K}^*(892)^0$ and a slowly varying amplitude whose fitted phase shift (with respect to the $\overline{K}^*(892)^0 K^+$) is approximately 90^o. Upon examination of our simulated Dalitz

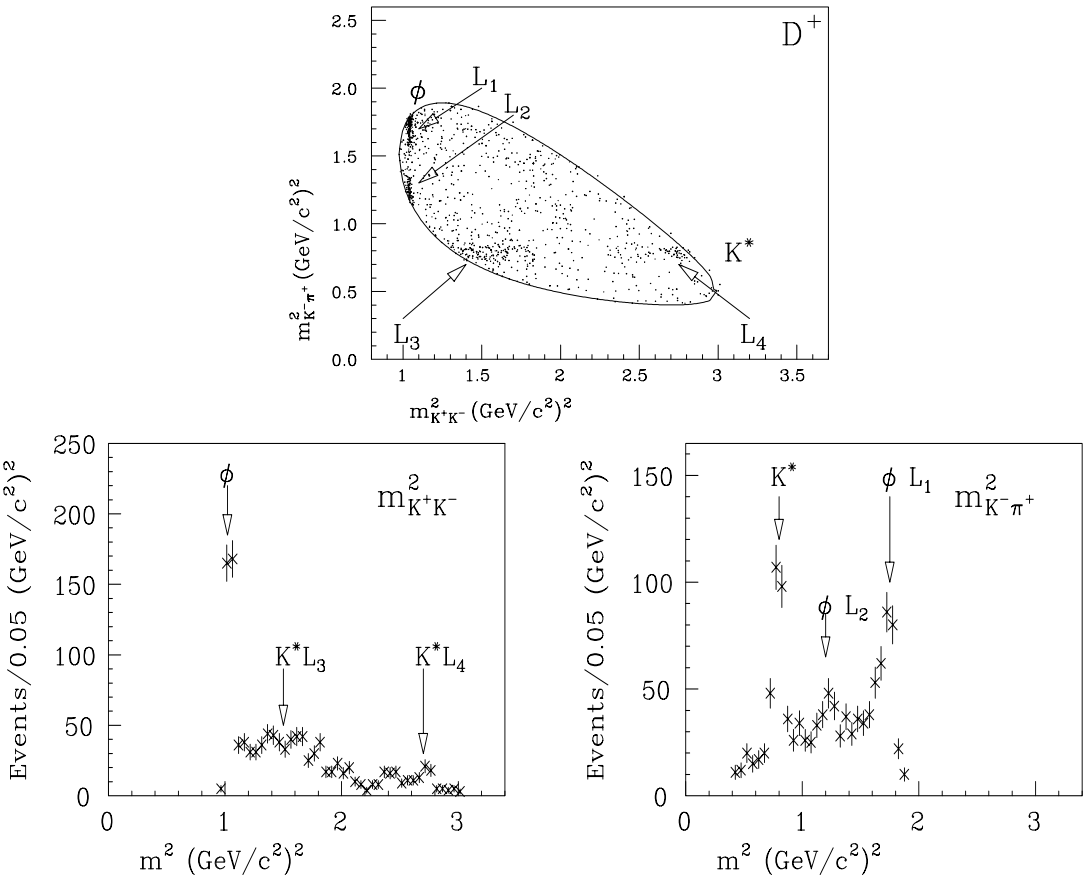

Figure 5.14 D^+ Dalitz scatterplot, m^2_{KK} and $m^2_{K^-\pi^+}$ projections. Examination of these plots motivate inclusion of the $\overline{K}^*_0(1430)^0 K^+$ channel in the amplitude fit.

scatterplots, Fig. 5.13, we identify the $\overline{K}^*_0(1430)^0 K^+$ channel as a likely candidate

13 A pure ϕ would obtain symmeteric L_1 and L_2 lobes.

which provides these resonance structures. It is a wide (i.e., slowly varying) high mass $K^-\pi^+$ resonance with no Zemach nodes. It greatly resembles a nonresonant contribution except it preferentially populates the high $m^2_{K^-\pi^+}$ region of the Dalitz plot. A coherent superposition of the landmark channels $\overline{K}^*(892)^0K^+$ and $\phi\pi^+$, along with the $\overline{K}^*_0(1430)^0K^+$, does a good job of reproducing the lobe

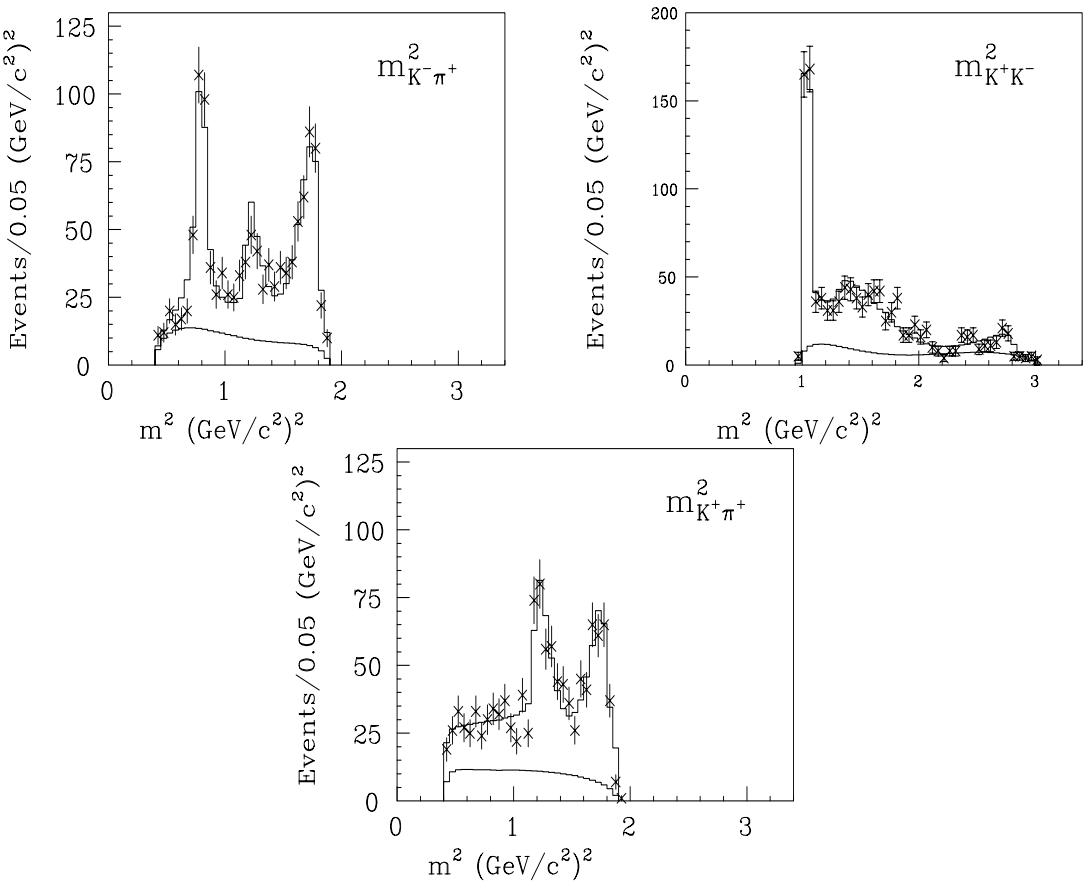

Figure 5.15 Mass-squared projections obtained with the D^+ fit. The points with error bars are the data; the large histogram the prediction pf the fit (signal + background); the small histogram is the prediction of the background model.

asymmetries described above. The final result is compared to the data in Fig. 5.15 and summarized in Table 5.10.[14] Although the mass projections of the fit shown in Fig. 5.15 are a fairly good match to the projection histogram of the

14 This table only shows statistical errors. The final results showing systematic errors will be listed in Table 5.17.

data, the fit has an unacceptably large χ^2 for matching the data in adaptively chosen, two dimensional bins (94.2 for 44 degrees of freedom). This suggests that the model, although fitting the data fairly well in a qualitative sense, may be over simplified.[15] The mass-squared projections obtained with this fit are shown in Fig. 5.15.

We use our adaptive binning software to deduce where the fit matches the data and where it fails to mimic the physical intensity. Figure 5.16 shows the bin-by-bin contribution to the χ^2 in Eq. 5.19.

Table 5.10 D^+ Fit Results

Parameter	Fitted Value $\pm\sigma_{stat}$
$a_{\overline{K}^*(892)^0K+}$	1.0 (fixed)
$a_{\phi\pi^+}$	0.98 ± 0.05
$a_{\overline{K}^*(1430)^0K+}$	1.11 ± 0.07
$\delta_{\overline{K}^*(892)^0K+}$	0^o (fixed)
$\delta_{\phi\pi^+}$	-159 ± 8^o
$\delta_{\overline{K}^*(1430)^0K+}$	70 ± 7^o
$f_{\overline{K}^*(892)^0K+}$	0.301 ± 0.020
$f_{\phi\pi^+}$	0.292 ± 0.031
$f_{\overline{K}^*(1430)^0K+}$	0.370 ± 0.035

To estimate the statistical level this mixture is preferred, we compare the goodness of this fit to others where we include different mixtures of amplitudes. The result of this exercise is shown below in Table 5.11. Note that the fit which is both the simplest and obtains the lowest value of χ^2 is fit # 7, our quoted

15 There may be contributions from slowly varying, nonresonant amplitudes or perhaps the phases δ are functions of the mass-squared Dalitz variables. Of course undiscovered resonances may also be playing a role.

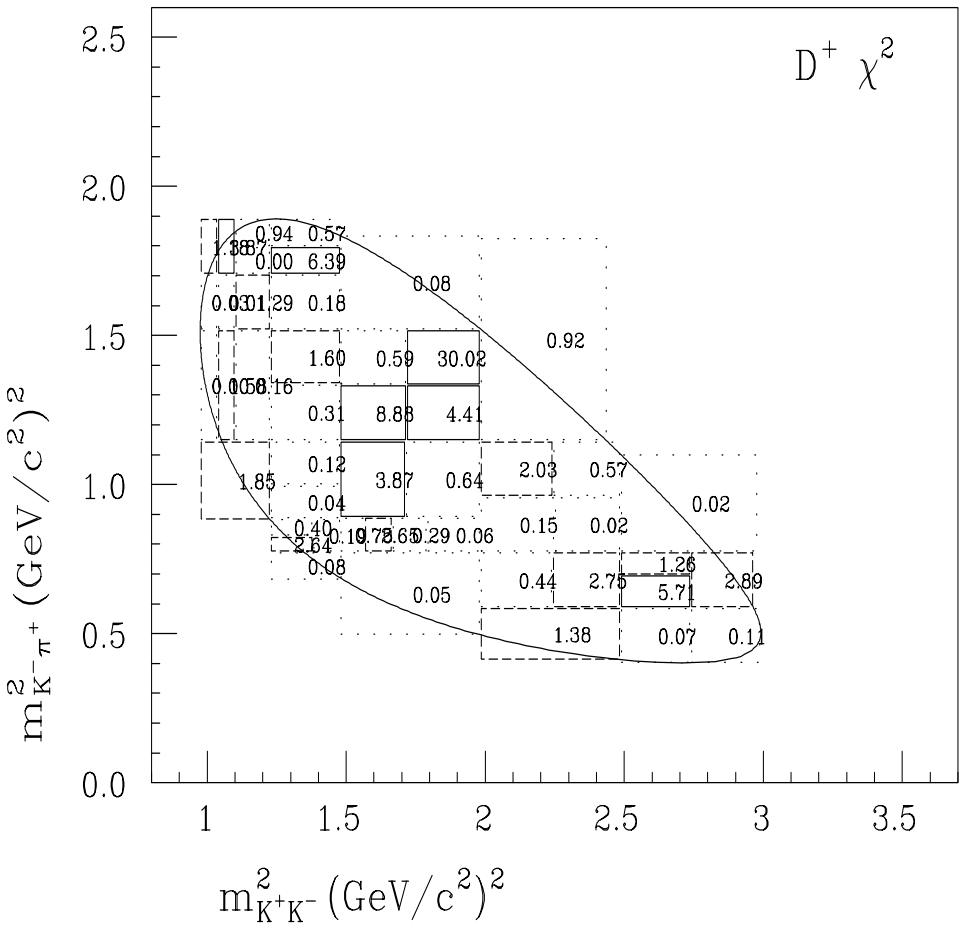

Figure 5.16 Bin-by-bin contribution to the two-dimensional χ^2 for the D^+ fit. The fit obtains a two-dimensional χ^2 of 92.2. A naive count of the degrees of freedom (i.e., $N_{bins} - N_{params}$) obtains 44. As described in Sec. 5.3.2, this calculation underestimates the true number of degrees of freedom. The dotted bins have $\chi^2 < 1.0$, dashed bins have $\chi^2 < 3.0$, solid bins have $\chi^2 > 3.0$

fit.[16] Although its χ^2 value (94.16) is somewhat larger than several more complicated fits, the fitter cannot discriminate between these many-amplitude fits (i.e., they obtain essentially degenerate values of χ^2). Indeed, a sufficiently complicated mixture can certainly mimic the broad, slowly varying structure on the D^+ Dalitz plot. However, our dataset cannot discriminate between these complicated fits and hence does not provide adequate evidence for the presence of channels in addition to $\overline{K}^*(892)^0K^+$, $\phi\pi^+$ and $\overline{K}_0^*(1430)^0K^+$.

5.3.2 Results of the D_s^+ Fit

As Fig. 5.2 shows, the $D_s^+ \to K^+K^-\pi^+$ Dalitz plot is very strongly dominated by the $\overline{K}^*(892)^0K^+$ and $\phi\pi^+$ bands. The Dalitz plot for the very clean "airgap" sample, Fig. 5.2, shows an accumulation of events in the nodal region of the ϕ band. We suspect these events are due to a spinless object (since there is no evidence of Zemach nodes) with broad structure interfering with the ϕ.[17] After studying contributions from known (K^+K^-) and $(K^-\pi^+)$ resonances, we found the decay $D_s^+ \to f_0(980)\pi^+$ is the most likely source responsible for this accumulation. The Dalitz plot for simulated $D_s^+ \to f_0(980)\pi^+$ decays tends to populate the low M^2_{KK} region and hence 'fills in' the ϕ nodal region. The $f_0(980)$ decays via both $\pi^+\pi^-$ and K^+K^-. [28] Because a large fraction of $D_s^+ \to \pi^+\pi^+\pi^-$ decays are known (Ref. [22] and see Chapt. 6) to proceed via $D_s^+ \to f_0(980)\pi^+$, one expects to observe contributions from $D_s^+ \to f_0(980)\pi^+$ to the $K^+K^-\pi^+$ Dalitz plot as well. A fit to the full dataset with a coherent sum of $\overline{K}^*(892)^0K^+$, $\phi\pi^+$ and $f_0(980)\pi^+$ amplitudes obtains $\chi^2 = 80.5$, whereas replacing the $f_0(980)\pi^+$ with three-body nonresonant gets 99.9. This change in χ^2 means the data prefers the $f_0(980)\pi^+$ solution at the $\sqrt{99.9 - 80.5} \simeq 4$ standard deviation level.

---

16 It is interesting to note that replacing the $\overline{K}^{*0}(1430)K^+$ channel with the three-body nonresonant amplitude (Hypothesis 12) obtains an increase of $\sim$ 30 units in χ^2, indicating that the $\overline{K}^{*0}(1430)K^+$ channel is preferred at the $\sim$ 5.5 standard deviation level.

17 Here again we apply the arguments of Sec. 2.2.1 to the observed symmetry of the ϕ lobes in the $M^2_{K^-\pi^+}$ projection points.

Table 5.11a Comparison of D^+ Fits, 3 Amplitudes

χ^2 Rank	Fit Hypothesis	χ^2	$-2ln\mathcal{L}$	$\mathcal{L}$ C.L.
7	$\surd$ $\overline{K}^{*0}(892)$, ϕ, $\overline{K}^{*0}(1430)$	94.16	-723	34.2
12	NR, $\overline{K}^{*0}(892)$, ϕ	124.08	-675	7.8
15	$f_0(980)$, $\overline{K}^{*0}(892)$, ϕ	213.40	-641	0.004
16	$\overline{K}^{*0}(892)$, ϕ, $\overline{K}^{*}(1680)$	242.00	-561	0.0
17	$\overline{K}^{*0}(892)$, ϕ, $\overline{K}^{*}_2(1430)$	242.9	-559	0.0

Table 5.11b Comparison of D^+ Fits, 4 Amplitudes

χ^2 Rank	Fit Hypothesis	χ^2	$-2ln\mathcal{L}$	$\mathcal{L}$ C.L.
4	$\overline{K}^{*0}(892)$, ϕ, $\overline{K}^{*0}(1430)$, $\overline{K}^{*}_2(1430)$	87.24	-737	36.1
5	$NR, \overline{K}^{*0}(892)$, ϕ, $\overline{K}^{*0}(1430)$	88.62	-726	36.3
6	$\overline{K}^{*0}(892)$, ϕ, $\overline{K}^{*0}(1430)$, $\phi(1680)$	91.98	-729	28.4
8	NR, $\overline{K}^{*0}(892)$, ϕ, $f_0(1710)$	95.76	-721	21.8
9	NR, $\overline{K}^{*0}(892)$, ϕ, $\phi(1680)$	100.80	-708	20.5
10	NR, $\overline{K}^{*0}(892)$, ϕ, $\overline{K}^{*}_2(1430)$	108.36	-697	15.2
11	NR, $\overline{K}^{*0}(892)$, ϕ, $f_2(1270)$	113.82	-694	6.1
13	NR, $\overline{K}^{*0}(892)$, ϕ, $\overline{K}^{*}(1410)$	118.86	-691	20.3
14	NR, $\overline{K}^{*0}(892)$, ϕ, $\overline{K}^{*}(1680)$	126.00	-687	22.7

Table 5.11c Comparison of D^+ Fits, $\geq$ 5 Amplitudes

χ^2 Rank	Fit Hypothesis	χ^2	$-2ln\mathcal{L}$	$\mathcal{L}$ C.L.
1	NR, $\overline{K}^{*0}(892)$, ϕ, $\overline{K}^{*0}(1430)$, $\phi(1680)$, $\overline{K}^{*}_2(1430)$	84.42	-741	38.1
2	$\overline{K}^{*0}(892)$, ϕ, $\overline{K}^{*0}(1430)$, $\phi(1680)$, $\overline{K}^{*}_2(1430)$	86.53	-741	33.4
3	NR, $\overline{K}^{*0}(892)$, ϕ, $\overline{K}^{*0}(1430)$, $\overline{K}^{*}_2(1430)$	86.40	-737	31.9

Despite this sizable $\Delta\chi^2$, we tested the statistical significance of this apparent preference for the $f_0(980)\pi^+$ solution as described below.

From our qualitative comments about the airgap sample at the beginning of this section, it is apparent that the low background contamination in this sample enables it to discriminate between the structureless nonresonant and the broad $f_0(980)\pi^+$ channel. Therefore, we designed 'by hand' two-dimensional bins which accentuate the key features of the airgap Dalitz plot: the ϕ and K^* lobes, their Zemach zero regions, and the region far from these resonances. These so-called *static bins* are displayed in Fig. 5.17. The static χ^2 values for fits to the airgap data are listed in Table 5.12. We tested this $\sim 2\sigma$ preference for the $f_0(980)\pi^+$ solution by fitting ensembles of Monte Carlo datasets generated with the amplitudes resulting from our fits to the airgap data.[18] Fig. 5.18 shows the static χ^2 obtained from these fits. This test points out that the preference for the $f_0(980)\pi^+$ is not due to background fluctuation - the amplitude definitely requires a contribution from $f_0(980)\pi^+$.

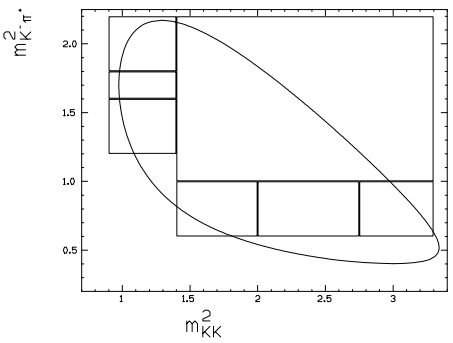

Figure 5.17 Static two-dimensional bins used for discriminating between three-body nonresonant and $f_0(980)\pi^+$ channel.

18 Within each ensemble, each generated sample had the signal region statistics listed in Table 5.4.

Table 5.12, f_0/NR Air Gap Data Fit Comparisons, Static χ^2

	Fit	Hypothesis
	NR, ϕ, K^*	$f_0(WA76), \phi, K^*$
Static $2D$ χ^2	13.4	8.5

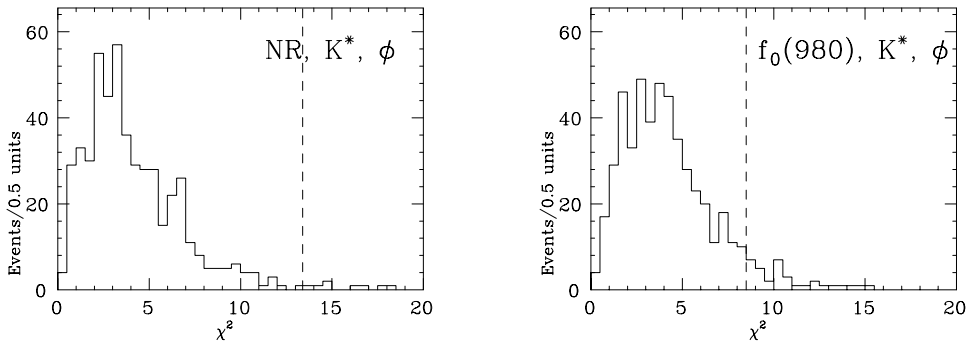

Figure 5.18 Static two-dimensional χ^2 obtained from fitting ensembles of Monte Carlo generated datasets generated with the indicated amplitude The indicated static χ^2 values from Table 5.12 (dashed lines) correspond to 1.6% and 6.8% confidence levels for the $NR, K^*K, \phi\pi$ and $f_0\pi, K^*K, \phi\pi$ fits, respectively.

This Monte Carlo exercise obtained another somewhat surprising result. Naively, the number of degrees of freedom is calculated to be

$$\begin{aligned} NDOF_{naive} &= N_{bins} - N_{params} \\ &= 7\ bins - 4\ fit\ parameters \\ &= 3\ dof \end{aligned} \tag{5.22}$$

In Fig. 5.19 we plot the confidence levels obtained from Fig. 5.18 for the non-resonant and $f_0(980)\pi^+$ fits as functions of the static χ^2. We also show analytic calculations of the confidence level for Gaussian distributed data (the CERNLIB function $PROB(\chi^2, NDOF)$) for different degrees of freedom. Apparently, the correct number of degrees of freedom to use for two-dimensional χ^2 is a complicated function - in this example it falls between 3 and 5. We believe this

phenomenon is a consequence of our parameter estimation procedure, which is to minimize a $-2\ln\mathcal{L}$ function instead of the two-dimensional χ^2.

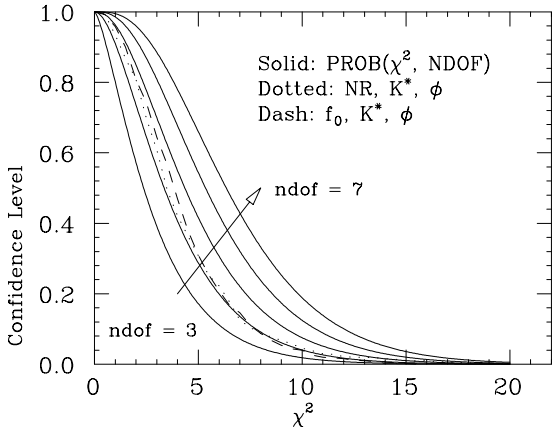

Figure 5.19 Tests of counting degrees of freedom.

Having established the presence of the $f_0(980)\pi^+$ channel in the D_s^+ decay amplitude we now critically examine the fit projections and find there are some notable descrepancies between the fit prediction and the data. The projections (from the fit to the full dataset) are shown in Fig. 5.20. This fit underpredicts of the $\overline{K}^*(892)^0$ peak, R_1 in Fig. 5.20, and overpredicts R_2. We also note the fitted $\overline{K}^*(892)^0$ mass of the two $\overline{K}^*(892)^0$ lobes differ.[19] These observations suggest the presence of additional amplitudes which interfere with the $\overline{K}^*(892)^0$. After studying contributions from established (K^+K^-) and $(K^-\pi^+)$ resonances (see following paragraph), we found the inclusion of a contribution from $f_J(1710)\pi^+$ and $\overline{K}_0^*(1430)^0K^+$ significantly improved the agreement between the fit and data in Regions 1 and 2, as shown in Fig. 5.20.[20] The results of this five amplitude D_s^+ fit, which is our final solution, are summarized in Table 5.13.

---

19 We fit the (background subtracted) low and high $m^2_{K^+K^-}$ $\overline{K}^*(892)^0$ lobes to p-wave Breit Wigners convoluted with the Gaussian function and obtained $888 \pm 5\ MeV/c^2$ and $876 \pm 5\ MeV/c^2$ for the low and high lobes, respectively. The world average [28] $\overline{K}^*(892)^0$ mass is $896 \pm 0.28\ MeV/c^2$.

20 In this fit the $f_J(1710)$ is assumed to be a scalar particle.

Table 5.13 D_s^+ Fit Results

Parameter	Fitted Value $\pm\sigma_{stat}$
$a_{\overline{K}^*(892)^0K+}$	1.0 (fixed)
$a_{\phi\pi^+}$	0.91 ± 0.05
$a_{\overline{K}^*(1430)^0K+}$	0.44 ± 0.08
$a_{f_0(980)\pi^+}$	0.48 ± 0.08
$a_{f_J(1710)\pi^+}$	0.27 ± 0.07
$\delta_{\overline{K}^*(892)^0K+}$	0^o (fixed)
$\delta_{\phi\pi^+}$	178 ± 20^o
$\delta_{\overline{K}^*(1430)^0K+}$	152 ± 40^o
$\delta_{f_0(980)\pi^+}$	159 ± 22^o
$\delta_{f_J(1710)\pi^+}$	110 ± 20^o
$f_{\overline{K}^*(892)^0K+}$	0.478 ± 0.046
$f_{\phi\pi^+}$	0.396 ± 0.033
$f_{\overline{K}^*(1430)^0K+}$	0.093 ± 0.032
$f_{f_0(980)\pi^+}$	0.110 ± 0.035
$f_{f_J(1710)\pi^+}$	0.034 ± 0.023

Inclusion of the $\overline{K}^*(1430)^0K+$ channel in the fit results in a subtle improvement in the fit which is revealed by examing the bin-by-bin contribution to the two-dimensional χ^2. The bin with the maximum value (*hot bin*) obtains a ~ 6 unit decrease in χ^2 after including the $\overline{K}^*(1430)^0K+$ channel, as demonstrated by Fig. 5.21.

As in the D^+ fit we pursue a study where we compare our quoted fit to fits including reasonable mixtures of known decay channels. The results are listed below in Table 5.14.

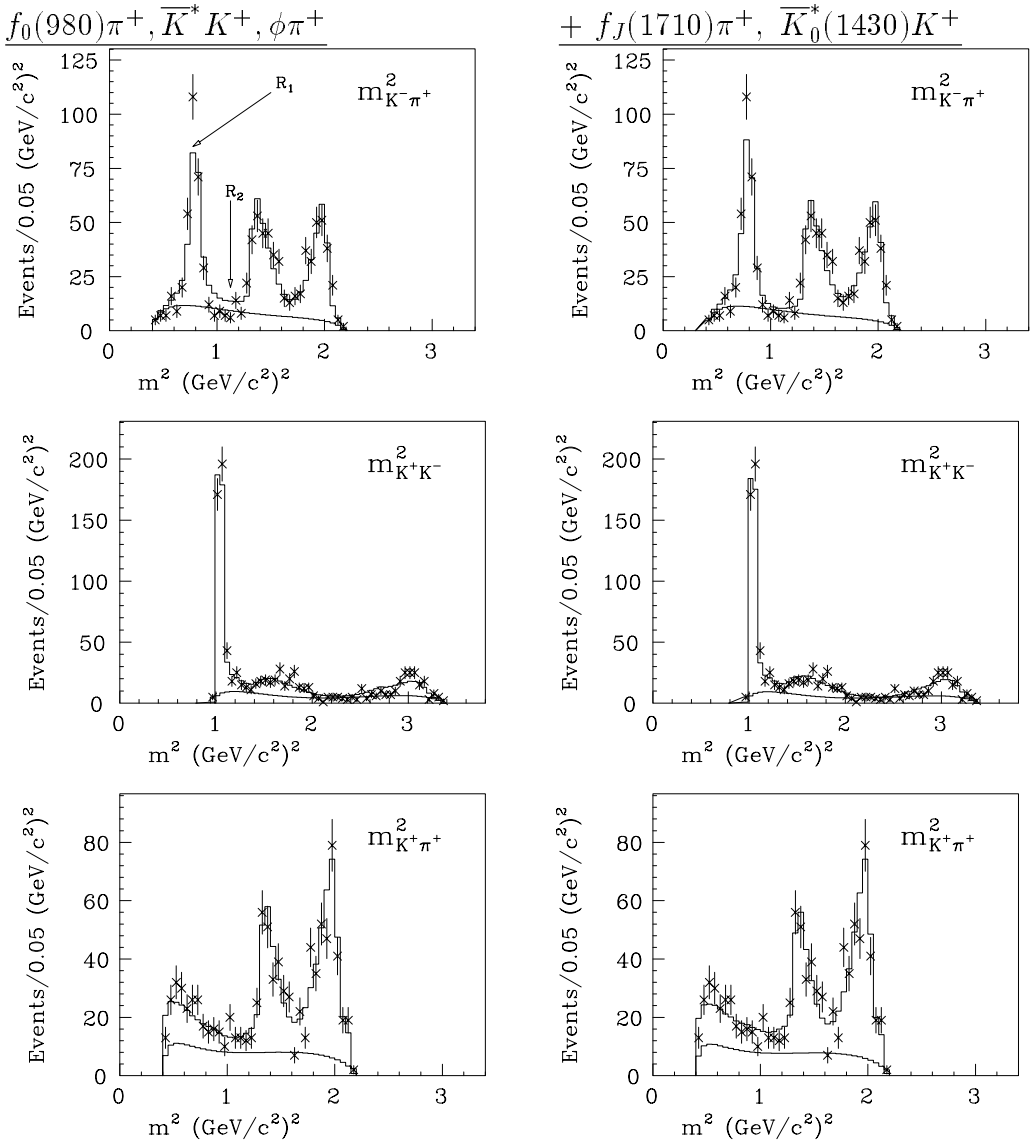

Figure 5.20 Mass-squared projections obtained with the D_s^+ fit. The points with error bars are the data; the large histogram the prediction pf the fit (signal + background); the small histogram is the prediction of the background model. Left column shows result of a fit with the $f_0(980)\pi^+, \overline{K}^* K^+$ and $\phi\pi^+$ amplitudes; right column also includes the $f_J(1710)\pi^+$ and $\overline{K}_0^*(1430)K^+$ channels. The right column projections illustrate our final fit result.

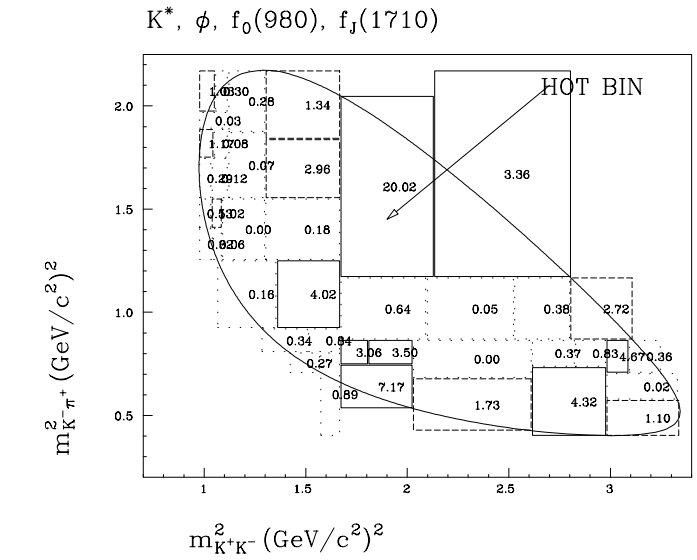

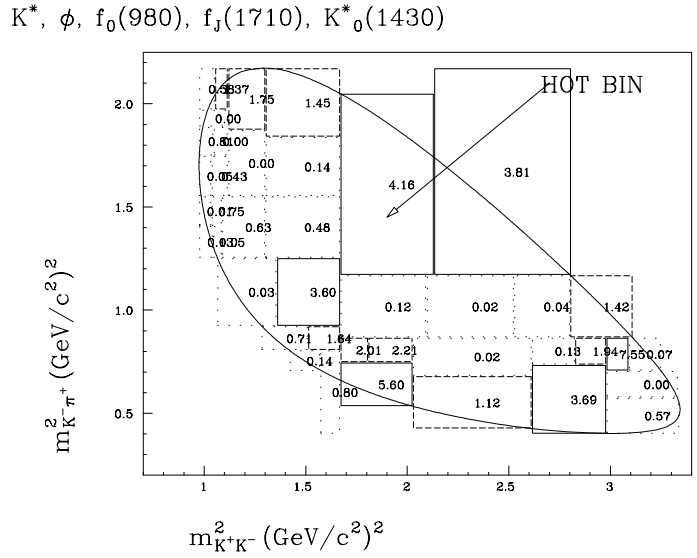

Figure 5.21 Bin-by-bin contribution to the two-dimensional χ^2 for the indicated fit hypotheses for the D_s^+ fit. Our quoted five-amplitude fit obtains a two-dimensional χ^2 of 50.2 with, naively speaking, 33 degrees of freedom.

Table 5.14 Comparison of D_s^+ Fits

#	Fit Hypothesis	χ^2	$-2ln\mathcal{L}$	$\mathcal{L}$ C.L. (%)
1 $\surd$	$\overline{K}^{*0}(892),\ \phi,\ f_0(980),\ f_J(1710),\ \overline{K}^{*0}(1430)$	50.16	-1075	80.2
2	$\overline{K}^{*0}(892),\ \phi,\ f_0(980),\ \overline{K}^{*0}(1430)\ \overline{K}^{*}(1410),\ \overline{K}_2^{*}(1430)$	54.6	-1068	91.1
3	$\overline{K}^{*0}(892),\ \phi,\ f_0(980),\ f_0(1400),\ \overline{K}_1^{*}(1680)$	55.11	-1073	80.7
4	$\overline{K}^{*0}(892),\ \phi,\ f_0(980),\ \overline{K}_1^{*0}(1430)\ \overline{K}^{*}(1410)$	55.77	-1067	91.0
5	$NR,\ \overline{K}^{*0}(892),\ \phi,\ f_0(980)$	56.0	-1068	69.5
6	$\overline{K}^{*0}(892),\ \phi,\ f_0(980),\ \overline{K}^{*0}(1430)$	57.05	-1060	83.8
7	$\overline{K}^{*0}(892),\ \phi,\ f_0(980),\ \overline{K}^{*}(1410)$	66.5	-1048	85.3
8	$\overline{K}^{*0}(892),\ \phi,\ f_0(980),\ f_0(1400)$	66.85	-1055	53.9
9	$\overline{K}^{*0}(892),\ \phi,\ \overline{K}^{*0}(1430),\ \overline{K}^{*}(1410),\ \overline{K}_2^{*}(1430)$	69.6	-1042	61.1
10	$\overline{K}^{*0}(892),\ \phi,\ f_0(980),\ f_J(1710)$	70.7	-1046	36.7
11	$\overline{K}^{*0}(892),\ \phi,\ \overline{K}_1^{*}(1410),\ \overline{K}^{*0}(1430)$	71.05	-1036	57.3
12	$\overline{K}^{*0}(892),\ \phi,\ \overline{K}^{*0}(1430)$	76.96	-1027	52.8
13	$\overline{K}^{*0}(892),\ \phi,\ \overline{K}^{*}(1410)$	79.18	-1020	20.8
14	$\overline{K}^{*0}(892),\ \phi,\ f_0(980),\ f_2(1270)$	80.15	-1023	43.4
15	$\overline{K}^{*0}(892),\ \phi,\ f_0(980)$	81.4	-1018	53.2
16	$\overline{K}^{*0}(892),\ \phi,\ f_0(980),\ \overline{K}_2^{*}(1430)$	81.55	-1020	51.2
17	$\overline{K}^{*0}(892),\ \phi,\ f_0(980),\ \phi(1680)$	83.3	-1020	56.6

5.4 Measurement Error

We believe [17] that it is appropriate to quote two independant types of error on amplitude measurements.[21] The first error is the usual statistical error which we obtain from the fitter itself, after checking that it is a fair representation of the variation of parameters using an ensemble Monte Carlo technique (*Mini Monte*

21 This section is borrowed from Ref. [33].

Carlo) to be described shortly. The second error is a systematic error which (as we discuss below) is estimated by considering differences in the fit parameters obtained with different fitting techniques, and non-statistical differences in the parameters obtained by fitting disjoint (i.e. essentially uncorrelated) sub-samples of the data. A third error due to the lack of knowledge [28] about some of the resonance parameters themselves was found to be totally negligible[22] and is not included in our error estimates.

5.4.1 Monte Carlo Tests of Fit Biases and Errors

We checked the fidelity of parameter errors and the presence of biases in the parameters returned by the fit using expedited Monte Carlo simulations (so called *Mini Monte Carlo*). An expedited simulation prodeeds by generating three body decays according to the final fitted amplitude (our *parent distribution*), simultaneously correcting for acceptance variation by using the parameterized acceptance which was originally based on the full, hit level simulation (see section 5.2.2). We also simulate accompanying backgrounds using the model for the parameterized background version of our fit as described in Section 5.2.1. Expedited simulations run very quickly compared to full simulations and as a result, one can simulate hundreds of ensembles of the complete E687 data set and fit each ensemble to study the distribution of returned fit parameters. Figure 5.22 shows deviations between the fitted and input fit parameters (i.e., $\vec{\alpha}_{fit} - \vec{\alpha}_{parent}$) for 500 simulated data sets each consisting of a number of signal region events equal to the number of signal region events listed in Table 5.3.[23] We show in Tables 5.15 and 5.16 the fitted widths of these distributions and their biases (in units of standard deviation).[24]

---

22 These uncertainties result in errors on the order of 0.5%.

23 For conciseness, we just show the plots for the D^+ deviations. The D_s^+ deviations are similar.

24 We define the $bias/\sigma$ for fit parameter i as the normalized deviation from zero, $\frac{\alpha_{i,fit} - \alpha_{i,parent}}{\sigma_{i,parent}}$.

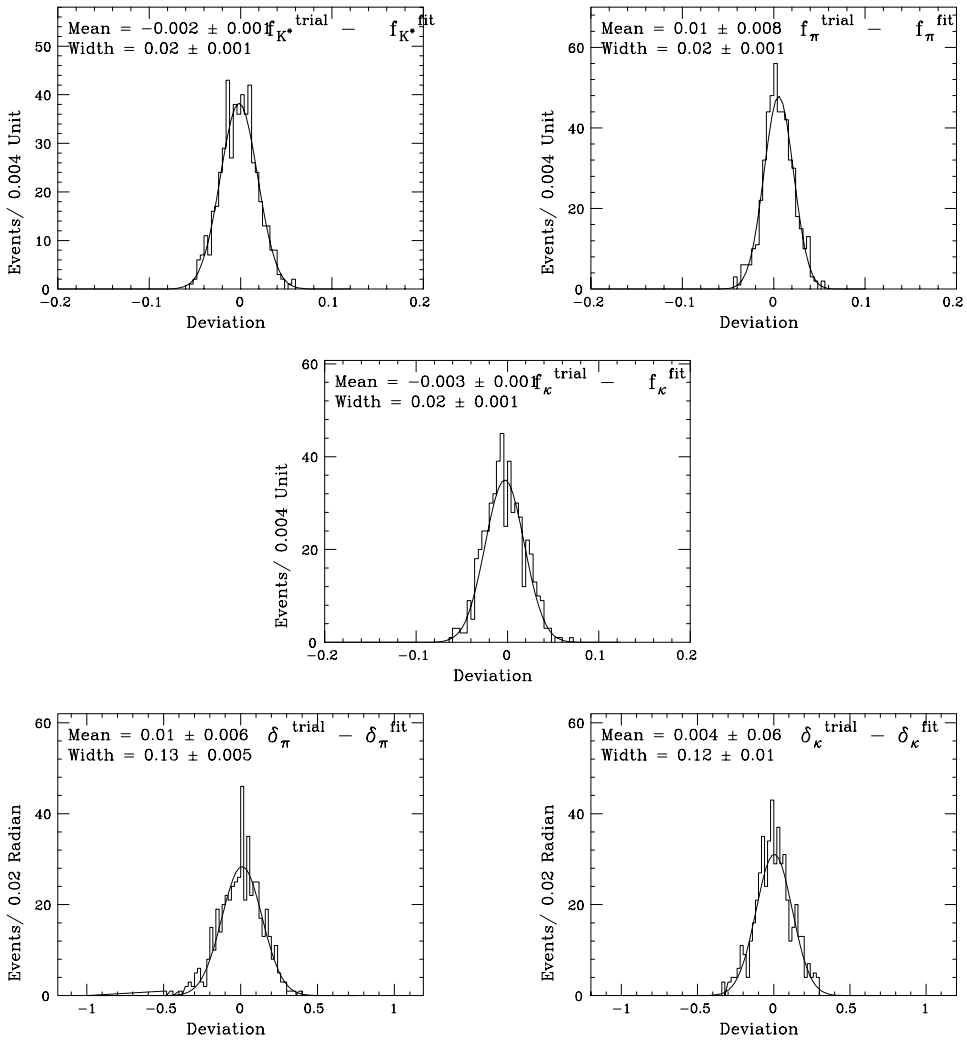

Figure 5.22 Mini-Monte Carlo deviations, D^+ fit.

Table 5.15 D^+ Mini-Monte Carlo Checks

Parameter	σ_{MMC}	σ_{fitter}	Bias
$\delta_{\phi\pi^+}$	7.5^o	7.9^o	0.070
$\delta_{\overline{K}^*(1430)^0K+}$	6.8^o	7.4^o	0.029
$f_{\overline{K}^*(892)^0K+}$	0.020	0.012	-0.139
$f_{\phi\pi^+}$	0.016	0.031	0.179
$f_{\overline{K}^*(1430)^0K+}$	0.021	0.035	-0.081

Table 5.16 D_s^+ Mini-Monte Carlo Checks

Parameter	σ_{MMC}	σ_{fitter}	$Bias/\sigma$
$\delta_{\phi\pi^+}$	19.8^o	18.6^o	-0.131
$\delta_{\overline{K}^*(1430)^0K+}$	40.2^o	32.8^o	0.171
$\delta_{f_0(980)\pi^+}$	21.8^o	16.9^o	-0.035
$\delta_{f_J(1710)\pi^+}$	20.2^o	20.0^o	-0.004
$f_{\overline{K}^*(892)^0K+}$	0.046	0.021	-0.350
$f_{\phi\pi^+}$	0.019	0.033	-0.089
$f_{\overline{K}^*(1430)^0K+}$	0.030	0.032	-0.127
$f_{f_0(980)\pi^+}$	0.035	0.034	0.153
$f_{f_J(1710)\pi^+}$	0.023	0.019	0.580

The extent which the RMS deviations are equal to the statistical errors returned by the fitter in Tables 5.10 and 5.13 indicates how well the fitter estimates these errors.[25] Only $\sigma(f_{\overline{K}^*(892)^0K+})$ for the D^+ is underestimated, so we will use the MMC value for our final fit result.[26] Although the results do show some bias, we

25 MINUIT uses the matrix equation $\frac{\delta^2 - 2\ln\mathcal{L}}{\delta\alpha_i\alpha_j}^{-1}$, evaluated at the final fitted value of $-2\ln\mathcal{L}$, to estimate the matrix of statistical errors.

26 We conservatively choose to quote the larger of the MMC and fitted errors for our final statistical errors.

do not believe it is severe.

5.4.2 Estimating Systematic Error

Because of the complexity of Dalitz fitting it is rather difficult to compute systematic errors directly from known uncertainties about the apparatus or known deficiencies of fitting techniques. In order to facilitate our systematic checks, we define below [17] *split sample* and *fit variant* systematic uncertainties:

1. We split the data sample in disjoint pieces and compare the fit parameters obtained in splits of the data sample. In a fixed target experiment most efficiency corrections (geometric acceptance, Čerenkov particle identification, triggering) are highly momentum dependent, hence a natural split is to divide the sample on the basis of high momentum ($p > 90 GeV/c$) versus low momentum ($p < 90 GeV/c$). The problem in estimating systematics by comparing split sample estimators is deciding how much of the difference in fit parameters is due to statistical fluctuation and how much should be ascribed to systematic error. We use a method for handling this based on the S-factor technique which is used by the Particle Data Group [28] to combine data from statistically inconsistent experiments.
2. One can also estimate systematic errors by varying reasonable fitting techniques for a complete data set. Fit variations include using the helicity amplitudes described in Appendix A and fitting the airgap data. The problem in estimating systematics by comparing fit parameters between fit variants is to decide how to extract a meaningful systematic error from the spread of estimates obtained with the various fit variants.

Our high statistics sample allows many oportunities for systematic checks. Having defined these types of systematic uncertainties, we now must develop a systematics error estimation technique which meets certain goals.

(a) We would like the split sample systematics to be quoted in a common currency with the fit variant systematics if possible.

(b) We would like the quoted systematic error to be essentially independent of the number of systematic sources considered. For example, it isn't really that fair to just add the split sample differences in quadrature to obtain a grand systematic error. Such a scheme insures that this systematic error will tend to grow as the number of splits increases. The same can be said for trying many possible fit variants.

We begin by describing our technique for split sample systematics. Consider splitting the sample in two disjoint sets corresponding to high and low D momentum. The standard test for statistical consistency is to construct a confidence level for the hypothesis that the 2 measurements can be fit by a single (weighted average) fit parameter. For N independent samples, the confidence level would be constructed from a χ^2 with $N-1$ degrees of freedom of the form:

$$\chi^2 = \sum_i^N \frac{(x_i - < x >)^2}{\sigma_i^2} \qquad \text{where} \quad < x >= \frac{\sum_i x_i/\sigma_i^2}{\sum_i 1/\sigma_i^2} \tag{5.23}$$

We can use this χ^2 to extract an estimate of the systematic error in analogy with the S-factor method of the Particle Data Group. [28] Let us consider the case where $\chi^2/(N-1) > 1$. We can say that this inconsistency arises because the split sample true errors are all underestimated because of an unknown systematics problem. If all subsample errors are scaled up to $\sigma_i \sqrt{\chi^2/(N-1)}$, the new χ^2 per degree of freedom will automatically be unity. In addition, the statistical error for the weighted average of the subsample estimates

$$\bar{\sigma} = \frac{1}{\sqrt{\sum_i^N 1/\sigma_i^2}} \tag{5.24}$$

will be increased by the same factor and become a "scaled error" ($\tilde{\sigma}$) of:

$$\tilde{\sigma} = \bar{\sigma} \sqrt{\chi^2/(N-1)} = \sqrt{\frac{< x^2 > - < x >^2}{N-1}} \tag{5.25}$$

where we use the weighted averaging brackets $<\ >$ defined in Eq. (5.23). Let σ_f be the statistical error returned by the fitter on the unsplit data set. Our procedure is to quote a "split sample" systematic error of:

$$\boxed{\begin{array}{ll} \sigma_{\rm sys}^{\rm split} = \sqrt{\tilde{\sigma}^2 - \sigma_f^2} & \text{If } \tilde{\sigma} > \sigma_f \\ \sigma_{\rm sys}^{\rm split} = 0 & \text{If } \tilde{\sigma} \leq \sigma_f \end{array}} \tag{5.26}$$

By construction this systematic error is able to separate true indications of systematics problems from normal statistical fluctuations. Furthermore the error $\tilde{\sigma}$ and $\sigma_{\rm sys}$ will tend to be independent of the number of subsamples N and thus satisfy Goal B. As one increases N the variance of each subsample ($< x^2 > - < x >^2$) will grow proportional to N since the statistics of each sample is reduced by a factor of $1/N$. The factor of $N-1$ in Eq. (5.25) will tend to cancel this growth, while simultaneously making the result degenerate at $N = 1$. This property is desired since one can't assess split sample systematics without splitting the sample!

We turn next to a discussion of fit variant systematics. We now try to see if we can extend the split sample systematics method to cover fit variant systematics. This would insure that we meet the criteria of a common currency (Goal A). The fit variant systematics is different from the split sample systematics in the three following respects:

1. We assume that the fit variants are all *a priori* likely. This means we should not use the weighted average implied by Eq. (5.23) but rather use a straight average: $< x >= \sum_i^N x_i/N$.

2. Furthermore, we are not making a combined average of the fit variants where each variant is adding independent information. As a result we should remove a factor of $1/\sqrt{N}$ in the $\tilde{\sigma}$ expression which reflected the fact that we were averaging the N split samples to get an error on the

combined sample. In this sense we *were* trying to get the error on the mean of a set of parameters. *Now* we are trying to assess the actual rms spread in a set of estimators rather than the spread on the mean. The answers to these two questions differ by $1/\sqrt{N}$.

3. Lastly there is no need to subtract the statistical variance from $\tilde{\sigma}^2$, since the fit variations should essentially have fully correlated statistical errors.

Making these modifications we get:

$$\sigma_{\rm sys}^{\rm variant} = \sqrt{\frac{\sum_i^N \; x_i^2 - N < x >^2}{N-1}} \tag{5.27}$$

Eq. 5.27 is the expression for the *sample* standard deviation and differs from the *population* standard deviation by $N \rightarrow N-1$

Because Eq. 5.27 for the "fit variant" systematic error is really a special case of Eq. (5.25) we automatically have a common currency of errors. In addition the sample standard deviation should be roughly independent of the number of events in the sample so long as reasonable fit variants actually follow a normal distribution.

Lastly we believe that fit variant systematics, which reflect uncertainty in technique, are essentially independent of split sample systematics, which indicate uncertainty of modeling as gauged by the degree of internal inconsistency of the data. For this reason we would add the fit variant systematic error to the split sample systematic error in quadrature to get the combined systematic error. We report in tables 5.17 the final results and systematic errors. The split sample systematic errors are calculated according to equation 5.26 using low and high momentum samples. The fit variants considered are:

- Using helicity amplitudes.
- Fitting the airgap sample.

- Setting the error on the signal fraction $\sigma_{\mathcal{F}}$ to infinity.
- Fitting a sample reconstructed with the stand-alone vertexer (Sec. 4.1.6.2)
- Setting the Blatt-Weiskopf vertex form factors F_D, F_r to unity.

Table 5.17 Fit Results

Parameter	D^+	D_s^+
$\delta_{\overline{K}^*(892)^0K+}$	0^o (fixed)	0^o (fixed)
$\delta_{\phi\pi+}$	$-159 \pm 8 \pm 11^o$	$178 \pm 20 \pm 24^o$
$\delta_{\overline{K}^*(1430)^0K+}$	$70 \pm 7 \pm 4^o$	$152 \pm 40 \pm 39^o$
$\delta_{f_0(980)\pi^+}$	-	$159 \pm 22 \pm 16^o$
$\delta_{f_J(1710)\pi^+}$	-	$110 \pm 20 \pm 17^o$
$f_{\overline{K}^*(892)^0K+}$	$0.301 \pm 0.020 \pm 0.025$	$0.478 \pm 0.046 \pm 0.040$
$f_{\phi\pi+}$	$0.292 \pm 0.031 \pm 0.030$	$0.396 \pm 0.033 \pm 0.047$
$f_{\overline{K}^*(1430)^0K+}$	$0.370 \pm 0.035 \pm 0.018$	$0.093 \pm 0.032 \pm 0.032$
$f_{f_0(980)\pi^+}$	-	$0.110 \pm 0.035 \pm 0.026$
$f_{f_J(1710)\pi^+}$	-	$0.034 \pm 0.023 \pm 0.035$

5.5 Assessing Goodness of Fit

It is clearly important to be able to quantitatively report on how well the measured intensity function actually matches the data.[27] For one dimensional distributions, a standard technique is to bin the data into a histogram, overlay the fitted prediction and quote a confidence level based on the value of χ^2, which describes how well the predicted bin contents matches the observed populations given the number of degrees of freedom in the histogram.

27 This section is borrowed from Ref [34].

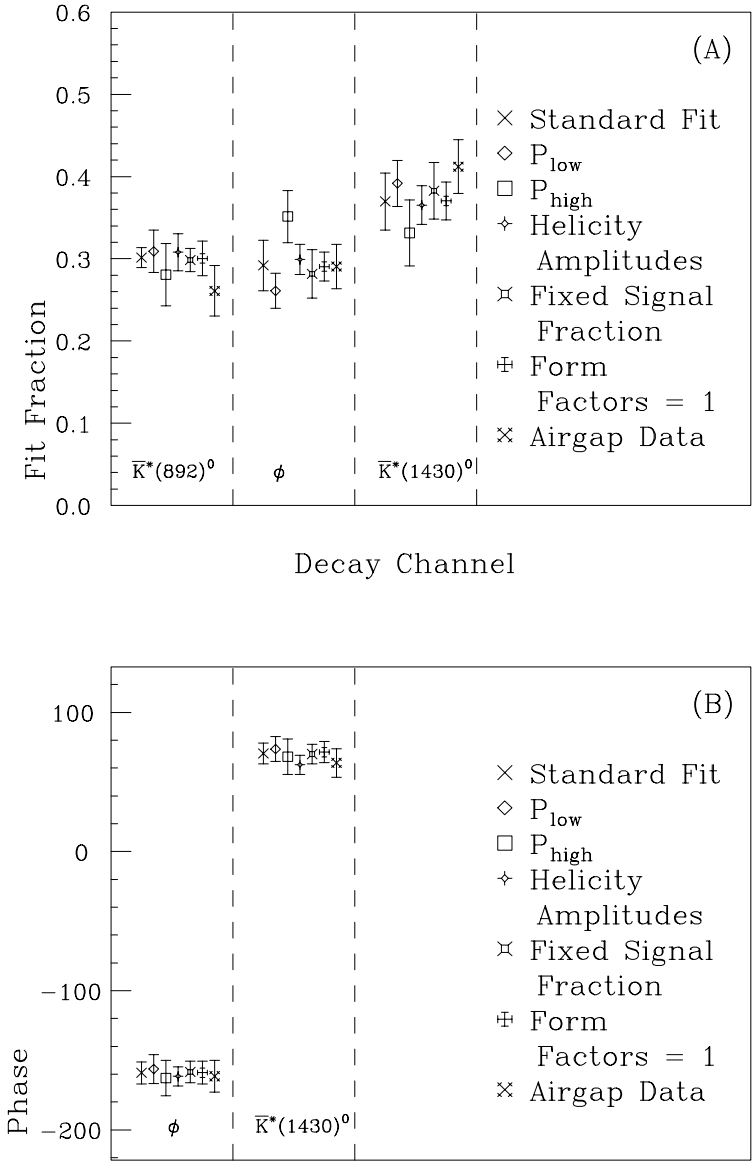

Figure 5.23 D^+ systematic checks: A) Decay fractions; B) Fitted phases.

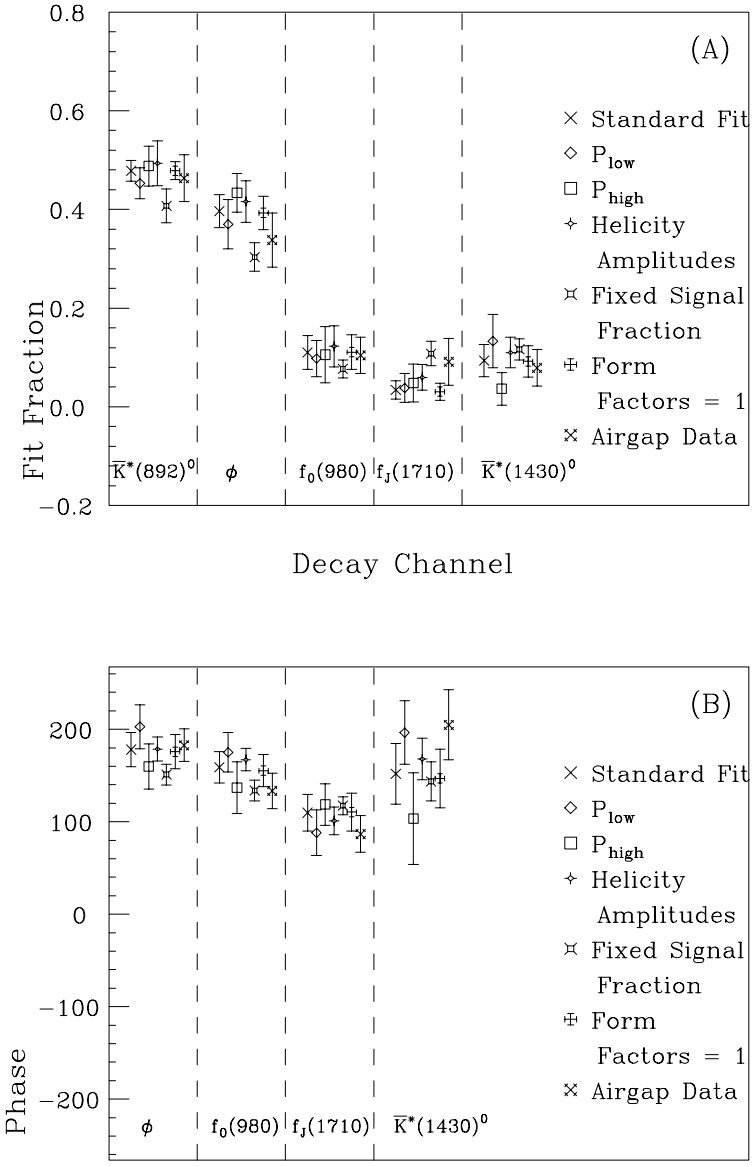

Figure 5.24 D_s^+ systematic checks: A) Decay fractions; B) Fitted phases.

The case of two dimensional distributions is somewhat more problematic. The ARGUS collaboration [16] discusses the use of a confidence level test to assess goodness of fit which is based on the log likelihood distribution for an ensemble of simulated data sets. The idea here would be to quote a confidence level as the fraction of times the log likelihood variable (w) for simulated data sets exceeds the actual log likelihood variable returned by the fit to the data. Each simulated data set would in principle be generated with the measured intensity returned by the fit. We call this method of assessing the goodness of fit the "likelihood confidence level". The ARGUS collaboration made the very useful observation that in typical fits to the Dalitz plot, the number of fit parameters is often so large that the w variable for an ensemble of fits closely approximates a Gaussian distribution with a centroid and variance given by:

$$< w >= N \int I(\vec{x})[-2 \times \ln I(\vec{x};\alpha)]d\vec{x} \; - \; n \tag{5.28}$$

$$\sigma(w^2) = \sqrt{N^2 \int I(\vec{x};\vec{\alpha})[-2 \times logI(\vec{x};\vec{\alpha})]^2 d\vec{x} \; - \; (< w > +n)^2} \tag{5.29}$$

where the integrals range over the Dalitz variables, $\vec{x} = (M^2_{ab}, M^2_{ac})$, and use the efficiency corrected intensity for the parameters returned by the fit, $\vec{\alpha}$. n is the number of fit parameters and N is the number of signal events predicted by the fit, $\mathcal{F} \times$ number of signal region events. We confirm that the ARGUS approximation works beautifully for our Dalitz fits as well, thereby saving the computer time required to generate ensembles of datasets.

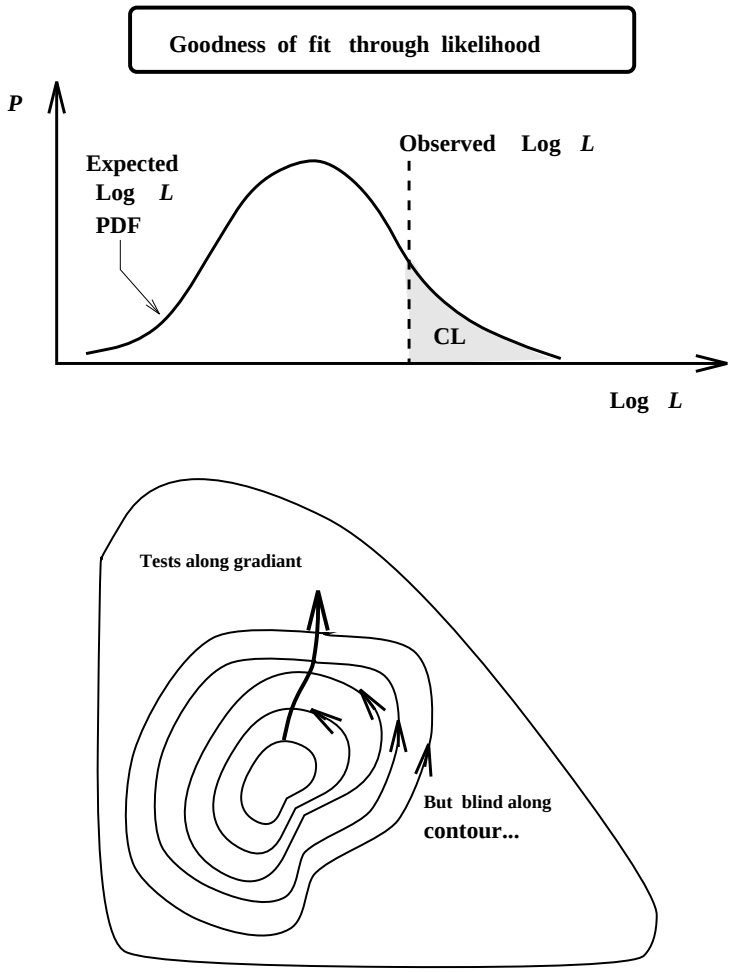

Figure 5.25 Illustration of the likelihood confidence level for an ensemble of simulated data sets.

Through the inclusion of a sufficient number of amplitudes, the ARGUS Collaboration [16] was generally able to produce fits with an acceptable, likelihood confidence level. Our experience has been quite similar; we are always able to find at least one fit to the $KK\pi$ Dalitz plots with a likelihood confidence level which exceeded 30 %. On the other hand, we often notice (See Section 5.3) a pattern of statistically significant discrepancies between the predicted and observed histograms of the individual mass squared projections.

We are of the opinion that although an acceptable likelihood confidence level is a necessary and important condition for a good fit it is not a sufficient condition. We have developed what we feel is a more stringent criteria for goodness of fit in response to our observation that fits with poor confidence levels based on χ^2 tests to the various mass-squared projections often have quite acceptable confidence likelihoods. The reasoning that led to our conclusion that an acceptable likelihood confidence level is insufficient information to conclude that one has an acceptable fit can be most easily explained using a hypothetical example.

Imagine that one is trying to fit intensity distributions to a parameterized wave function using a model that assumes that the state is in an s-wave and is therefore isotropic in angle. In reality, let us say that state is in a p-wave. The log likelihood will depend on radius only and thus data for a p-wave state with the same radial wave function will match the expected log likelihood distribution as the s-wave model. But clearly s-wave and p-wave distributions can be distinguished by looking at angular distributions. Even though the s-wave fit has an acceptable likelihood confidence level the s-wave hypothesis does not actually "fit" the wave function. Under the s-wave assumption, radial distribution can be transformed into a projection in log likelihood. This projection is clearly blind to the orthogonal, angular variations of the intensity. A really good model, once tuned from the visible, likelihood projection, will correctly predict the hidden, orthogonal projection as well as correlations between the two projections.

In spite of this view, however, we feel that the likelihood confidence level does have special significance as a necessary condition for a reasonable fit. One often extracts physical parameters using models with arbitrary or minimal parameterizations of those details of the distribution deemed unimportant to the physics (*eg* polynomial backgrounds in a fit to a mass distribution). One is generally concerned that a fit looks good for the physics features one is trying to measure and is not as concerned that the fit fails to match less relevant aspects of the distribution. The likelihood confidence level describes how well the model matches the intensity variations expected in the context of the model but ignores unexpected

variations along the likelihood contour. A very poor likelihood confidence level means that the model can't adequately fit the data along the projection most sensitive to the assumed physics of the model and thus leads one to question the validity of the model as well as the fit parameters returned by the fit. A good likelihood confidence level obtained in a fit with poorly fit projections might be excused by saying that the model is over simplified but the features we were looking at in the extraction our measurements are well reproduced.

Because of the aforementioned problems associated with assessing goodness of fit through single projections, we turned to a χ^2 test based on dividing the Dalitz plot into two dimensional bins using the adaptive binning algorithm discussed in Sec. 5.2.2 and our final fitted amplitudes. To insure the validity of the χ^2 test, we required that each bin chosen by the adaptive binning algorithm preserved a minimal number of predicted and observed counts (typically greater than 10). We thus felt that we had achieved a statistically valid χ^2 test over the finest binning scales supported by our sample size.

We typically ran the algoritm to find a two dimensional χ^2 based confidence level as well as the location of the most troublesome bins which supplied the biggest contributions to the overall χ^2. Subjected to this adaptive binning χ^2 criteria, poor fits of the amplitude model was the rule rather than the exception. For example, our best fits produced the χ^2 reported in Table 5.18.

Table 5.18 Goodness of the Fits

Parent		ARGUS		2-Dimen.
Meson	$-2\ln\mathcal{L}$	$<-2\ln\mathcal{L}>$	$CLVL$	χ^2/DOF
D^+	-723	-771 ± 117	34.2%	92.2 (44 dof)
D_s^+	-1075	-966 ± 129	80.2%	50.2 (33 dof)

In the Table we quote a naive number of degrees of freedom which, as we described in Sec. 5.3.2, underestimates the true number of degrees of freedom. To insure that these poor χ^2 are not artifacts of ignoring resolution, or approximations in

modeling the efficiency, we also apply the adaptive χ^2 test to full Monte Carlo simulations of the decays. As expected, the Monte Carlo samples produced very acceptable χ^2, thus leading us to conclude that the problem lay with the overly simplified physics of the amplitude model we have used. illustrates the severity of our best fits miss-match to the data. The figure shows each adaptively chosen bin's contribution to the over all χ^2 for the Dalitz plot. Fig. 5.26 shows the ratio of the number of observed to predicted events in each of these bins. The pattern of the disagreement, with the ratio straying further from unity at regions removed from the landmark resonance regions, could be caused by an interference with either an unknown broad resonance overlapping in that region (but not others), or by an essentially nonresonant term with a slowly varying phase. Although we cannot isolate a unique cause for this discrepency it has led us to conclude that given enough data one will find that all strong interaction effects which affect nonleptonic charm decay cannot be modeled as a pure linear combination of Breit-Wigner resonances with constant strengths and relative phases.

5.6 $K^+K^-\pi^+$ Branching Fractions

An important application of the present Dalitz amplitude analysis is the extraction of branching fractions into the inclusive $K^+K^-\pi^+$ final state. Often [28] for convenience, "branching fractions" are quoted for the decays of charmed particles into particular intermediate state resonant modes (eg. $D^+ \to \phi\pi^+$) which because of the possibility of interference should actually be described by amplitudes rather than partial widths.[28] The amplitude fits described here automatically take into account the small but non-negligible effects of interference as well as providing a detailed intensity model for correcting the inclusive yield to account for non-uniformities in the acceptance across the Dalitz plot.

28 Although the charm particle decay into resonant intermediate states should be described by an amplitude rather than an intensity, we quote "branching fractions" into the intermediate two-body resonant states to allow comparison of our results with other groups in Table 5.19.

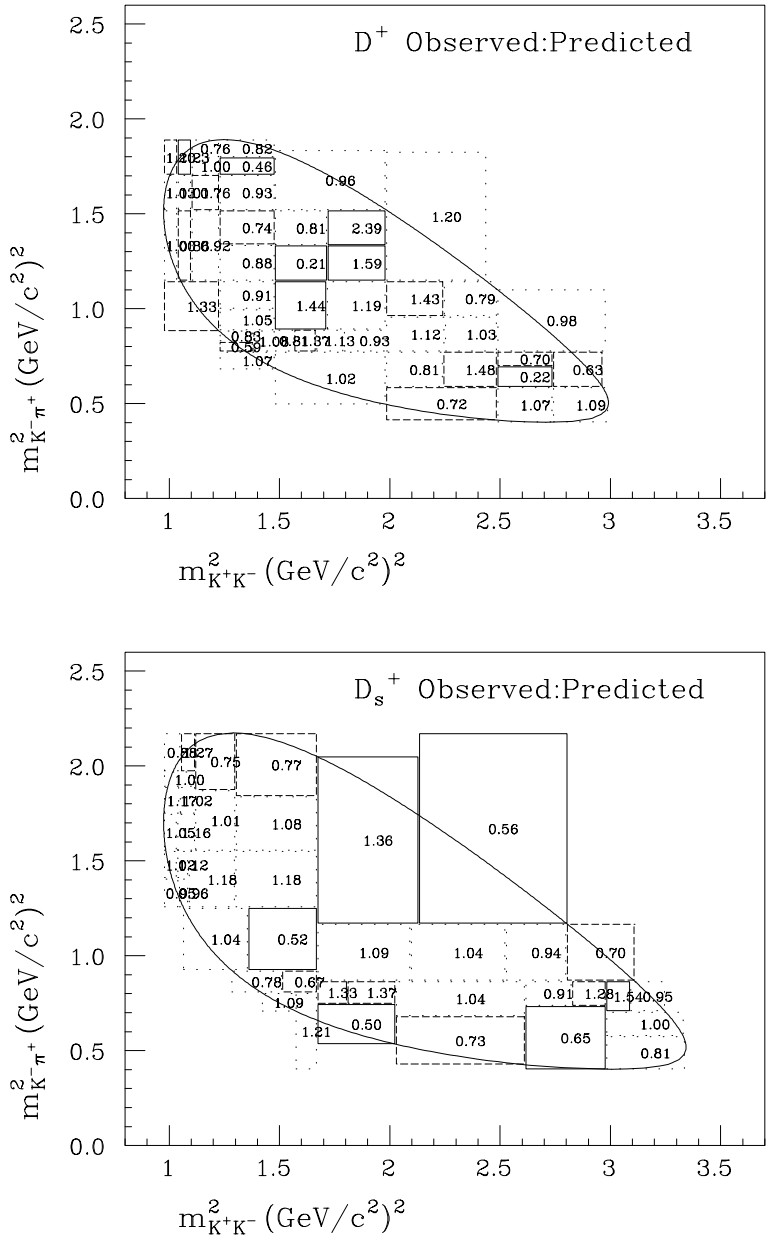

Figure 5.26 The ratio of the number of observed to predicted events in each of the bins used calculate the two-dimensional χ^2.

We have resisted the temptation to quote branching fractions for any of the decays mentioned in Tables 5.17 other than the landmark final states $\overline{K}^*(892)^0K^+$ and $\phi\pi^+$ or set an upper limit on nonresonant (phase space) $K^+K^-\pi^+$ decays. Although we have presented evidence for the presence of each of the broad resonances included in our fits, we lack sufficient statistics to exclude alternative fits where the set of resonance contributions is expanded. Because of interference effects, these broad resonance contributions can fluctuate wildly in expanded fits while the the landmark $\overline{K}^*(892)^0K^+$ and $\phi\pi^+$ contributions remain stable within quoted errors.

Because the existing $D^+ \to K^+K^-\pi^+$ absolute branching fraction measurement is based on a very low statistics sample [36], we extract ratios of partial widths for the D^+ decays[29] by using the following formula:

$$\frac{\Gamma(D^+ \to \phi\pi^+)}{\Gamma(D^+ \to K^-\pi^+\pi^+)} = \frac{1}{\Gamma(D \to K^-\pi^+\pi^+)} \times \frac{\Gamma(D \to K^+K^-\pi^+)\ f(D \to \phi\pi^+)}{B(\phi \to K^+K^-)} \tag{5.30}$$

The experimental ratio $\frac{\Gamma(D^+ \to K^+K^-\pi^+)}{\Gamma(D^+ \to K^-\pi^+\pi^+)}$ represents the ratio of efficiency corrected yields for $D^+ \to K^+K^-\pi^+$ and $D^+ \to K^-\pi^+\pi^+$ and has a value of $0.0976 \pm 0.0042 \pm 0.0046$. The second factor is the current world average [28] absolute branching fraction for $D^+ \to K^-\pi^+\pi^+$.[30] We compare our measured branching ratios to other recent measurements in Table 5.19.[31]

It is interesting to compare these measurements to model predictions. We can convert the ratios of partial widths in Table 5.19 to absolute branching ratios by multiplying by the world average [28] absolute partial width of the $D^+ \to K^-\pi^+\pi^+$ decay[32] . Both the BSW [4] and BLMPS [37] models employ

29 We neglect the D_s^+ branching fractions because it depends on the theoretical ratio $\frac{\Gamma(D_s^+ \to \phi\mu^+\nu)}{\Gamma(D^+ \to \overline{K}^*(892)^0\mu^+\nu)}$, which is not well determined. It lies in the range 0.78 - 1.02. [28]

30 We use our published [17] amplitude for $D^+ \to K^-\pi^+\pi^+$ to get the $K\pi\pi$ efficiency corrected yield.

31 The first error is statistical, the second is systematic, the third is due to the theoretical uncertainty in $\frac{\Gamma(D_s^+ \to \phi\mu^+\nu)}{\Gamma(D^+ \to \overline{K}^*(892)^0\mu^+\nu)}$. See Appendix B for additional remarks about the estimation of branching fraction errors.

32 It has a value 0.091 ± 0.006.

factorization of the decay amplitude. In addition, BLMPS includes a contribution from final state interactions. The comparison of our results and the models is shown in Table 5.20 below.

Table 5.19 Ratios of Partial Widths

Exp.	$\frac{\Gamma(D^+\to\overline{K}^*(892)^0K^+)}{\Gamma(D^+\to K^-\pi^+\pi^+)}$	$\frac{\Gamma(D^+\to\phi\pi^+)}{\Gamma(D^+\to K^-\pi^+\pi^+)}$
this work	$0.044 \pm 0.003 \pm 0.004$	$0.058 \pm 0.006 \pm 0.006$
CLEO		$0.077 \pm 0.011 \pm 0.005$
NA14		$0.098 \pm 0.032 \pm 0.014$
WA82		$0.062 \pm 0.017 \pm 0.006$
E691	$0.058 \pm 0.009 \pm 0.006$	$0.071 \pm 0.008 \pm 0.007$
MARK III	$0.048 \pm 0.021 \pm 0.011$	$0.084 \pm 0.021 \pm 0.011$

Table 5.20 Comparison of Absolute Branching Ratios

	this work	BSW [4]	BLMPS [37]
$\frac{\Gamma(D^+\to\overline{K}^*(892)^0K^+)}{\Gamma(D^+\to all)}$	$0.0040 \pm 0.0003 \pm 0.0004$	0.0044	0.0025
$\frac{\Gamma(D^+\to\phi\pi^+)}{\Gamma(D^+\to all)}$	$0.0053 \pm 0.0006 \pm 0.0006$	0.0028	0.0059

Very generally speaking, BSW agrees with our measured $\overline{K}^*(892)^0K^+$ branching ratio, whereas BLMPS matches our value for the $\phi\pi^+$ fraction. In Sec. 5.7 we discuss final state interaction effects.

5.7 Comments About Final State Interactions

Although much of the interest in Dalitz amplitude analyses is centered on the measurement of new charm branching ratios, the fitted relative phases $\{\delta\}$ provide important information about strong rescattering effects in the final state. It is instructive to borrow the phenomenology of neutral kaon decay to infer information from the present Dalitz analysis.[33] In the decays $K \to \pi\pi$, the

33 This discussion borrows material from Secs. VIII-4 and IX-2 in Ref. [30]

$s-$ wave di-pion final state has a total isotopic spin of either 0 or 2. Thus, such decays can be parameterized by the amplitudes

$$\begin{aligned}
\mathcal{A}_{K^0\to\pi^+\pi^-} &= |A_0|e^{i\xi_0}e^{i\delta_0} + \frac{|A_2|}{\sqrt{2}}e^{i\xi_2}e^{i\delta_2}, \\
\mathcal{A}_{\overline{K}^0\to\pi^+\pi^-} &= -|A_0|e^{i\xi_0}e^{i\delta_0} - \frac{|A_2|}{\sqrt{2}}e^{-i\xi_2}e^{i\delta_2}
\end{aligned} \tag{5.31}$$

The subscripts 0 and 2 represent the isospin quantum number. The phases $\xi_{0,2}$ parameterize CP-violation, whereas the phases $\delta_{0,2}$ model scattering of the two outgoing pions (i.e., final state interactions). Note that under the CP operation, $i\xi$ becomes $-i\xi$ but $i\delta$ does not change. In the limit of no CP-violation (i.e., $\xi \to 0$), Watson's theorem tells us that all imaginary phases (i.e., phases consistent with 90^o) in the decay amplitude are due to final-state interactions.

Our amplitudes for $KK\pi$ decays of charm follow a similar construction. Very generally speaking, the particle/anti-particle decay amplitudes are written (see Sec. 5.2) as follows:

$$\begin{aligned}
\mathcal{A} &\propto \frac{1}{m^2(K^-\pi^+) - \left(m_{K^*} - i\frac{\Gamma_{K^*}}{2}\right)^2} + \frac{1}{m^2(K^+K^-) - \left(m_\phi - i\frac{\Gamma_\phi}{2}\right)^2} e^{i(\delta_\phi - \delta_{K^*})} \\
\overline{\mathcal{A}} &\propto \frac{1}{m^2(K^+\pi^-) - \left(m_{K^*} - i\frac{\Gamma_{K^*}}{2}\right)^2} + \frac{1}{m^2(K^-K^+) - \left(m_\phi - i\frac{\Gamma-\phi}{2}\right)^2} e^{i(\delta_\phi - \delta_{K^*})}
\end{aligned} \tag{5.32}$$

To the extent that $\phi\pi$ and K^*K final state interactions are elastic (ie, the process $\phi\pi \to K^*K$ is ignorable) and there are no narrow $\phi\pi$ or K^*K resonances to induce rapid phase shifts in the $KK\pi$ mass region $M(D^+) < M(KK\pi) < M(D_s^+)$, we would expect same relative $\phi\pi/K^*K$ phase for the D^+ and D_s^+. In other words,

$$|\sin_{D_s}(\delta_\phi - \delta_{K^*})| \simeq |\sin_{D^+}(\delta_\phi - \delta_{K^*})|$$

is what we expect. Our fits obtain

	$\delta_\phi - \delta_{K^*}$
D^+	$-159 \pm 8 \pm 11^o$
D_s^+	$178 \pm 20 \pm 24^o$

which obtains $|\sin(\delta_\phi - \delta_{K^*})| \simeq 0$ for both the D^+ and D_s^+. From our comments at the beginning of this section, this finding suggests that there is either very little final state rescattering between the outgoing $\phi\pi^+$ and $\overline{K}^*(892)^0 K^+$ channels at charmed mass scales, or the rescattering is the same and the phase shift cancels. However, if we compare the difference in fitted phase for the $K^*(1430)K^+$ and $K^*(892)K^+$ channels, we have

	$\delta_{K^*(1430)} - \delta_{K^*}$
D^+	$70 \pm 7 \pm 4^o$
D_s^+	$152 \pm 40 \pm 39^o$

which are consistent at about the 1.46 standard deviation level. They are also consistent with relatively imaginary phase, which indicates there are considerable final state interactions between these two channels. We knew from visual inspection that the pattern of interference with the upper $K^*(892)$ lobe required interference from a relatively imaginary amplitude so the large degree of FSI was apparent from the start (see L_4 in Fig. 5.14).

5.8 Closing Remarks

We have presented a $D^+, D_s^+ \rightarrow K^+K^-\pi^+$ Dalitz plot analysis. Although both decays are dominated by the two-body intermediate states $\phi\pi^+$ and $\overline{K}^*(892)^0 K^+$, they display dramatic differences. The bottom line is that while the physics included in our formalism describes the gross features of the data, it fails to mimic the fine interference structures in these decay amplitudes. Future experiments with larger datasets may be able to provide clues about more complete models which include more strong interaction effects.

Chapter 6

The $D^+, D_s^+ \to \pi^+\pi^-\pi^+$ Dalitz Plot

In this chapter we analyze the decays $D^+, D_s^+ \to \pi^+\pi^-\pi^+$ (and charge conjugate). [38, 39] We will show that the di-pion spectra of the D^+ and D_s are dominated by the intermediate $\rho\pi^+$ and $f_0(980)\pi^+$ resonances. Previous Dalitz amplitude analysis of these states has been reported by the E691 Collaboration [22]. Our resulting branching fractions are consistent with these previous measurements.

Because of the relative rarity of three-pion D^+ and D_s^+ decays, and the harshness of cuts required to pull these signals over the very copious three-pion combinatoric background, we are left with signal yields which are about an order of magnitude smaller than the $KK\pi$ samples we analysed in Chapter 5. This statistical limitation hinders our ability to consider more than just two amplitude contributions. We are able to obtain satisfactory fits using (in both cases) a single, dominent di-pion resonance interfering with a constant, nonresonant amplitude. Due to our limited statistics we are unable to determine to what extent this constant ampltude contribution is in fact a real decay amplitude or rather an amplitude which we included to represent a collection of broad resonances which appear as nearly constant amplitudes over the kinematical region of the Dalitz plot.

The chapter begins with a description of the cuts used to bring out the signal. We next outline the background model, efficiency correction and the (neglible) mass resolution effects. Next we describe the fit formalism, which is slightly modified by the need to Bose symmetrize the amplitudes. Finally, the Dalitz fit results are presented and the branching fractions are calculated.

6.1 The $D^+, D_s^+ \to \pi^+\pi^-\pi^+$ Signal

The global vertex skim, which requires evidence for multiple vertices without regard to specific decay modes (as described in Chapter 4), provides a minimum

bias dataset for our analysis.[1] We search these skim tapes for three-body all-charged final states which satisfy the following cuts:

(a) the confidence level of the secondary vertex (DCL) exceeds 10%.

(b) $Z^{norm}_{secondary} > 5$, $Z^{norm}_{primary} < 0$, $Z^{norm}_{TR1} < 0$.

(c) Second-level trigger satisfied.

(d) $CL1 < 30\%$, confidence level of the primary vertex (PCL) greater than 20%.

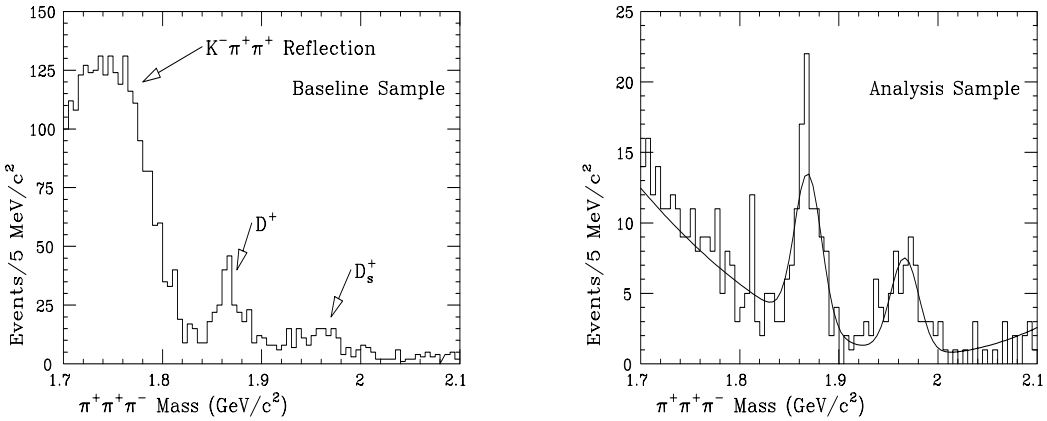

Figure 6.1 Invariant mass of histograms of the $\pi^+\pi^+\pi^-$ signals under various cuts described in the text. The curves represent fits to Gaussian signal peaks over a 4th order polynomial background. In each case the Gaussian width is fixed to the value obtained in Monte Carlo. The Dalitz amplitide fit is performed on the 'Analysis Sample.'

The normalized measures of the Z-component of the secondary vertex with respect to the experimental target and the $TR1$ trigger counter are as defined in Eqs. 5.1 and 5.2. $Z^{norm}_{primary}$ is the normalized z-component of the primary vertex

1 In the early stages of this analysis, we were concerned that a skim-level Čerenkov cut might reject too many events, so we elected to skim only on the vertex topology of the event.

with respect to the downstream end of the beryllium target Z_{targ} -

$$Z^{norm}_{primary} = \frac{Z_{primary\ vertex} - Z_{targ}}{\sigma(Z_{primary\ vertex})} \tag{6.1}$$

The cuts (b) allow us to require the primary vertex is ststistically consistent with charm production in the experimental target while the secondary vertex is consistent with coming from the airgap between the beryllium and the first detector element, $TR1$. As in the case of the $KK\pi$ analysis, this *airgap* cut reduces background due to hadronic reinteractions in the target and detector material.

The invariant mass histogram obtained upon applying these *baseline cuts* to the global vertex data is displayed in Figure 6.1. The peak at low mass is due to Čerenkov misidentification of the Cabbibo favored decay $D^+ \to K^-\pi^+\pi^+$ as $D^+ \to \pi^-\pi^+\pi^+$. By imposing a hard cut on the opposite sign pion, $ISTATP = 2\ or\ 3$, we greatly reduce this background. Additional contamination is due to Čerenkov misidentification of $D^{*+} \to D^0\pi^+ \to (K^-\pi^+)\pi^+$ as the tri-pion state. We remove this reflection by cutting events with $K\pi\pi$ mass consistent with the D^{*+} region, $1.988 < m_{K\pi\pi} < 2.030$.. After applying the *baseline cuts*, the Čerenkov cuts ($ISTATP = 2\ or\ 3$ on the opposite sign pion) and the D^{*+} reflection cut, we obtain the final signal characterized in Table 6.1 below and shown in Figure 6.1. This signal is used for our amplitude fits.

Table 6.1 Sample Statistics

Parameter	D^+	D^+_s
Yield	74 ± 12	49 ± 9
Mass (GeV/c^2)	$1.869 \pm .0021$	$1.966 \pm .0027$
Width σ (GeV/c^2)	0.01359 (fixed)	0.01420 (fixed)
Integrated Signal:Background	$2.42 \pm .609$	5.16 ± 1.17
Signal Fraction $\mathcal{F}_0$	$.708 \pm .052$	$.838 \pm .031$
Overall Efficiency (%)	1.0 ± 0.01	0.5 ± 0.01

The fitted widthes are fixed to the values obtained from a $c\bar{c}$ Monte Carlo simulation. The fit function overlaid on the mass histogram is two Gaussians plus a quadratic polynomial to model the background. Note the signal widths are not well reproduced by the Monte Carlo widths. This mismatch may simply be due to fluctuations with small statistics.

We will use the same maximum likelihood method employed in the $KK\pi$ Dalitz analysis for the $\pi\pi\pi$ decay. Hence, the next step is to define signal and sideband regions. The sidebands are all 2σ wide and are separated from the signal regions by 1σ. We characterize them below in Table 6.2.

Table 6.2 Signal and Sideband Regions

Region	Mass cut (GeV/c^2)	Events
D^+ low sideband	$1.801 < m(KK\pi) < 1.828$	25
D^+ signal region	$1.842 < m(KK\pi) < 1.896$	106
D^+ high sideband	$1.910 < m(KK\pi) < 1.937$	13
D_s^+ low sideband	$1.895 < m(KK\pi) < 1.924$	11
D_s^+ signal region	$1.938 < m(KK\pi) < 1.995$	58
D_s^+ high sideband	$2.009 < m(KK\pi) < 2.037$	4

An essential question in fitting the amplitude is what channels to include in the amplitude sum Eq. 2.10. Our choice is guided by landmarks in the di-pion mass projections shown in Fig. 6.2 for the D^+ and D_s^+. Because there are two neutral dipion combinations ($\pi^+\pi-_{low}$ and $\pi^+\pi^-_{high}$) for every $\pi^+\pi^+\pi^-$ decay, we increment the Fig. 6.2 histograms twice for each tri-pion combination. The dominant resonance in the D^+ di-pion spectrum appears to be the $\rho(770)$, while that for the D_s^+ is the $f_0(980)$. Both the D^+ and D_s^+ projections appear to consist of these resonance peaks along with either broad or non-resonant structures over a background. Given our limited statistics, we chose to model this broad constribution with a single constant, nonresonant amplitude which might well be

a stand in for a complex mix of broad resonances. Hence our model for the D^+ is a mixture of three-body nonresonant which interferes with $\rho(770)\pi^+$. Our model for the D_s^+ is a mixture of three-body nonresonant and $f_0(980)\pi^+$.

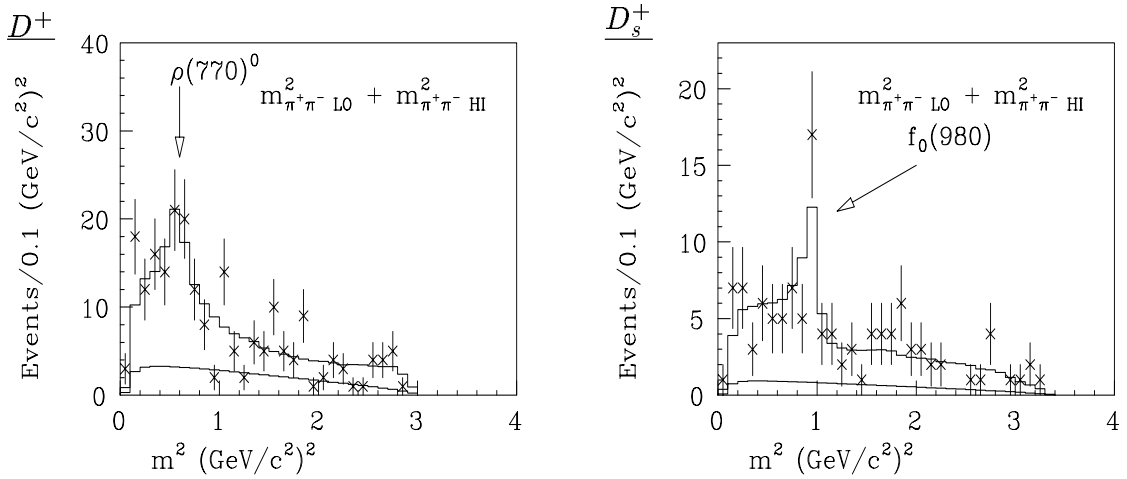

Figure 6.2 The summed mass-squared projections (i.e., $m^2_{low} + m^2_{high}$) for signal region events in the D^+ and D_s^+ mass peaks. We expect statistically significant resonance structures to show up as bumps on these plots. Some evidence for ρ and f_0 are indicated on these projections. Data are points with error bars, large histogram is the predicted sum of signal and background, and the small histogram is the predicted background distribution. These predictions are described in the text.

The Dalitz scatterplots for the D^+ and D_s^+ signal regions are shown in Figure 6.3. We plot the higher $\pi^+\pi^-$ squared mass on the vertical axis and the lower $\pi^+\pi^-$ squared mass on the horizontal axis. In this way, each datum occurs only once on this so-called *folded* Dalitz plot. It is useful to compare the Dalitz plot obtained in the data to the simulated Dalitz plots of known di-pion resonances shown in Fig. 6.4. The D_s^+ Dalitz plot reproduces the "L" band structure of the $f_0(980)$ simulation while the situation for the D^+ is far less obvious. Although the ρ appears clearly in the D^+ di-pion projection, the Zemach zero (quite evident in the simulated Dalitz plot for $\rho(770)$) is very difficult to see in the data. Perhaps it is being populated by background and/or nonresonant contributions.

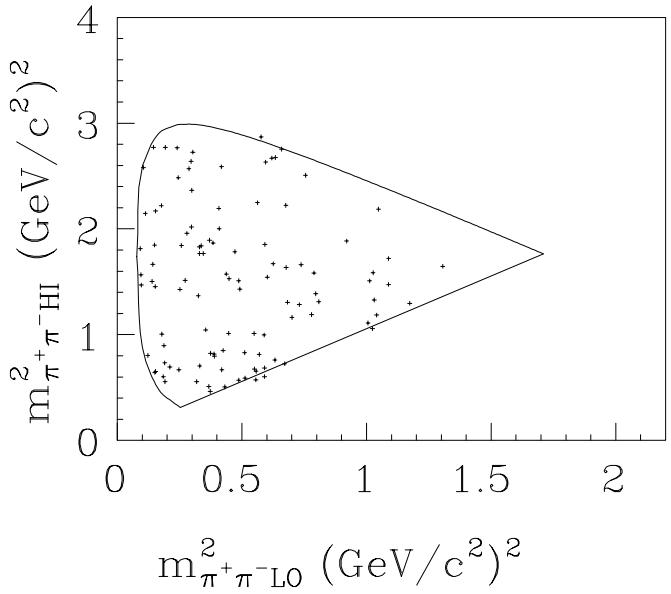

Figure 6.3a Dalitz scatterplot for the $D^+ \to \pi^+\pi^+\pi^-$ final state.

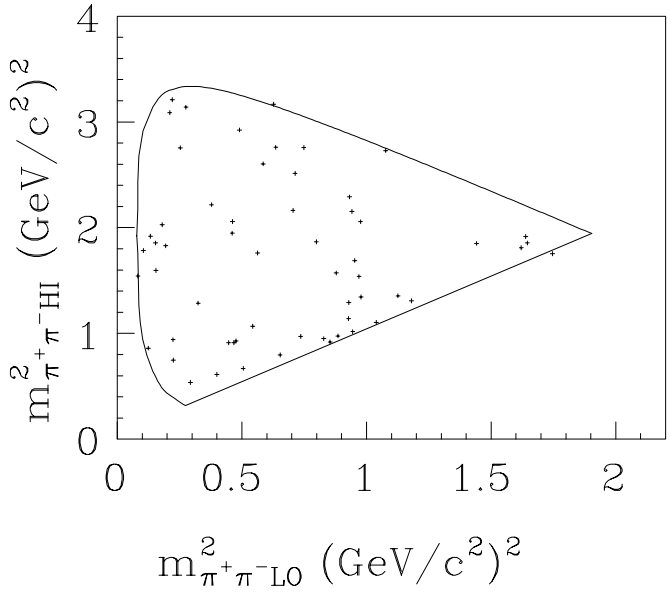

Figure 6.3b Dalitz scatterplot for the $D_s^+ \to \pi^+\pi^+\pi^-$ final state.

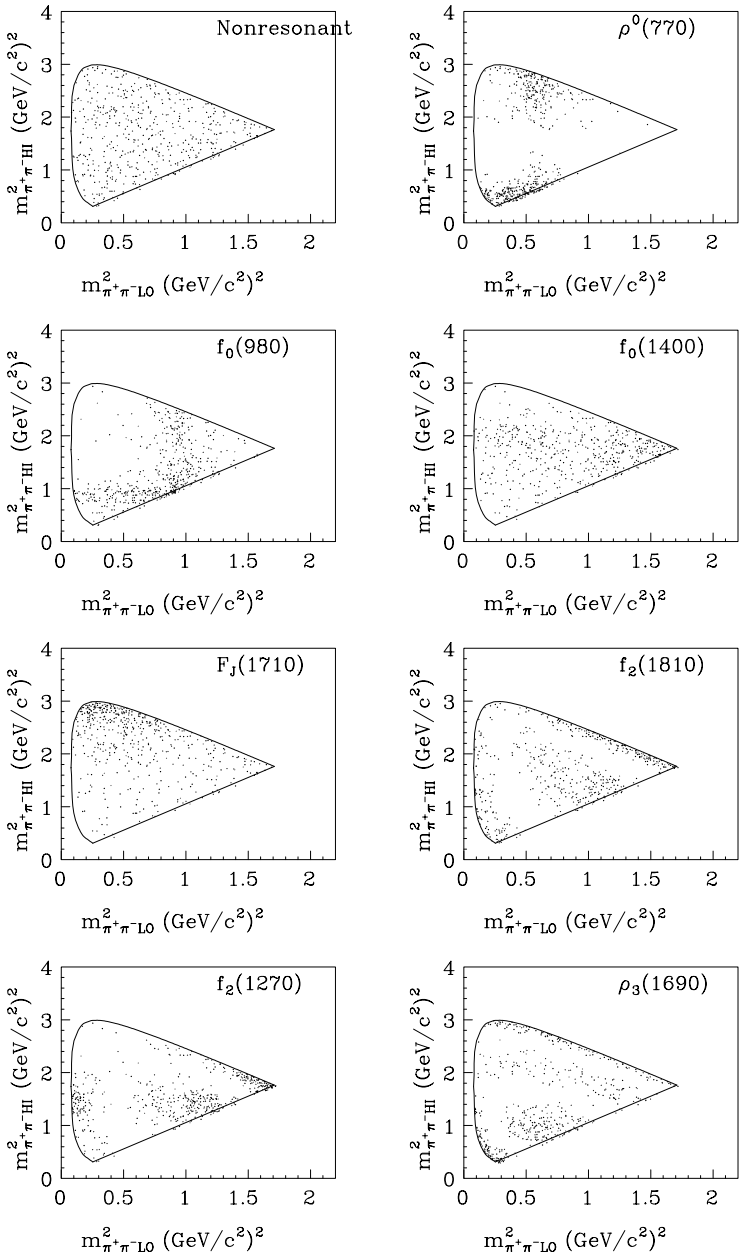

Figure 6.4 Simulated decay channels on the D^+ Dalitz boundary.

6.2 Background Parameterization

Because our background sample is very small, we do not have the statistical strength to model the sideband distributions as a polynomial in the Dalitz variables as we did for the $\pi\pi\pi$ Dalitz plots. Instead, we model the $\pi\pi\pi$ background Dalitz distributions with a flat intensity corresponding to a phase space population. Therefore we assume that the normalized background probability density function is simply

$$pdf_{bg} = \frac{1}{\int_{\mathcal{DP}} d\mathcal{DP}} \tag{6.2}$$

We compare this model to the sideband data in Figs. 6.5 and 6.6 where we show the reconstructed and predicted event distribution in each sideband for the D^+ and D_s^+. On the scatter plot the solid contours represent the sideband central values and the dashed lines the signal region central values. As always, the mass-squared projections are plotted with the sideband data shown as the points with error bars, the phase-space prediction as the histogram.

We assess the quality of this background model via the likelihood confidence levels, as described in Sec. 5.5. These confidence levels are listed in Table 6.3. It appears from this table that,within our limited statistics, a pure phase space description is consistent with the Dalitz plot of the sideband data.

Table 6.3 Sideband Fit Quality Assesment

Region	$-2\log\mathcal{L}_{sb}^{fit}$	$\langle -2\log\mathcal{L}_{sb}^{fit}\rangle$	$CLVL(\%)$
D^+ LSB	39.97	40.1 ± 0.47	61.4
D^+ HSB	27.4	27.5 ± 0.50	59.4
D_s^+ LSB	22.5	22.6 ± 0.44	58.4
D_s^+ HSB	10.2	$10.2 \pm .22$	53.5

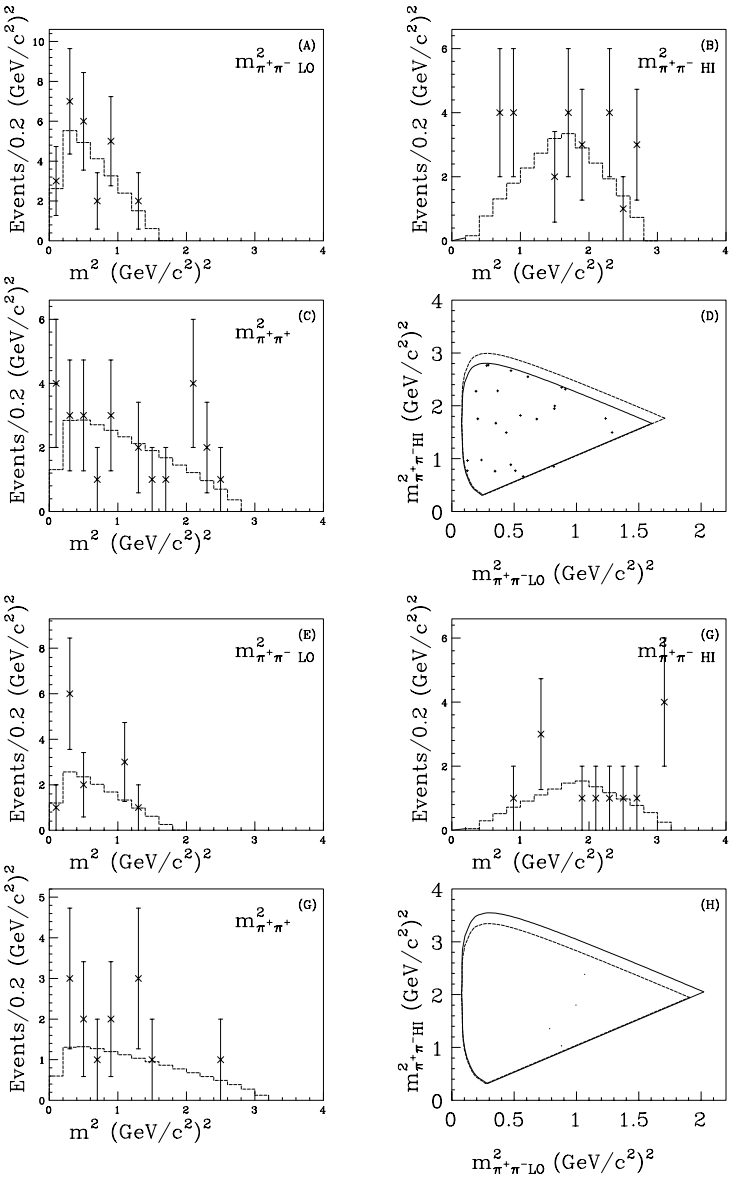

Figure 6.5 D^+ sideband Dalitz plot fit. A) - D) are the low sideband representations; E) - H) the high sideband. In the histograms, the points with error bars are the data, the histogram the prediction of the polynomial model. In the Dalitz scatterplots, the Dalitz boundary is drawn with respect to the center of the respective sideband.

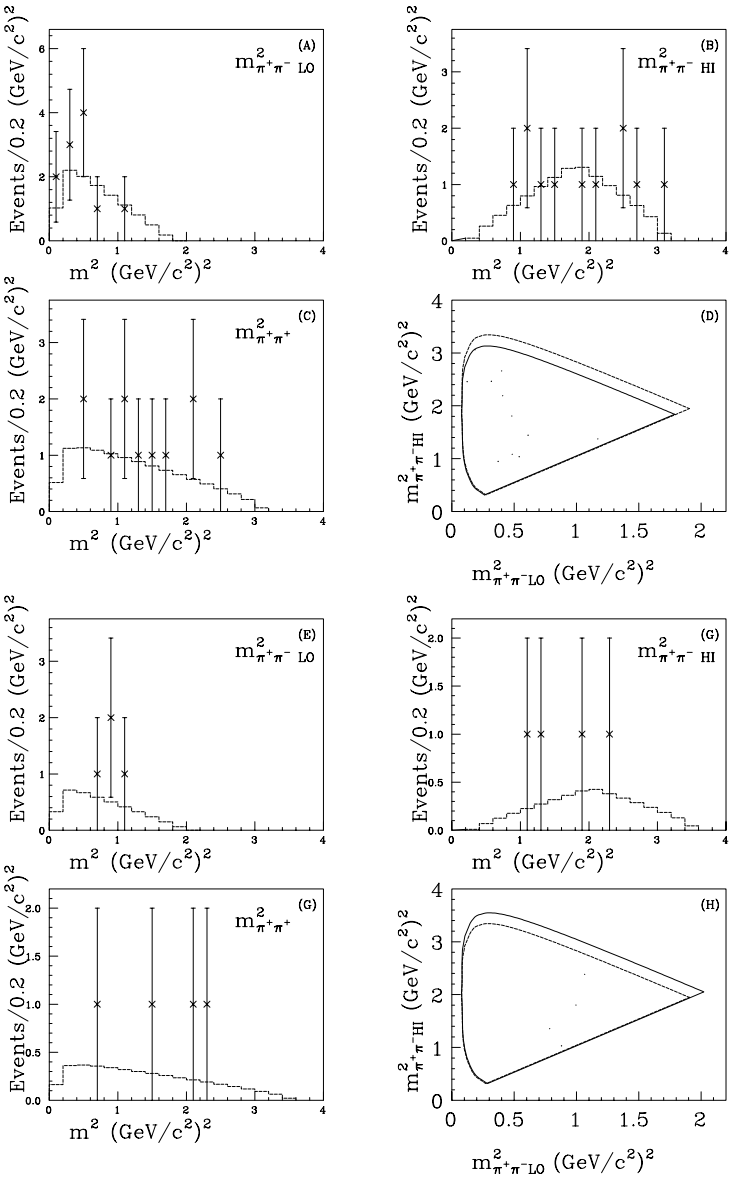

Figure 6.6 D_s^+ sideband Dalitz plot fit. A) - D) are the low sideband representations; E) - H) the high sideband. In the histograms, the points with error bars are the data, the histogram the prediction of the polynomial model. In the Dalitz scatterplots, the Dalitz boundary is drawn with respect to the center of the respective sideband.

6.3 Efficiency Correction and Resolution Effects

Using the standard acceptance correction method described in Section 5.2.2, we obtain the acceptance correction binning shown in Figs. 6.7 and 6.8. For the D^+ Monte Carlo sample we use an amplitude consisting of a coherent superposition of nonresonant and $\rho(770)^0\pi^+$, whereas the D_s^+ sample employs nonresonant and $f_0(980)\pi^+$. The final Monte Carlo samples which pass the analysis cuts are 138 and 77 times as large as the data, for D^+ and D_s, respectively. The RMS variation of the efficiency correction factors is shown in Table 6.4.

Table 6.4 RMS Variation of Relative Efficiencies

Parent Particle	RMS Variation
D^+	0.191
D_s	0.213

We do not expect resolution effects to induce significant biases in our final results. To check this simplification, we fit an (approximately) uncorrelated Monte Carlo sample, i.e., the first 1000 events of the sample we used to obtain the efficiency correction. This sample manifests resolution of the Dalitz observables since it was created with the ROGUE spectrometer simulation. If our simplification is reasonble, a fit to the first 1000 events should obtain results statistically consistent with the generation parameters. Tables 6.5 and 6.6 confirm that neglecting resolution introduces no significant bias in the fitter.

Table 6.5 D^+ Resolution Test

Parameter	Generation Value	Fitted Value
a_{PS}	1.22	$1.22 \pm .05$
a_ρ	1.0 (fixed)	1.0 (fixed)
(continued)		

Table 6.5 D^+ Resolution Test (continued)

δ_{PS}	-35.4^o	-36.0 ± 3.2^o
δ_ρ	0.0^o (fixed)	0.0^o (fixed)
$f_{PS}(\%)$	60.0	60.0 ± 2.0
$f_\rho(\%)$	40.3	40.3 ± 2.0

Table 6.6 D_s Resolution Test

Parameter	Generation Value	Fitted Value
a_{PS}	1.36	$1.30 \pm .10$
a_{f_0}	1.0 (fixed)	1.0 (fixed)
δ_{PS}	24.5^o	24.3 ± 5.0^o
δ_{f_0}	0.0^o (fixed)	0.0^o (fixed)
$f_{PS}(\%)$	48.2	46.4 ± 3.1
$f_{f_0}(\%)$	26.0	27.6 ± 2.8

6.4 Fit Formalism

As usual, we write the amplitude for $D^+, D_s^+ \to \pi^+\pi^+\pi^-$ as a coherent sum of amplitudes as follows:

$$\mathcal{A} = a_0\, e^{i\delta_0} \; + \sum_{resonances\ i} a_i e^{i\delta_i} \mathcal{M}_i$$

where the first term represents the nonresonant contribution and the resonant amplitudes $\mathcal{M}_i$ are Bose-symmetrized. They are written as follows -

$$\mathcal{M}_i = B_i(abc|r) + B_i(acb|r) \tag{6.3}$$

The functions B take the form of the entries in Table 2.1. As always, the a, b, c label the final state particles and define our phase convention. The momentum

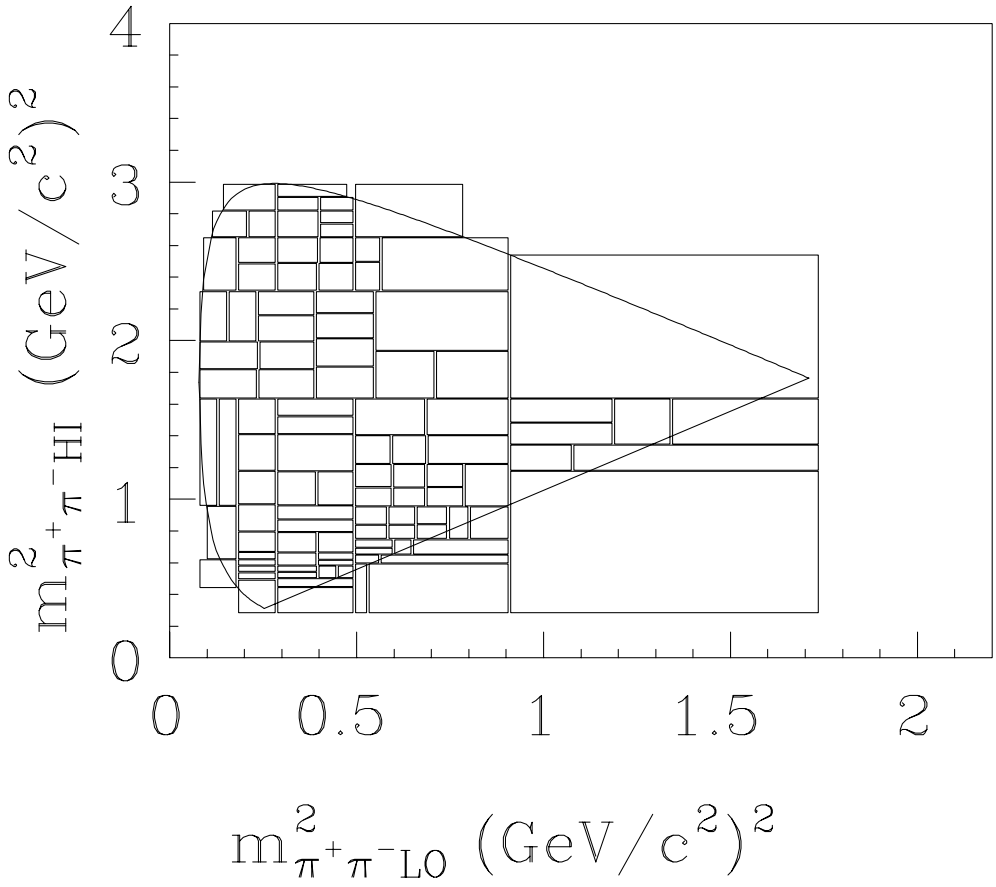

Figure 6.7 Bins resulting from running the adaptive binning algorithm on the high statistics $D^+ \to \pi^+\pi^+\pi^-$ Monte Carlo sample. Within each bin i we calculate the efficiency according to $\epsilon_i = \frac{n^i_{reconstructed\ events}}{n^i_{predicted}}$. We emphasis the binning by suppressing the resulting bin-by-bin efficiency factors from the figure.

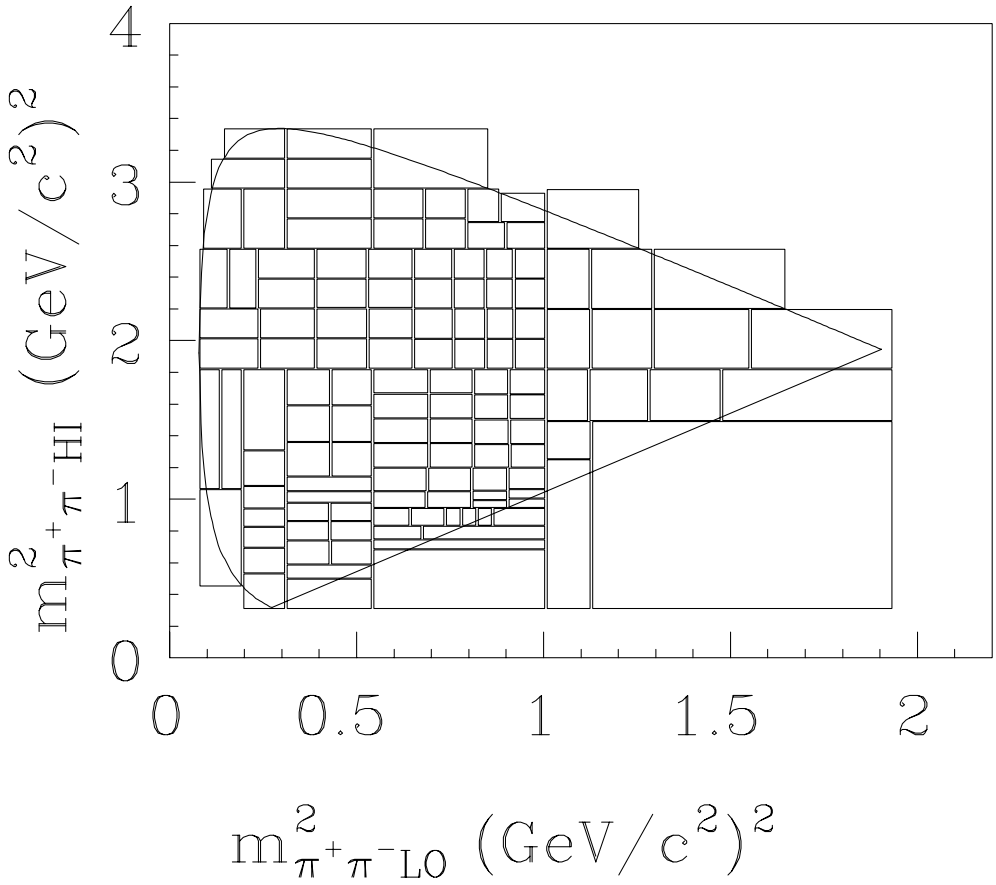

Figure 6.8 Bins resulting from running the adaptive binning algorithm on the high statistics $D_s^+ \to \pi^+\pi^+\pi^-$ Monte Carlo sample.

vectors are in the reference frame of the decaying intermediate resonance. So, according to Eq. 6.3 we write the amplitude for the $f_0\pi^+$ channel as $\mathcal{M}_{f_0\pi^+} = S\left[(\pi^+\pi^-)_{lo}\pi^+\middle|\, f_0\right] + S\left[(\pi^+\pi^-)_{hi}\pi^+\middle|\, f_0\right]$. The remaining amplitudes are similarly constructed.

We perform a continuous likehood fit to the Dalitz plot. The normalized probability density function for the signal is

$$pdf_s = \epsilon\frac{\mathcal{A}_s\mathcal{A}_s^*}{\mathcal{N}_s}$$

where $\mathcal{N}_s$ is the integral across the Dalitz plot of the product $\mathcal{A}_s\mathcal{A}_s^*$. The likelihood function is a continued product (over the signal region events) of the (weighted) sum of the signal and background probability density functions -

$$\mathcal{L}_s = \prod^{sr}\{\mathcal{F}pdf_s + (1-\mathcal{F})pdf_{bg}\}$$

As always, we use MINUIT to minimize the $w = -2\ln\mathcal{L}$ function. It is written as follows -

$$\begin{aligned} w_{signal\ region} &= -2\ln\mathcal{L}_{sr} \\ &= -2\sum_{sr} ln\{\mathcal{F}pdf_s + (1-\mathcal{F})pdf_{bg}\} + \left[\frac{\mathcal{F}-\mathcal{F}_0}{\sigma_{\mathcal{F}_0}}\right]^2 \end{aligned} \tag{6.4}$$

The additional χ^2 term , $\left[\frac{\mathcal{F}-\mathcal{F}_0}{\sigma_{\mathcal{F}_0}}\right]^2$, allows the background normalization to vary within erors. Recall that the background model fit parameters are fixed (i.e., the background is taken to have a purely phase-space distribution), so the function w does not contain a term for varying the background pdf, unlike Eq. 5.11 in Chapter 5.

6.5 Fit Results

The standard amplitude for the D^+ is a coherent sum of nonresonant and $\rho(770)^0\pi^+$ channels whereas the D_s^+ amplitude is written as a sum of nonresonant and $f_0(980)\pi^+$. The resulting fits are shown in Figs. 6.9 and 6.10 and are listed in the following tables.

Table 6.7 D^+ Fit Results

f_{NR}	$0.650 \pm 0.091 \pm 0.0523$
$f_{\rho(770)\pi^+}$	$0.353 \pm 0.091 \pm 0.0518$
δ_{NR}	0.0^o (fixed)
$\delta_{\rho(770)\pi^+}$	$22.8 \pm 12.9 \pm 2.2 \pm 3.8^o$
$-2ln(\mathcal{L})$	157.9
ARGUS conf. level (%)	46.6
χ^2	5.65 (5 DOF)

Table 6.8 D_s^+ Fit Results

f_{NR}	$0.981 \pm 0.144 \pm 0.0896$
$f_{f_0(980)\pi^+}$	$1.241 \pm 0.126 \pm 0.0404$
δ_{NR}	0.0^o (fixed)
$\delta_{f_0(980)\pi^+}$	$84.3 \pm 9.5 \pm 10.6^o$
$-2ln(\mathcal{L})$	108.8
ARGUS conf. level (%)	40.1
χ^2	1.34 (2 DOF)

We note a dramatic difference in the amount of interference found in the decay of the D^+ and D_s^+. The former obtains a decay fraction sum of 1.00 whereas the latter obtains 2.22. The relative simplicity of our $\pi\pi\pi$ fits allows us to easily motivate this observed difference in interference by using analytic arguments. Recalling our informal discussion of decay amplitudes in Sec. 2.2.1, we consider the total decay intensity

$$\begin{aligned} I &= \sum_{i,j} \mathcal{A}_i \mathcal{A}_j^* \\ &= \sum_i |\mathcal{A}_i|^2 + \sum_{i,j \neq i} \mathcal{A}_i \mathcal{A}_j^* \end{aligned} \tag{6.5}$$

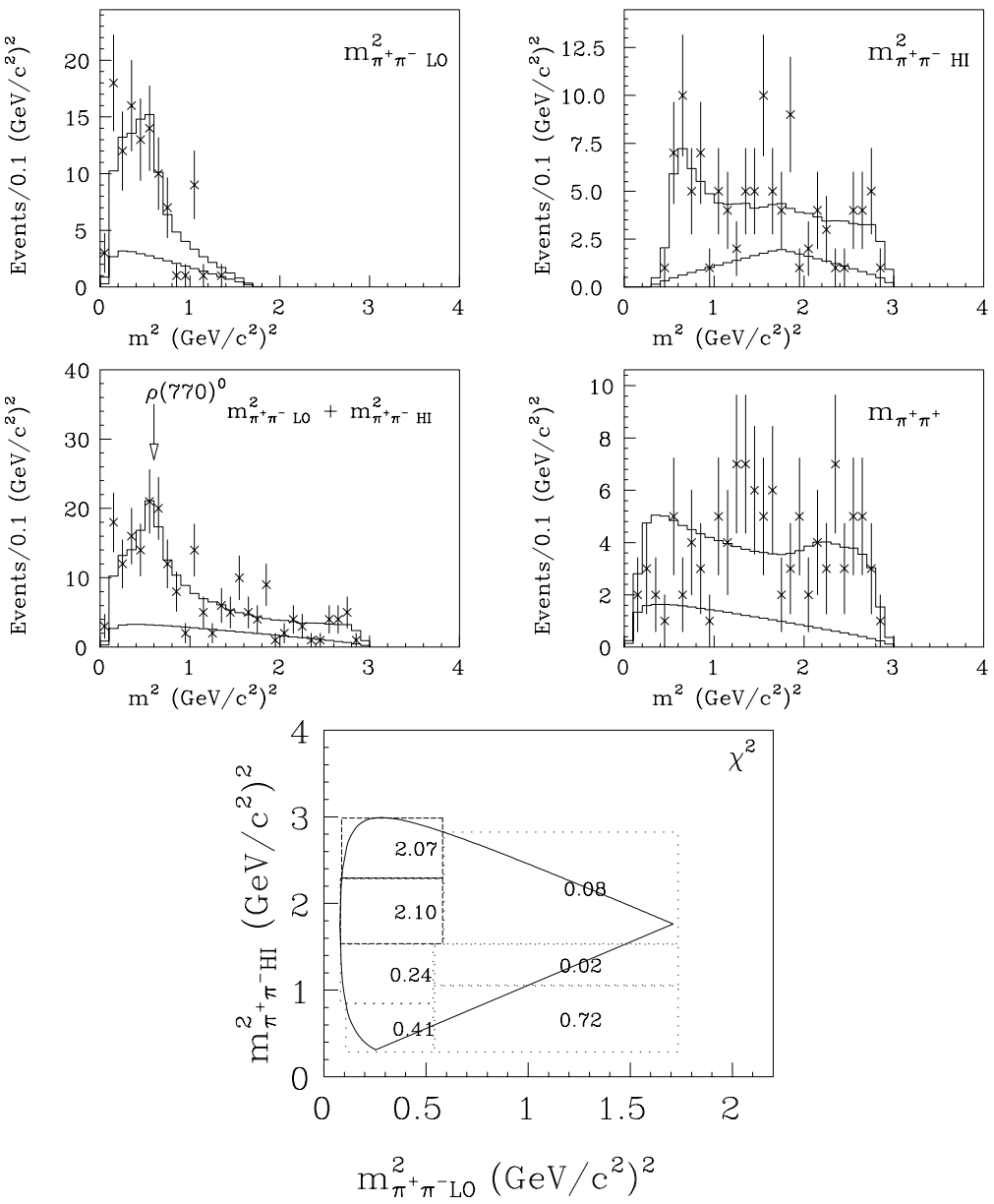

Figure 6.9 Results of the $D^+ \to \pi^+\pi^+\pi^-$ amplitude fit. Mass-squared projections are as indicated. Points with error bars are the data; large histogram is the predicted signal + background; small histogram is the predicted background distribution. All points are singly plotted (as per the prescription of the folded Dalitz plot). Bottom plot shows the adaptive bin-by-bin absolute χ^2 obtained from the fit.

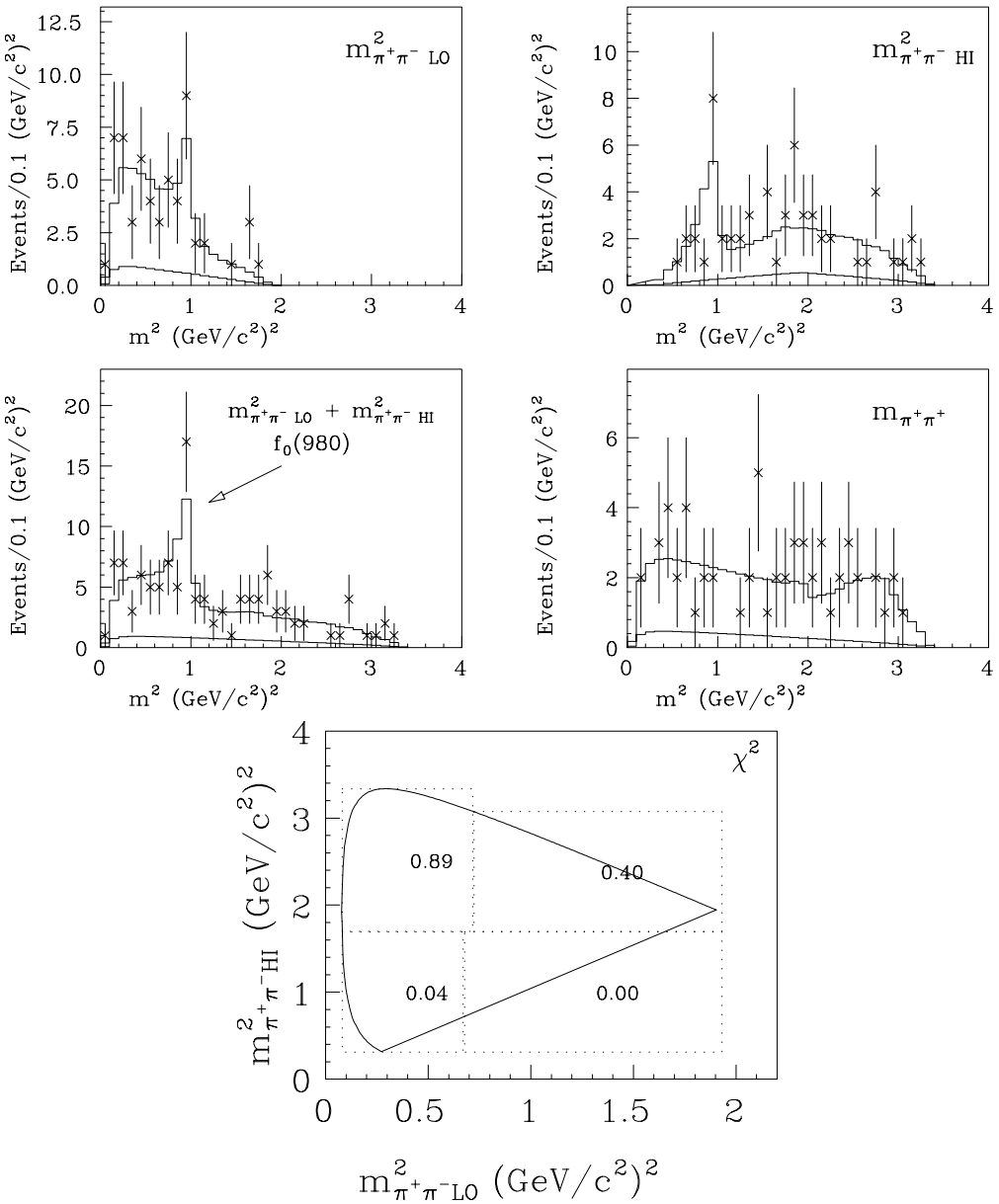

Figure 6.10 Results of the $D_s^+ \to \pi^+\pi^+\pi^-$ amplitude fit. Mass-squared projections are as indicated. Bottom plot shows the adaptive bin-by-bin absolute χ^2 obtained from the fit.

We consider the sign of the interference terms $\sum_{i,j\neq i} \mathcal{A}_i \mathcal{A}_j^*$. Using arguments identical to the example of Sec. 2.2.1, we determine the pattern of interference on the $\pi\pi\pi$ Dalitz plots to be as displayed on Fig. 6.11.[2] Note the tremendous interference detected in the D_s^+ fit.[3] Also note the fitted phase δ_{f_0} is consistent with the case of relatively imaginary (i.e., $\delta \simeq 90^o$) amplitudes, which implies maximal interference. Onn the other hand, the D^+ interference pattern is consistent with the case of relatively real amplitudes.

To estimate the systematic errors, we add in quadrature the "split sample" and the "fit variant" systematic errors, as described in Chap. 5. We divide the data into high ($p > 90 GeV$) and low momentum ($p < 90 GeV$) samples for the former, and use the following fit variants to assess the fit variant systematics: helicity amplitudes, fixing the Blatt-Weiskopf form factors F_D and F_r to unity and letting the background normalization vary without constraint (i.e., $\sigma_{\mathcal{F}} \to \infty$). The largest systematic uncertainty is due to the background level.

The next step is to test the technical correctness of the fit (i.e., "are the statistical errors returned by MINUIT correct, are the fit parameter estimates unbiased ?"). To address these questions we ran mini-Monte Carlo trials consisting of 1000 experiments each containing statistics identical to that in the data (see Table 6.2). We show in Figure 6.12 (D^+) and 6.13 (D_s) the deviations of the fit parameters obtained from fitting each of these samples. To the extent these plots are unbiased (i.e., mean consistent with 0) and have widths comparable to the statistical error returned by MINUIT, the fit is technically correct. In both cases the decay fractions are fairly unbiased and the returned estimators have widths commeasurate with the statistical errors returned by the fit. Contrary to our finding of negligible bias (due to mass resolution effects) in the phases δ in Sec. 6.3, significant biases are observed for the two phases.

---

2 In the figure, we disregard complications due to the folded Dalitz boundary.

3 The D_s and D^+ decay fractions sum to 2.22 and 1.00, respectively.

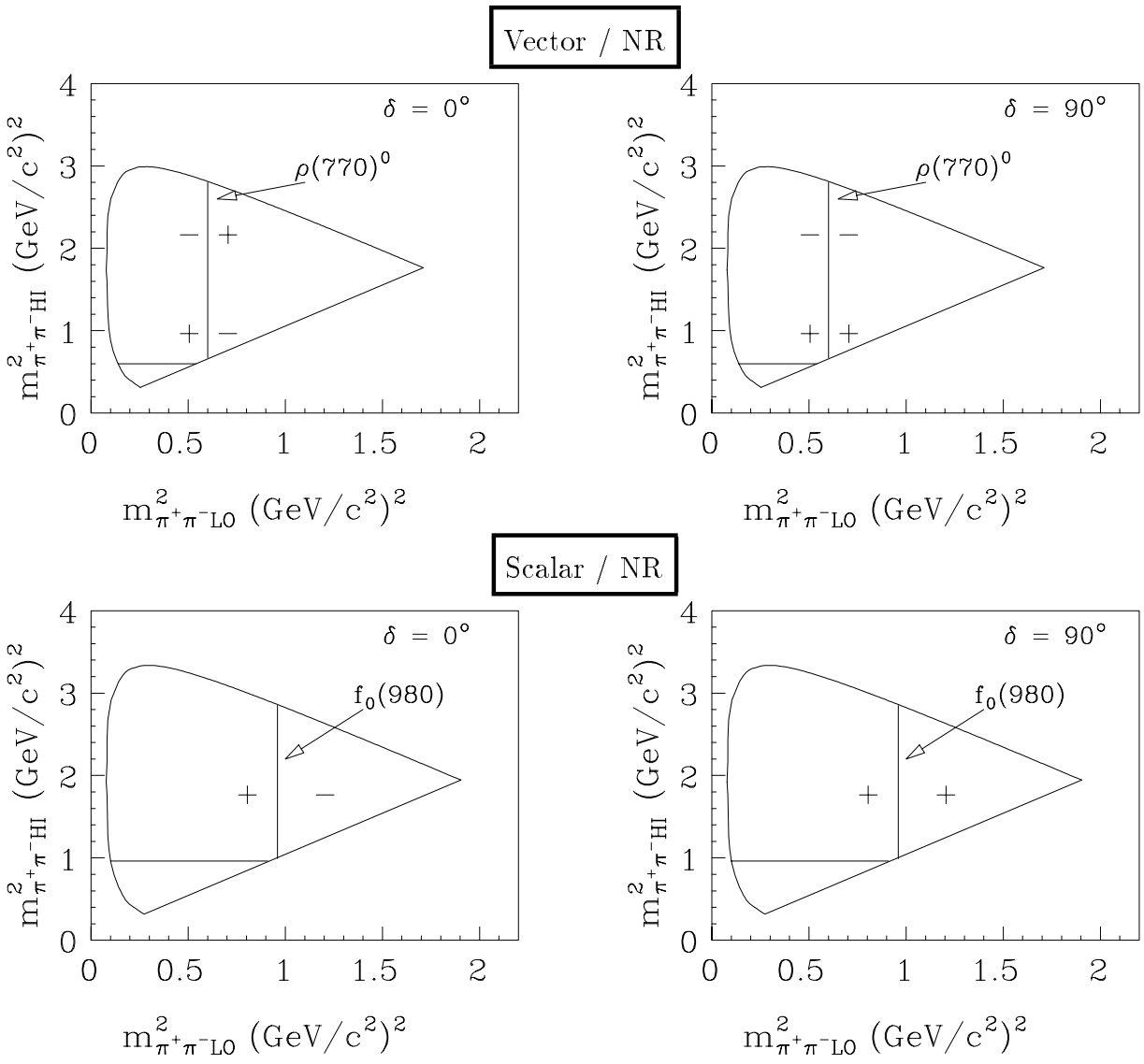

Figure 6.11 Sign of the interference terms in Eq. 6.5 for the D^+ (top row) and D_s^+ (bottom row) decays to $\pi^+\pi^+\pi^-$. For the D_s decay, relatively real ($\delta = 0^0$) amplitudes contribute zero net interference, relatively imaginary amplitudes contribute large amounts of inteference to the intensity function. Similarly, $\delta = 0^o$ and $\delta = 90^o$ correspond to zero and maximal net interfernce, respectively, for the $D^+ \to \pi^+\pi^+\pi^-$ fit. For the ρ, the total interference cancels independent of the fitted phase but the pattern of interference is sensitive to whether the phase is real (i.e., $\delta \simeq 0^o$) or imaginary (i.e., $\delta \simeq 90^o$).

These results are summarized in Tables 6.9 and 6.10.[4]

Table 6.9 D^+ Mini-Monte Carlo Checks

Parameter	σ_{MMC}	σ_{fitter}	Bias
$\delta_{\rho\pi+}$	13.4^o	12.9^o	1.17
f_{NR}	0.084	0.091	-0.11
$f_{\rho\pi+}$	0.085	0.091	0.10

Table 6.10 D_s^+ Mini-Monte Carlo Checks

Parameter	σ_{MMC}	σ_{fitter}	Bias
$\delta_{f_0\pi+}$	8.1^o	9.5^0	1.22
f_{NR}	0.151	0.144	-0.03
$f_{f_0\pi+}$	0.122	0.126	-0.25

We next employ likelihood confidence levels and adaptive two-dimensional χ^2 tests to assess the ability of the fitter to mimic the data. The likelihood confidence levels are 52% and 61% for the D^+ and D_s, respectively. The bin-by-bin contributions to the two-dimensional χ^2 are shown in Figures 6.14 and 6.15. Although the biggest χ^2 bin contribution implies only about a 1.5 standard deviation discrepancy. we find it disconcerting that the biggest discrepancies are in the region of the D^+ ρ band close to the $\rho's$ Zemach zero. In light of the weak visual evidence of the ρ Zemach structure in the Dalitz plot (*i.e.* it's "filled in" in the data) this discrepancy is not surprising. This mismatch between the fit prediction and the data probably means, once again, that our model is over simplified. The χ^2 values are listed in Tables 6.7 and 6.8. In Chapter 5 we discussed the fact that the χ^2 distributions for the binned Dalitz plots do not strictly follow the χ^2 distributions expected for a fit with a degrees of freedom equal to number of bins minus the number of fit parameters because the fit is

4 We define the bias for fit parameter i as the normalized deviation from zero, $\frac{\alpha_{i,fit} - \alpha_{i,parent}}{\sigma_{i,parent}}$.

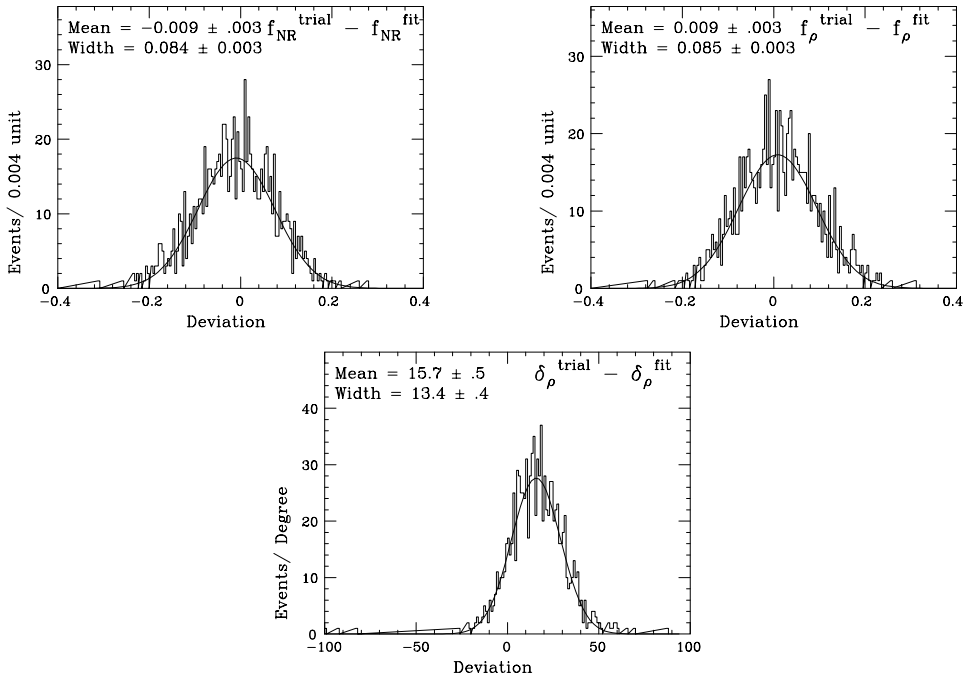

Figure 6.12 Mini-Monte Carlo tests on the $D^+ \to \pi^+\pi^+\pi^-$ fit.

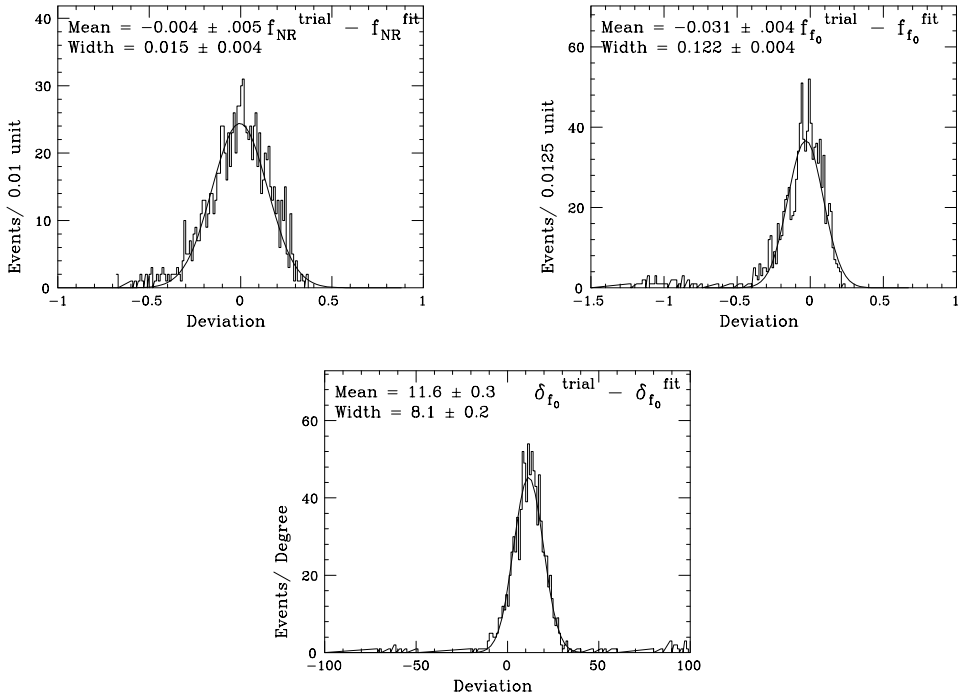

Figure 6.13 Mini-Monte Carlo tests on the $D_s^+ \to \pi^+\pi^+\pi^-$ fit.

minimizing the log likelihood rather than the binned χ^2 test statistic. If one naively computes the confidence level using this erroneous degree of freedom, we obtain confidence levels of 34% and 52% for the D^+ and D_s^+ respectively, which suggests that the fits are quite consistent with the data. Because we have undercounted the degrees of freedom, the true confidence levels are probably higher.

6.6 Branching Fractions

We extract ratios of partial widths in a manner identical to the procedure described in Chap. 5. Our results are listed below in the table. Basically, our D_s^+ results are consistent with E691.

Table 6.11 Ratios of Partial Widths

	this work	E691
$\frac{\Gamma(D^+ \to \rho^0 \pi^+)}{\Gamma(D^+ \to \pi^+\pi^+\pi^-_{NR})}$	$0.543 \pm 0.159 \pm 0.091$	-
$\frac{\Gamma(D_s^+ \to f_0(980)\pi^+)}{\Gamma(D_s^+ \to \pi^+\pi^+\pi^-_{NR})}$	$1.215 \pm 0.216 \pm 0.118$	$0.966 \pm 0.457 \pm 0.144$

6.7 Closing Remarks

We have presented fits to the amplitudes for the nonleptonic decays $D^+, D_s^+ \to \pi^+\pi^-\pi^+$. We found evidence for three-body nonreasonant decay in both amplitudes and $\rho\pi^+$ and $f_0\pi^+$ in the D^+ and D_s^+, respectively. Although we find a substantial nonresonant contribution in our model, we cannot prove that this contribution is purely nonresonant, *i.e.* it may be a mixture of several broad resonances which can mimic a nonresonant contribution.

Chapter 7

Conclusion

We have reported Dalitz amplitude analysis of nonleptonic decays of the D^+ and D_s^+ mesons to the $K^+K^-\pi^+$ and $\pi^+\pi^+\pi^-$ final states. We obtained fit amplitudes and phases. We extracted decay fractions and ratios of partial widths from our fit results. Unlike many previous studies of these decays, our "charm interferometry" technique properly accounts for quantum mechanical interference, thereby allowing us to discover previously unknown $KK\pi$ decay channels.

The $KK\pi$ Dalitz plots described in Chapter 5 were excellent laboratories for studying these interference effects. Although the Dalitz scatterplots in Fig. 5.2 seemed to be dominated by the $\phi\pi^+$ and $\overline{K}^*(892)^0K^+$ channels, considerable interference[1] was found (see Table 5.17). The asymmetric intensity of the ϕ lobes in the D^+ scatterplot[2] betrayed the notable interference between the $\overline{K}^*(892)^0$ and $\overline{K}^*(1430)^0$ resonances. In fact, we found a sizable relative fitted phase δ[3] between these channels, indicating significant final state interactions between them. Another D^+ decay analysis [17] found a large $\overline{K}^*(1430)^0\pi^+$ decay fraction (0.284 ± 0.063) in $D^+ \to K^-\pi^+\pi^+$. Our statistical tests (two-dimensional χ^2) as well as compelling visual evidence in the mass-squared projections led us to write the D^+ amplitude as a three-channel process and the D_s^+ as a five-channel decay.[4] By obtaining the full quantum mechanical decay amplitude and efficiency correction function over the entire space of physical observables, we were able to extract high precision ratios of partial widths for the landmark D^+ decays. The branching fractions reported in Table 5.19 tend to be somewhat lower than previous measurements. This might reflect the fact that our fits are fully coherant for this state while other group's are not.

---

1 The D^+ decay fractions sum to 96%, the D_s^+ to 111%.

2 Recall lobes L_1, L_2 in Fig. 5.14.

3 Which also happened to be consistent with 90^o at the 2.5 standard deviation level.

4 There has been recent speculation [28] that two of the resonances which participate in the $D_s^+ \to K^+K^-\pi^+$ decay, the $f_0(980)$ and $f_J(1710)$, are candidate non $-$ quark $\overline{\text{quark}}$ states, possibly glueballs or $K\overline{K}$ molecules.

Although the sample sizes were small, our $\pi^+\pi^+\pi^-$ analysis identified two channels in each decay. The large nonresonant fractions reported in Tables 6.7 and 6.8 were probably low statistics manifestations of more complicated resonant substructure. On the other hand, the simplicity of our fits allows us to cleanly identify FSI effects. The $\rho\pi^+$ and nonresonant D^+ channels had no net FSI whereas the D_s channels had essentially maximal interaction. Our branching fractions were consistent with E691's [22] measurements.

It is hoped that future Dalitz analyses based on more sophisticated decay models and employing larger data samples will shed more light on this fascinating subject.

Appendix A

The Helicity Formalism

We presently describe the helicity amplitude formalism for describing decay amplitudes. The helicity h is defined by $\vec{S} \cdot \hat{p}$. It is well suited for relativistic processes because one can construct relativistic basis vectors that are either eigenstates of total angular momentum and helicity, or of linear momentum and helicity.

Within the helicity formalism [40] we consider the two body decay $D \to rc$, where particle D has angular momentum J, angular momentum component M along the (arbitrary) quantization axis Z (see Fig. A.1), and the two daughter particles have spin components (*i.e.*, helicity) λ_r and λ_c along the decay axis Z'. We write the parent state (in the familiar Dirac bra notation) as $|JM\rangle\,|P^\alpha\rangle$. In

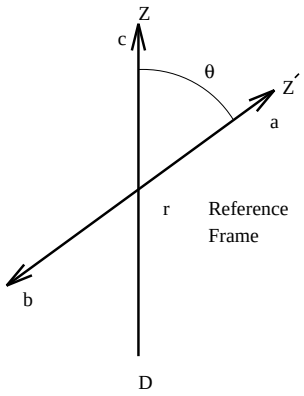

Figure A.1 Coordinate system for the decay $D \to rc \to (ab)c$. The arrows represent 3-momentum vectors of the particles in the rest frame of the intermediate resonance r.

this notation we have employed the fact that the parent state is explicitly an eigenstate of the four-momentum P^α. This observation allows one to factorize the state vector into angular momentum and four-momentum parts. Likewise, in the so-called two-particle *plane-wave helicity basis*, the final state is written $\left|p_f, \theta_f, \phi_f, \lambda_1, \lambda_2\right\rangle |P^\alpha\rangle$. Here, the decay axis Z' has polar angles θ_f and ϕ_f with

respect to the quantization axis Z of the decaying D. The amplitude for the process $D \to rc$ is written

$$\mathcal{M} = (2\pi)^3 \left[\frac{4m_D}{p_f}\right]^{\frac{1}{2}} \left\langle \theta_f \phi_f \lambda_1 \lambda_2 \right| U \left| JM \right\rangle \tag{A.1}$$

U is the time evolution operator that propagates the initial state to the final state. The factors preceding the transition matrix element $\left\langle \theta_f \phi_f \lambda_r \lambda_c \right| U \left| JM \right\rangle$ in Equation A.1 are due to the normalization condition which holds for the two-particle plane-wave helicity basis kets:

$$\begin{aligned} \left\langle \theta' \phi' \lambda' \lambda' | \theta \phi \lambda_r \lambda_c \right\rangle &= (2\pi)^6 \frac{4\sqrt{s}}{p} \delta^4 \left(P'^{\alpha} - P^{\alpha}\right) \delta\left(\cos\theta' - \cos\theta\right) \\ &\times \delta\left(\phi' - \phi\right) \delta_{\lambda'_r, \lambda_r} \delta_{\lambda'_c, \lambda_c} \end{aligned} \tag{A.2}$$

To apply conservation of angular momentum to the transition matrix element $\left\langle \theta_f \phi_f \lambda_1 \lambda_2 \right| U \left| JM \right\rangle$, it is necessary to use eigenstates of total angular momentum as the basis of the two-particle center-of-momentum states. To this end we make a change of basis from the two-particle plane-wave helicity basis to the so called *spherical helicity basis* $\{|JM\lambda_r\lambda_c\rangle\}$ according to the following rule -

$$\left\langle JM\lambda'_r\lambda'_c | \theta\phi\lambda_r\lambda_c \right\rangle = \delta_{\lambda'_r,\lambda_r}\delta_{\lambda'_c,\lambda_c}\sqrt{\frac{2J+1}{4\pi}} D^J_{M\lambda}(\phi,\theta,-\phi) \tag{A.3}$$

The next step is to insert a complete set of spherical helicity basis kets into equation A.1. Unfortunately, at this point the literature is confusing - the crucial momentum normaliztion fators $\frac{4\sqrt{s}}{p}$ are ignored [40- 42]. Upon dropping the momentum dependence the decay amplitude becomes

$$\mathcal{A}(D \to rc) = \left[\frac{2J+1}{4\pi}\right]^{\frac{1}{2}} D^{J*}_{M\lambda}(\phi_f, \theta_f, -\phi_f) A_{\lambda_r \lambda_c} \tag{A.4}$$

In these equations, $\lambda = \lambda_r - \lambda_c$ and $p_f = |\vec{p}_r| = |\vec{p}_c|$ in the center of momentum frame. The term $A_{\lambda_r\lambda_c}$ is the matrix element $\langle \lambda_r \lambda_c | U | M \rangle$. Since it must be rotationally invariant, we write simply $A_{\lambda_r\lambda_c}$, a notation that explicitly neglects the

M quantum number. It is straightforward to extend this result to the sequential two-body decay, $D \to rc \to (ab)c$ that is the subject of this thesis. Again, dropping the momentum normalization factors obtains

$$\begin{aligned} \mathcal{A}(D \to rc \to (ab)c) &= \sum_{\lambda_r} D^{s_r *}_{\lambda_r, \lambda_a - \lambda_b}(\phi_a, \theta_a, -\phi_a) D^{J*}_{M, \lambda_r - \lambda_c}(\phi_r, \theta_r, -\phi_r) \\ &\times B_{\lambda_a, \lambda_b} A_{\lambda_r \lambda_c} BW(m_r) \end{aligned} \tag{A.5}$$

Here we have summed over the allowed helicities of the intermediate particle r because it cannot be measured. The function BW is a Breit-Wigner propagator which represents the strong interaction dynamics of the intermediate resonance r. It is the same Breit-Wigner propagator used in the Zemach formalism described in Sec. 2.2.2. It takes the form

$$\frac{1}{m_0^2 - m_{ab}^2 - i\Gamma m_0}$$

The angles θ_r, ϕ_r are measured in the rest frame of the decaying parent D, whereas the angles θ_a, ϕ_a are measured in the rest frame of the intermediate resonance r.

One might ask, 'why are we spending so much time describing the helicity amplitude formalism, especially since our analysis is based on the Zemach (following section) formalism?' The answer is we must have an alternative amplitude formalism to assess systematic effects due to the details of our model. We will compare our standard results (obtained within yje Zemach amplitude formalism) to results obtained within the helicity framework. In order to affect this comparison, we have to decide how to accomodate the missing momentum factors in the helicity formalism. We adopt the expedient step employed by the MARK III [6] Collaboration - the momentum dependence is 'put in by hand' by placing a factor $\sqrt{\frac{\Gamma m_r}{p_{ab}}}$ in front of the amplitude in Eq. A.5. The result is to obtain the amplitudes listed in Table A.1 below.

A.1 Helicity Amplitudes

$J(r)$	$\mathcal{M}$
nonresonant	1
0	$y \times \sqrt{\frac{\Gamma m_r}{p_{ab}}} BW$
1	$y \times \sqrt{\frac{\Gamma m_r}{p_{ab}}} \left[-2\lvert\vec{C}\rvert \ \lvert\vec{A}\rvert \ \cos\theta^R_{AC}\right] \times BW$
2	$y \times \sqrt{\frac{\Gamma m_r}{p_{ab}}} \left[(-2\lvert\vec{C}\rvert \ \lvert\vec{A}\rvert)^2 \frac{1}{2}(3\cos^2\theta^R_{AC} - 1)\right] \times BW$
3	$y \times \sqrt{\frac{\Gamma m_r}{p_{ab}}} \left[(-2\lvert\vec{C}\rvert \ \lvert\vec{A}\rvert)^3 \frac{1}{2}(5\cos^3\theta^R_{AC} - 3\cos\theta^R_{AC})\right] \times BW$

The factor y is a product of the hadronic vertex form factors F_D and F_r which are described in Sec. 2.2.2.

Appendix B

Notes on the Estimation of Branching Fraction Errors

There is a subtle issue concerning the propagation of errors for the various quantities in Eqn. 5.30 due to the fact that there is a potential correlation between $\Gamma(K^+K^-\pi^+)$ and $f(D \to \phi\pi)$. To illustrate this let's consider the slightly simpler problem of estimating the branching ratio of $D^+ \to \phi\pi$ relative to $K^-\pi^+\pi^+$

$$BR(D^+ \to \phi\pi^+) = \frac{\Gamma(D^+ \to K^+K^-\pi^+)}{\Gamma(D^+ \to K^-\pi^+\pi^+)} \times \frac{f(D^+ \to \phi\pi)}{B(\phi \to K^+K^-)}. \qquad (B.2)$$

Rather than quoting the factor $\frac{\Gamma(D^+\to K^+K^-\pi^+)}{\Gamma(D^+\to K^-\pi^+\pi^+)}$ from the literature, we measure it in our data. Specifically, $\frac{\Gamma(D^+\to K^+K^-\pi^+)}{\Gamma(D^+\to K^-\pi^+\pi^+)} = \frac{N(KK\pi)/\hat{\epsilon}(KK\pi)}{N(K\pi\pi)/\hat{\epsilon}(K\pi\pi)}$. The overall $KK\pi$ reconstruction efficiency $\hat{\epsilon}(KK\pi)$[1] ,is obtained from a Lund /Rogue Monte Carlo phase-space simulation where we reject on the D^+ decay amplitude in Table 5.17. Likewise, the $\hat{\epsilon}(K\pi\pi)$ is obtained by rejecting phase space with our published [17] $D^+ \to K^-\pi^+\pi^+$ amplitude. The potential correlation we are concerned with comes about since an upward fluctuation in the $KK\pi$ yield will increase both the perceived $\Gamma(KK\pi)$ and the signal fraction $\mathcal{F}$ used in obtaining our likelihood. This correlation will in turn induce a correlation in the fit fraction $f(\phi\pi)$.

In this section we compute this correlation using the mini-Monte Carlo techique and will show that it can be neglected. We find that the error is well estimated by neglecting the off-diagonal elements of the covariance matrix for the factors in Eq. B.2 and just simply taking a quadrature sum of terms. It is more transparent to write $\frac{\Gamma(D^+\to K^+K^-\pi^+)}{\Gamma(D^+\to K^-\pi^+\pi^+)}$ as $\frac{\Gamma(D^+\to K^+K^-\pi^+)}{\Gamma(D^+\to K^-\pi^+\pi^+)} = \frac{N(KK\pi)_{corr}}{N(K\pi\pi)_{corr}}$, where N_{corr} is the efficiency corrected yield. So the branching ratio expression,

1 This is not to be confused with the efficiency function $\epsilon(m^2_{KK}, m^2_{K^-\pi^+})$ used in the amplitude fit.

Eq. B.2, becomes

$$BR(D^+ \to \phi\pi^+) = \frac{N(KK\pi)_{corr}}{N(K\pi\pi)_{corr}} \times \frac{f(D^+ \to \phi\pi)}{B(\phi \to K^+K^-)} \qquad (B.3)$$

Note this equation is just products and quotients of the quatities Q_i. Now, the propagation of error formula

$$\sigma^2(BR) = \frac{\partial BR}{\partial Q_i} < \delta Q_i, \delta Q_j > \frac{\partial BR}{\partial Q_j}$$

obtains for the fractional error on this branching ratio

$$\frac{\sigma^2(BR)}{BR^2} = \sum_i \frac{\sigma^2(Q_i)}{Q_i^2} + 2 \sum_{i,j;\ j>i} \frac{\sigma(Q_i)}{Q_i} \frac{\sigma(Q_j)}{Q_j} sign_i\ sign_j\ \rho(i,j) \qquad (B.4).$$

In this formula, $sign_i$ is $+1$ if Q_i appears in the numerator in equation B.4, -1 otherwise. $\rho(i,j)$ is the correlation coefficient between the quantities Q_i and Q_j - it ranges from -1 to +1, inclusive.[2] The dominant errors are likely to be on $N(KK\pi)_{corr}$ and the $\phi\pi^+$ fit fraction, which are both in the numerator and thus have $sign = +1$. In this case, we have a simple geometrical interpretation. The fractional error $\sigma(BR)/BR$ is the vector sum of fractional errors $\sigma(KK\pi)/N(KK\pi)_{corr}$ and $\sigma(f(\phi\pi^+))/f(\phi\pi^+)$, where $\sigma(KK\pi)/N(KK\pi)_{corr}$ is inclined with respect to $\sigma(f(\phi\pi^+))/f(\phi\pi^+)$ by an angle whose cosine is $\rho(f(\phi\pi^+), N(KK\pi)_{corr})$. For simplicty, we can think

2 The correlation coefficient ρ, $\frac{<\delta Q_i, \delta Q_j>}{\sigma(Q_i)\sigma(Q_j)}$, is useful because it sets a natural scale for the covariance between quantities Q_i, Q_j. It can be shown that when $|\rho| > 1$, the covariance matrix is not positive definite.

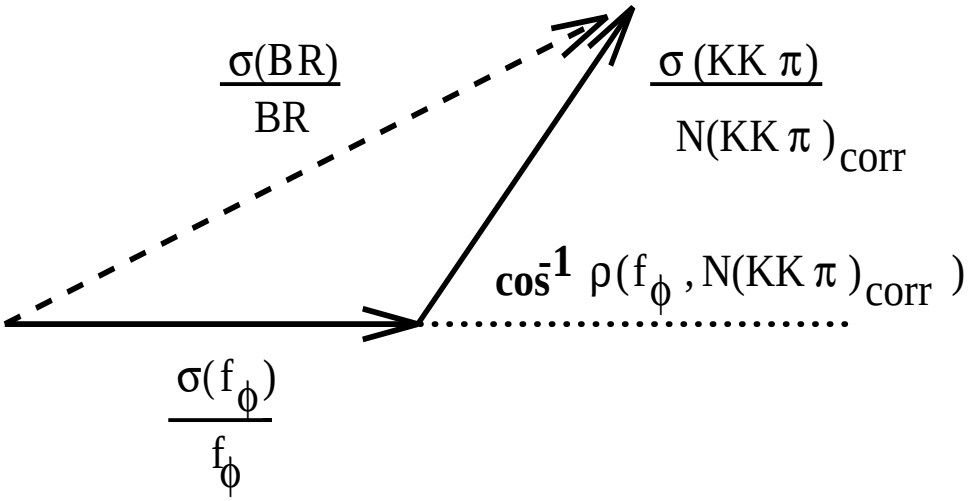

Figure B.1 Geometrical interpretation of the correlation coefficient.

of $\sigma(KK\pi)/N(KK\pi)_{corr}$ as the fractional error in the number of $KK\pi$ events which appears in the signal peak. If $\rho(f(\phi\pi^+), N(KK\pi)_{corr})$ is zero, the fractional errors are at right angles and one adds them in quadrature to get the fractional error in the BR. We plot $\frac{\sigma(BR)}{BR}$ from equation B.4 in Fig. B.2. We used the quantities and statistical errors quoted in the Table 5.17. We assumed the correlation coefficient matrix had $+1.$ along the diagonal and just varied $\rho(f, N_{corr}(KK\pi))$ (and $\rho(N_{corr}(KK\pi), f)$) from $-1.$ to $+1.$ From these plots it is apparent that if we can establish that $\rho(f, N_{corr}(KK\pi))$ is close to zero the calculation of the error on the branching ratio is well approximated by the quadrature sum

$$\sigma^2(BR) = \sum_i \frac{\partial BR}{\partial Q_i}^2 \sigma_i^2.$$

It follows that the error in our quoted ratios of partial widths in Table 5.19 can also be approximated by a quadrature sum of terms.

To compute $\rho(f(\phi\pi), N_{corr}(KK\pi))$ we need to simulate the background subtraction process used to extract the $KK\pi$ yield , the signal fraction , and the effects of a signal fraction fluctuation on the measurement of the $\phi\pi$ decay fraction. To do this we will have to define **parent distribution quantities**, **measured**

quantities and **estimated quantities**. We presently describe our Monte Carlo simulation procedure.

As a simplification , we consider simulating independent yields for the signal region signal (S), the signal region background (B) , the low sideband (A) and the high sideband (C). The schematic (parent) histogram is

$$\begin{array}{ccc} & S & \\ A & B & C \end{array}$$

We choose $A = B = C$ and choose S to be the real signal region signal and B to be the real signal region background. These are **parent distribution** quantities. In the limit $N \to \infty$ (where Poisson $\to$ Gaussian) the yield simulation is essentially independent Gaussians described by

$$S \pm \sqrt{S} \quad A \pm \sqrt{A} \quad B \pm \sqrt{B} \quad C \pm \sqrt{C}$$

On a given trial the **measured yields** S^*, A^*, B^*, C^* are generated by simulating Gaussian random numbers with indicated means and rms spreads. By "measured" we mean these yields are obtained from counting events in a given mass region. Let us denote estimated (fitted) values with a $\tilde{}$. These values are obtained from a Gaussian + polynomial fit to the $KK\pi$ mass histogram.[3] For each trial we can estimate B (of the parent distribution) from the weighted sum of A and C. Let R be the sideband weight (for example, $R = 1/2$ if $A = B = C$). The estimate of B is then

$$\tilde{B} = R(A^* + C^*)$$

The estimate of S for each trial is then:

$$\tilde{S} = S^* + B^* - R(A^* + C^*)$$

3 The estimated fit fractions $\tilde{f}$ are obtained from the full Dalitz fit.

The *a priori* rms error on $\tilde{S}$ is

$$\sigma(\tilde{S}) = \sqrt{S + B + R^2(A + C)} = \sqrt{S + B(1 + R)}$$

The estimate of the signal fraction ($\tilde{\mathcal{F}}$) for each trial is

$$\tilde{\mathcal{F}} = \frac{(S^* + B^*) - R(A^* + C^*)}{S^* + B^*}$$

This trial signal fraction $\tilde{\mathcal{F}}$ goes directly into the Dalitz fitter as the starting point for the solution of the signal fraction. The assumed error on the signal fraction is the same one used in the real Dalitz fits[4] . Once B^* and S^* yields are randomly drawn for the given trial we then randomly populate the signal region Dalitz plot to be fit with B^* events drawn from the parameterized parent background distribution (polynomial) and S^* events with the Dalitz intensity. Specifically, the background and signal parent probability density functions are those used in the final Dalitz fit. One completes the fit to obtain the trial's estimated fit fraction and its estimated error: $\tilde{f} \pm \sigma(\tilde{f})$.

The correlation coefficient,$\rho(f(\phi), N(KK\pi)_{corr})$, is the average over many trials of the quantity

$$\frac{(\tilde{f}(\phi) - f(\phi))(\tilde{S} - S)}{\sigma(\tilde{f}(\phi))\sigma(\tilde{S})} \qquad (B.5).$$

We take the $\sigma(\tilde{f}(\phi))$ to be the fit fraction error returned for each trial fit. For expediency, we use the a priori error on $\sigma(\tilde{S})$ ($\sqrt{S + B(1 + R)}$). We histogram this quantity for each trial and find the typical or mean value of ρ from the histogram.

For our mini-Monte Carlo simulation we use the following parent distribution quantities:

4 $\sigma_{\mathcal{F}_0}$ in Table 5.1.

Table B.1 D^+ Parent Distribution Quantities

Signal region signal S	915
Sideband population:A,B,C	318

In Fig. B.3 we plot the expectation value of B.5 for the landmark decay channels we used for the D^+ fit. We also show the value of $\frac{\sigma(BR_X)}{BR_X}$ from Fig. B.2 corresponding to this correlation coefficient and for zero correlation.

Table B.2 $< \rho >$

Channel	$< \rho(f, N(KK\pi)_{corr}) >$	$\frac{\sigma(BR_X)}{BR_X}$	$\frac{\sigma(BR_X)}{BR_X}\Big\vert_{\rho=0}$
K^*K	+0.008	0.075	0.08
$\phi\pi$	+0.036	0.094	0.118

Given that $\frac{\sigma(BR_X)}{BR_X} \simeq \frac{\sigma(BR_X)}{BR_X}_{\rho=0}$, it is appripriate to approximate the branching ratio error with quadrature sums of the contributing errors. It follows that little accuracy is lost by using quadrature sums of the participating terms to calculate the errors of the ratios of partial widths in Table 5.19.

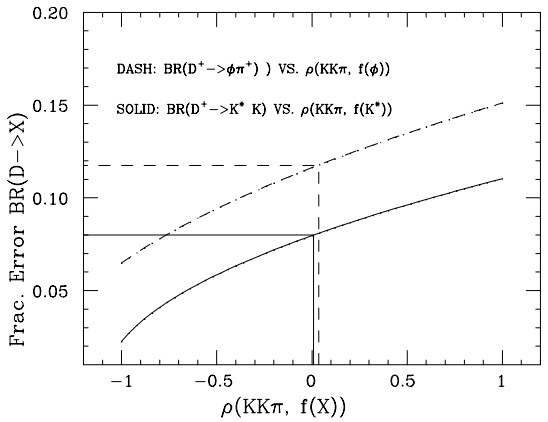

Figure B.2 Branching fraction correlation coefficient study. Curves are plots of Eq. B.4. Lines show the result of a Mini-Monte Carlo study of $< \rho >$ and indicate the corresponding fractional error in BR.

Appendix C

The Parameterization of the $f_0(980)$ Resonance

Because the literature is filled with many different parameterizations of the $f_0(980)$ resonance, an essential first step for our Dalitz analysis is to decide what impact our chosen f_0 model has on our amplitude fit. In an effort to understand the impact of our parameterization on the $KK\pi$ analysis, we tried fully coherent Dalitz plot fits using the $\phi\pi^+, \overline{K}^*(892)^0 K^+$ and $f_0(980)\pi^+$ amplitudes. The f_0 parameterizations we tried are listed in Tables C.1 and C.2.

Table C.1 $f_0(980)$ Amplitudes

Type	$\mathcal{M}_{f_0(980)}$	$m_0\ (GeV)$	g_π	g_K
WA76 [43]	$\frac{1}{m_0^2 - m_{KK}^2 - i m_0(\Gamma_\pi + \Gamma_K)}$	.979	$.28 \pm .04$	$.56 \pm .18$
Mark II [44]	$\frac{1}{m_0^2 - m_{KK}^2 - i m_0(\Gamma_\pi + \Gamma_K)}$	.956	.088	.2
Rutherford [45]	$\frac{1}{m_0^2 - m_{KK}^2 - i\frac{m_0}{2}(\Gamma_\pi + \Gamma_K)}$	.987	1.	3.8
LEBC [46]	$\frac{1}{m_0^2 - m_{KK}^2 - i m_0 \Gamma_K}$	.971	-	-
Zou [47]	$\frac{g_K}{m_0^2 - m_{KK}^2 - i m_0(\rho_\pi g_\pi + \rho_K g_K)}$	.9535	$.1108\ GeV^2$	$.4229\ GeV^2$

Table C.2 Terms in the $f_0(980)$ Amplitudes

Type	Γ_π	Γ_K	ρ_π	ρ_K
WA76	$g_\pi \sqrt{\frac{m_{KK}^2}{4} - m_\pi^2}$	$\frac{g_K}{2}\left[\sqrt{\frac{m_{KK}^2}{4} - m_{K^+}^2} + \sqrt{\frac{m_{KK}^2}{4} - m_{K^0}^2}\right]$	-	-
Mark II	$g_\pi \sqrt{\frac{m_{KK}^2}{4} - m_\pi^2}$	$g_K \sqrt{\frac{m_{KK}^2}{4} - m_{K^+}^2}$	-	-
Ruth.	$g_\pi \sqrt{\frac{m_{KK}^2}{4} - m_\pi^2}$	$g_K\left[\sqrt{\frac{m_{KK}^2}{4} - m_{K^+}^2} + \sqrt{\frac{m_{KK}^2}{4} - m_{K^0}^2}\right]$	-	-
LEBC	-	$\Gamma_0 \frac{m_0}{m_{KK}} \frac{p^*}{p_0^*}$	-	-
Zou	-	-	$\sqrt{1 - \frac{4m_\pi^2}{m_{KK}^2}}$	$\sqrt{1 - \frac{4m_K^2}{m_{KK}^2}}$

All the amplitudes have similar forms. m_0 is the on-shell mass and the remaining constants appear as listed in the formulas. Note that because the

kinematic boundary of the $KK\pi$ Dalitz plot requires $m^2_{KK} \geq [2 \times m_{K^+}]^2$, the WA76, Mark II, Rutherford and Zou amplitudes are analytic in all regions of the Dalitz boundary. Only resolution effects might put a datum in the dreaded 'subthresold region.' However, the LEBC model (with $\Gamma_0 = .0374GeV$) explicitly contains p_0^*, the 3-momentum of the $f_0(980)$ daughters in the $f_0(980)$ rest frame when $m_{KK} = m_0$. In this region, p_0^* is the square root of a negative number $\left(= \sqrt{\frac{m^2_{f_0(980)}}{4} - m^2_{K^+}}\right)$. To get around this explicit reference to the 'subthreshold region' we take p_0^* to be $+\sqrt{|\frac{m^2_{f_0(980)}}{4} - m^2_{K^+}|}$.

We show the simulated scatterplots for these pure $f_0(980)$'s (on the D_s kinematic boundary) in Figure C.1. The most dramatic difference is evidenced by the extent of the Breit-Wigner tails in the K^+K^- direction.

We ran fits to the data with the background amplitudes and signal fraction $\mathcal{F}$ fixed to their initial values. The spread in fit fraction and phase are shown in Figure C.2. The fits '$WA76 + 1, 2\sigma$' are done with the coupling constants varied within their errors. Note that all the models give consistent results for the D_s. In fact, we found about 1% systematic uncertainty in the decay fractions of the landmark channels ($\overline{K}^*(892)K^+$ and $\phi\pi^+$) due to which model is used in the fit. The results quoted in Chapters 5 and 6 use the WA76 model.

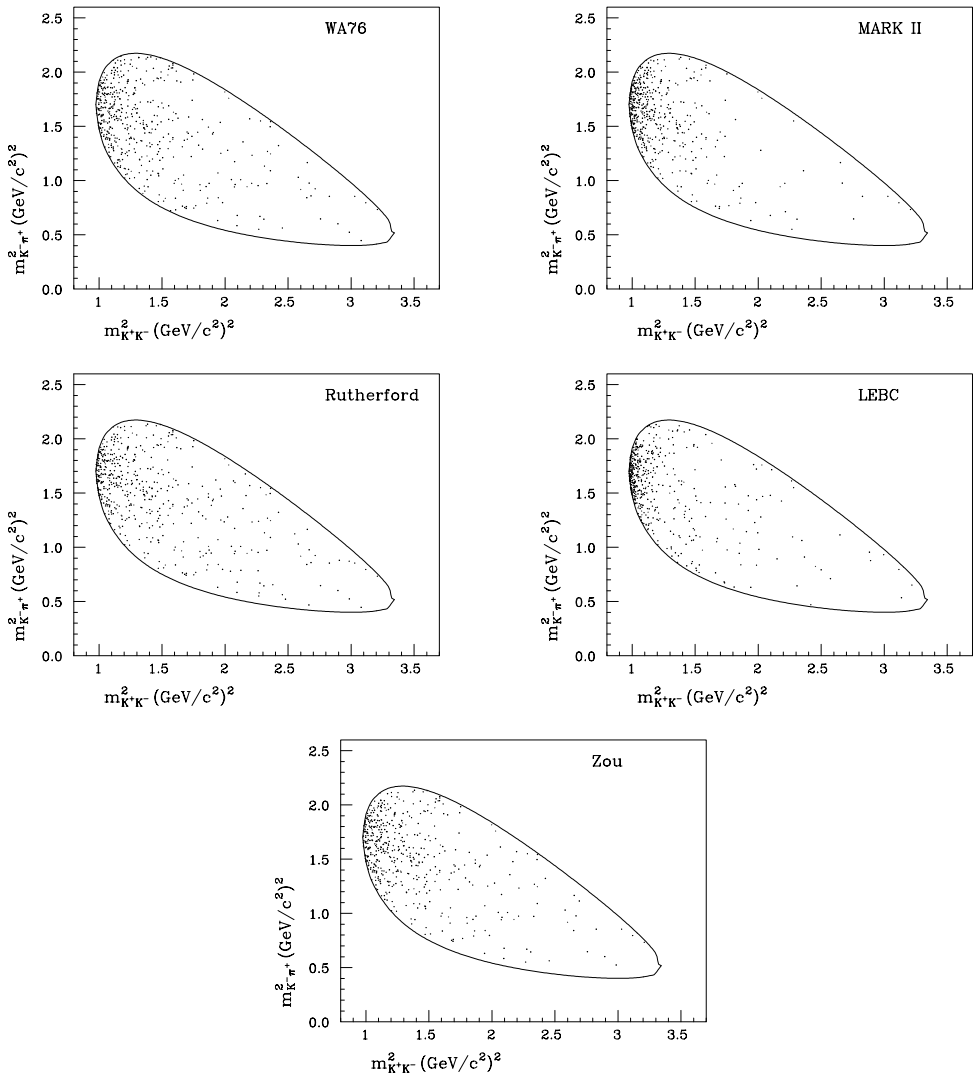

Figure C.1 Simulations of various pure $f_0(980)\pi^+$ decays on the $D_s^+ \to K^+K^-\pi^+$ Dalitz boundary.

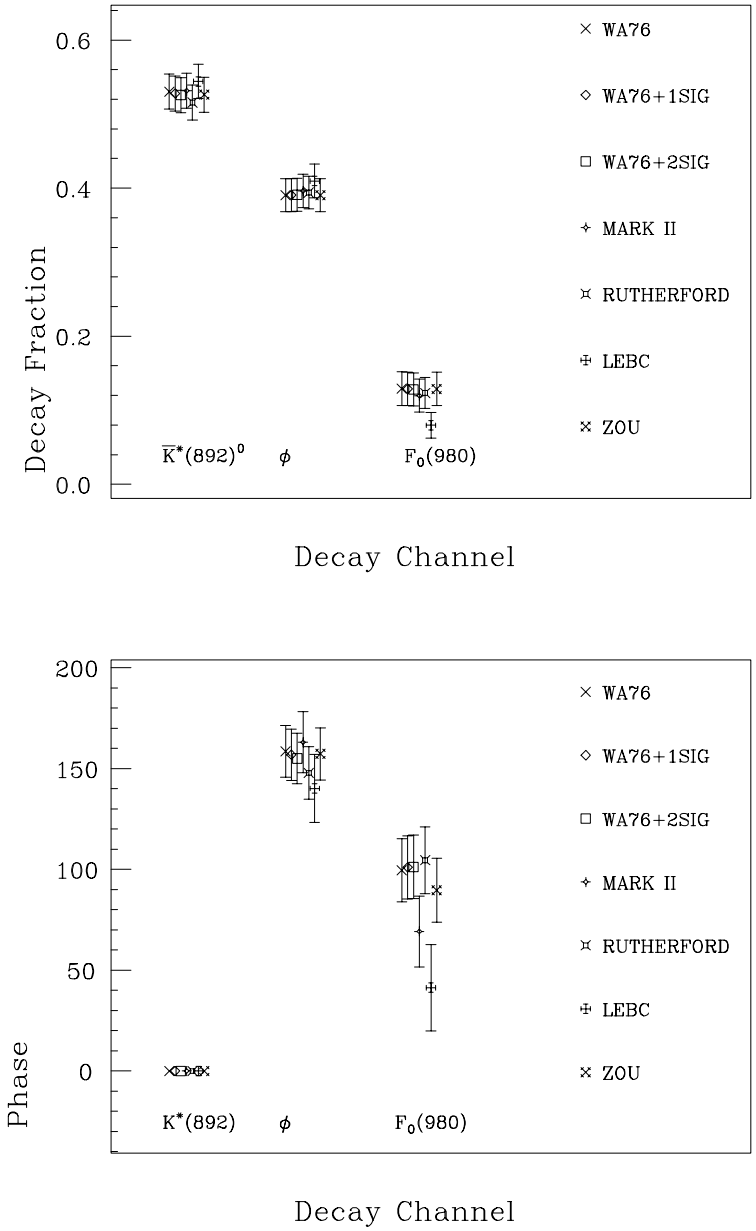

Figure C.2 Comparison of fits to $D_s^+ \to K^+K^-\pi^+$ data with coherent mixtures of $\overline{K}^*(892)K^+$, $\phi\pi^+$ and the indicated model for $f_0(980)\pi^+$. Top plot shows the resulting decay fractions, bottom the fitted phases.

Appendix D

The Lorentz Covariance of the Zemach Amplitudes

In this appendix, we address the apparent non-Lorentz invariance of our Zemach amplitude for the decay process $D \to rc \to (ab)c$, Eq. 2.8-

$$\mathcal{M}\left[D \to rc \to (ab)c\right] = y\ T^J(\vec{c}) : T^J(\vec{a}) \ \times \ BW(q) \tag{2.8}$$

It is understandable that the reader may be confused by the fact that, although we introduced the Zemach formalism with a manifestly Lorentz invariant decay amplitude (see Fig. 2.7 and Eq. 2.5), our formalism appears to not be covariant. We will discover that in fact our Zemach amplitudes are Lorentz invariant. By writing the amplitude in the rest frame of the intermediate resonance we hide the required covariance.[1]

We begin by writing the simplest Lorentz invariant decay amplitude for the decay $D \to rc \to (ab)c$ -

$$\mathcal{M}\left[D \to rc \to (ab)c\right] = y \times BW \times \sum_m a^\mu b^\nu e_{\mu\nu}(\vec{q},m) e^*_{\alpha\beta}(\vec{q},m) D^\alpha c^\beta \tag{D.1}$$

In this equation, $e_{\mu\nu}$ (and $e_{\alpha\beta}$) is an energy-momentum spin state vector of the intermediate resonance r. The 4-vectors of the participating particles are as indicated. m is the spin eigenvalue along the z-axis of the resonance r. We now define the *projection operator*

$$P^{(J)}_{\mu\nu\alpha\beta} = \sum_m e_{\mu\nu}(\vec{q},m) e^*_{\alpha\beta}(\vec{q},m) \tag{D.2}$$

which accomplishes the summation over all the spin polarizations of the resonance. This definition allows us to write the manifestly Lorentz invariant ampli-

1 The present discussion echoes Sec. 8.4 in Ref. [48].

tude Eq. D.1 as follows -

$$\mathcal{M}\left[D \to rc \to (ab)c\right] = y \times BW \times a^{\mu} b^{\nu} P^{(J)}_{\mu\nu\,\alpha\,\beta} D^{\alpha} c^{\beta} \qquad (D.3)$$

In the rest frame of the resonance, $\vec{q} = \vec{0}$. Therefore, the spin state four vector of the resonance becomes $e_{\mu\nu}(\vec{0}, m) = \{\vec{0}, \hat{e}(m)\}$, where $\hat{e}(m)$ are the polarization vectors in three-momentum space.[2] The key point is the Lorentz contractions in Eq. D.3 lose their dependence on energy, and therefore can be written in terms of sums over Cartesian indices i, j, k. In other words, in RF_r D.3 becomes

$$\mathcal{M}\left[D \to rc \to (ab)c\right] = y \times BW \times a^{*i} b^{*j} P^{(J)}_{ijkl} D^{*k} c^{*l} \qquad (D.4)$$

where '$*$' denotes RF_r quantities. If we define the following tensors

$$\begin{aligned} T^{(J)}_{ij}(D^{*k}, c^{*l}) &= P^{(J)}_{ijkl} D^{*k} c^{*l} \\ \hat{T}^{(J)}_{ij}(a^{*i}, b^{*j}) &= a^{*i} b^{*j} \end{aligned} \qquad (D.5)$$

we may write Eq. D.4 as follows -

$$\mathcal{M}\left[D \to rc \to (ab)c\right] = y \times BW \times \hat{T}^{(J)}_{ij}(a^{*i}, b^{*j}) : T^{(J)}_{ij}(D^{*k}, c^{*l}) \qquad (D.6)$$

In RF_r, $\vec{a^*} = -\vec{b^*}$ and $\vec{D^*} = -\vec{c^*}$, so we simply abbreviate the notation as follows -

$$\mathcal{M}\left[D \to rc \to (ab)c\right] = y \times BW \times \hat{T}^{(J)}(\vec{a}) : T^{(J)}(\vec{c}) \qquad (D.7)$$

where, although the momenta are in the rest frame of particle r, we have suppressed the '$*$'. This expression is identical to our Zemach amplitude, Eq. 2.8.

We have shown that the apparent non-covariance of the Zemach formalism is just a smokescreen - the decay amplitude is in fact Lorentz invariant. We avoid the complications arising from bookkeeping the four-momentum indices by evaluating the amplitude in the rest frame of the intermediate resonance.

---

2 As an example, the polarization vectors in three-momentum space for spin-1 are $\hat{e}(\pm 1) = \mp\frac{1}{\sqrt{2}}(\hat{x} \pm i\hat{y})$ and $\hat{e}(0) = \hat{z}$.

References

[1] L.M. Jones and H.W. Wyld, Phys. Rev. D 17 (1978) 759.

[2] F. Halzen, A. Martin, *Quarks and Leptons*, (1984).

[3] See for example the following and references therein:
B. Yu. Blok, M.A. Shifman, Sov. J. Nucl. Phys. 45 (1987) 522;
L.L. Chau, H.Y. Cheng, Phys. Rev. D 36 (1987) 137;
M. Diakonou and F. Diakonos, Phys. Lett. B 216 (1989) 436;
P. Bedaque, A. Das, V.S. Mathur, Phys. Rev. D 49 (1994) 269.

[4] M. Bauer, B. Stech, M. Wirbel, Z. Phys. C34 (1987) 103.

[5] J. Donoghue, Phys. Rev. D 33 (1986) 1516.

[6] D. Coffman, *et. al.*, Phys. Rev. D45 (1992) 2196.

[7] J. Korner, K. Schilcher, M. Wirbel, Y. Wu, Z. Phys. C48 (1990) 663.

[8] F. Bucella, M. Lusignoli, G. Miele, A. Pugliese, Z. Phys. 55 C, (1992), 243.

[9] C. Zemach, Phys. Rev. B140 (1965) 109.

[10] C. Zemach, Phys. Rev. B140 (1965) 97.

[11] C. Zemach, Phys. Rev. B133 (1964) 1201.

[12] S. Weinstein, Phys. Rev. 133 B (1964) 1318; S. Weinstein, Phys. Rev. 134 B (1964) 882; S. Weinstein, Phys. Rev. 181 B (1969) 1893.

[13] A. J. Weinstein, Private Communication

[14] Rodney Greene, Jim Wiss, 'E687 Memo: $D, D_s \to KK\pi$ Dalitz Plot Analysis - Update,' Jan. 16,1993.

[15] J.M. Blatt, V.F. Weisskopf, *Theoretical Nuclear Physics*, (1952).

[16] ARGUS Collab., H. Albrecht *et al.*, Phys. Lett. B 308 (1993) 435.

[17] P.L. Frabetti *et al.*, Phys. Lett. B 331 (1994) 217.

[18] Mark III Collab., J. Adler *et al.*, Phys. Lett. B 196 (1987) 107.

[19] E687 Collab., P.L. Frabetti *et al.*, Phys. Lett. B 286 (1992) 195.

[20] E691 Collab., J.C. Anjos *et al.*, Phys. Rev. D 48 (1993) 56.

[21] E691 Collab., J.C. Anjos *et al.*, Phys. Rev. Lett. 60 (1988) 897.

[22] E691 Collab., J.C. Anjos *et al.*, Phys. Rev. Lett. 62 (1989) 125.

[23] E687 Collab., P.L. Frabetti *et. al.*, Fermilab Pub 90/258-E (1990) 1.

[24] E687 Collab., P.L. Frabetti *et. al.*, Nucl. Instr. and Methods A 320 (1992) 519.

[25] R. Culbertson, R. Gardner, D. Pedrini, "E687 Memo: Post Hoc No More? Rogue MCS and PWC Noise Improvements,' March 1994.

[26] T.Sjostrand, Computer Phys. Comm. 39 (1986) 347;\ T.Sjostrand, H.-U.Bengtsson, Computer Phys. Comm. 43 (1987) 367;\ H.-U.Bengtsson, T.Sjostrand, Computer Phys. Comm. 46 (1987) 43;\ R. Gardner, 'E687 Memo: Lund Implementation in Rogue,' Jan. 10, 1992.

[27] Rob Gardner, Jim Wiss, 'E687 Meeting Talk: Update on Production Asymmetry Draft,' Jan. 5, 1995.

[28] Particle Data Group, K. Hikasa *et. al.*, Phys. Rev. D 45 S1 (1993).

[29] E687 Collab., P.L. Frabetti *et. al.*, Phys. Rev. D 50 (1994) 254.

[30] John F. Donoghue, *et. al.*, *Dynamics of the Standard Model* (1992).

[31] S. Malvezzi, D. Menasce, L. Moroni, 'E687 Memo: Some considerations on Dalitz fit procedures,' Oct. 20, 1993.

[32] Minuit Reference Manual Version 92.1, CERN, 1992.

[33] J. Wiss, R. Gardner, 'E687 Memo: Estimating Systematic Errors,' Feb. 22, 1994.

[34] R. Gardner, J. Wiss, 'E687 Memo:Assessing Goodness of Fit Using Adaptive Binning,'

[35] Rodney Greene, Jim Wiss, 'E687 Memo: $D_s^+ \to K^+K^-\pi^+$ Dalitz Plot Analysis - Update,' Dec. 16,1993.

[36] LEBC-EHS Collab., M. Aguilar-Benitez *et al.*, Z Phys C 36 (1987) 559.

[37] F. Buccella, *et. al.*, ROMA Preprint n. 1070-1994.

[38] Rodney Greene, Jim Wiss, Ray Culbertson, 'E687 Memo: Progress Toward $D^+, D_s^+ \to \pi^+\pi^+\pi^-$ Dalitz Plot Analysis,' Sep. 1,1993.

[39] Rodney Greene, Rob Gardner, Jim Wiss, 'E687 Memo: Preliminary $D^+, D_s^+ \to \pi^+\pi^+\pi^-$ Dalitz Analysis,' Jun 23, 1994.

[40] J.D. Richman, 'An Experimenter's Guide to the Helicity Formalism' (CALT-68-1148, California Institute of Technology), 1984.

[41] Martin L. Perl, *High Energy Hadron Physics* (Wiley, New York, 1974).

[42] J. D. Jackson, in Les Houches Lectures in High Energy Physics, 1965, C. DeWitt and M. Jacob, eds. (Gordon and Breach, New York, 1966).

[43] WA76 Collab., T.A. Armstrong, *et. al.*, Z. Phys. C51 (1991) 351.

[44] Mark II Collab., G. Gidal, *et. al.*, Phys Lett. B 107 (1981) 153.

[45] D.M. Binnie, *et. al.*, Phys. Rev. Lett. 31 (1973) 1534.

[46] LEBC-EHC Collab., M. Aguilar-Benitez, *et. al.*, Z. Phys. C50 (1991) 405.

[47] B.S. Zou and D.V. Bugg, Phys. Rev. D48 (1993) 3948.

[48] S. U. Chung, 'Spin Formalisms,' CERN 71-8, Mar. 25, 1971.

Vita

Rodney Lennart Greene was born August 17, 1962 in Austin, Texas and raised in Dallas, Texas. He received the S.B. degree in Engineering Science from Harvard University in 1985. He designed a minature incremental shaft encoder for robotics research for his final engineering design project. He subsequently joined the high frequency microelectronics group at the University of Texas at Austin, where he obtained the M.S. degree in electrical engineering in 1987. His thesis, *Contactless Charaterization of Thin Layers on Semi-Insulating GaAs by a Microwave Impedance Technique* involved the design of a P-band microwave reflectometer to measure the sheet resistance and drift mobility of ion-implanted layers on semi-insulating GaAs wafers. From 1987 to 1990 he was a Civil Engineering Officer in the United States Air Force and was responsible for the design of base electrical power construction projects. In 1990 he joined the nuclear physics group at the University of Illinois at Urbana-Champaign as a graduate assistant, where he designed trigger electronics for the JETSET experiment at CERN, a search for glueballs (gg and ggg). In 1991 he joined the E687 Collaboration, photoproduction of heavy flavors at Fermilab and participated in the 1990-1991 fixed target run. He was the primary author of the following paper: *Analysis of the* $D^+, D_s^+ \to K^+K^-\pi^+$ *Dalitz Plots*, E687 Collab., P.L. Frabetti *et. al.*, to be published in Phys. Lett. B.